THE UNIVERSITY *of* EDINBURGH

This thesis has been submitted in fulfilment of the requirements for a postgraduate degree (e.g. PhD, MPhil, DClinPsychol) at the University of Edinburgh. Please note the following terms and conditions of use:

This work is protected by copyright and other intellectual property rights, which are retained by the thesis author, unless otherwise stated.
A copy can be downloaded for personal non-commercial research or study, without prior permission or charge.
This thesis cannot be reproduced or quoted extensively from without first obtaining permission in writing from the author.
The content must not be changed in any way or sold commercially in any format or medium without the formal permission of the author.
When referring to this work, full bibliographic details including the author, title, awarding institution and date of the thesis must be given.

THE UNIVERSITY *of* EDINBURGH

Exoskeleton-assisted Locomotion

Design, Control & Evaluation of Wearable Robotic Devices

Daniel F. N. Gordon

Doctor of Philosophy

School of Informatics

The University of Edinburgh

2021

Daniel F. N. Gordon
Exoskeleton-assisted Locomotion:
Design, Control & Evaluation of Wearable Robotic Devices
Doctor of Philosophy, 2021

Supervisor:
Prof. Sethu Vijayakumar FRSE

To Mum & Dad,
For always being there,

and

In loving memory of Mary Boyd,
Miss you Granny.

Lay Summary

Assistive devices such as exoskeletons (which are worn) or prostheses (which replace a missing body part) have great potential as tools for both augmentation and rehabilitation. However, it is uncommon to see exoskeletons used widely outside of hospitals, research labs, and rehabilitation centres. Prosthetic limbs, whilst more common, are usually passive; meaning that they contain no motors or other actuators with which to provide assistive forces.

The reason for this is in large part due to the complexity of controlling these devices, especially in non-controlled environments where there are a huge array of factors to consider. Such factors including anything from the need to stop or change direction suddenly when walking to avoid bumping in to someone, to the more regular need to change walking speed or incline.

In this thesis, we attempt to devise a method for controlling exoskeletons and prosthetics which is able to account for these factors, based on mathematical optimisation. A model-based approach is taken, which means rather than relying on techniques which are purely data-driven, we use simulations to attempt to predict how the human body reacts to the forces applied by the assistive device.

We identify three open-problems: how to effectively model humans wearing assistive robotic devices; deciding what measures we should try to optimise for the human when we choose what forces the exoskeleton should apply; and how to account for the fact that humans change their walking style when experiencing external assistance. This thesis presents solutions to these problems, and quantifies the performance of these solutions using experimental motion data.

Abstract

Assistive robotic devices such as exoskeletons and prosthetic limbs have great potential as tools for both augmentation and rehabilitation. However, due to the complexity of controlling these devices, especially in unstructured environments where factors such as walking speed and incline can vary rapidly, it is uncommon to see exoskeletons outside of a clinical or research setting. Prostheses, whilst more common, are typically passive, which limits their ability to match the push off forces associated with healthy gait.

Motivated by modern techniques for controlling legged robots, this thesis motivates the pursuit of an optimisation-based approach to the control and design of exoskeletons. We identify a number of open problems within the field, namely (1) how to model the dynamic interaction between a human subject and an attached exoskeleton; (2) identifying the appropriate metric or combination of metrics to optimise for in exoskeleton-assisted locomotion; and (3) how to account for changes in human walking style induced by the presence of external assistive forces. This thesis details attempts to solve each of these problems.

We present a methodology for expressing human-exoskeleton system models as a combination of musculoskeletal models, exoskeleton inertial parameters and constraint forces. A specific human-exoskeleton model is detailed, along with a range of methods for modelling the interaction forces which occur at the attachment points between the human and exoskeleton agents. Experimental motion data is analysed using musculoskeletal modelling software (OpenSim) to quantify the effect that each of these interaction models, which represent various degrees of approximation, have on the resulting human-exoskeleton dynamics.

Applying exoskeleton assistance is inherently a shared control problem.

The overall goal is not to achieve a prescribed motion at any cost, or to do so while minimising exoskeleton joint torques, but rather to enhance aspects of the assisted humans motions; for example, increasing energy efficiency or stability. Therefore, in order to optimise exoskeleton control patterns we must first consider what it means for the resultant gait patterns to be optimal, or even good. We present a detailed analysis of exoskeleton-assisted walking in healthy subjects, with a particular focus on identifying those metrics which are invariant to changes in walking condition (e.g. walking speed or incline). We posit that such metrics, which exhibit strong invariance properties, are good candidates for the objective function of an optimisation-based controller.

Human walking strategies are unique and complex, and the problem of predicting the effect of exoskeleton assistance on a subjects gait pattern is a challenging one. In recent years, success has been had by methods which aim to learn suitable assistance strategies directly from a subject, via a process known as human-in-the-loop optimisation. We present a novel human-in-the-loop framework which utilises musculoskeletal modelling to make the learning process more time-efficient. Our method is evaluated on a number of subjects walking on a treadmill with exoskeleton assistance. In addition, we also explore how human-in-the-loop optimisation can be used to inform the design of exoskeletons to enhance their assistive capabilities.

Overall, these contributions represent a step towards enabling the wider usage of exoskeletons and other assistive robotic devices, which could lead to significant improvements to quality of life for many.

Acknowledgements

First and foremost, I would like to extend a huge thank you to my supervisor, Sethu Vijayakumar, not only for providing me with guidance and encouragement for these past years — though that was there in spades — but for his support with non-academic issues as well.

I am also very grateful to the entire SLMC research group, whose feedback and suggestions were always a big help in overcoming research challenges, and to Zhibin Li and Michael Mistry for their feedback and guidance during my end-of-year review meetings.

I would like to thank the ATR institute in Japan, for hosting me for a research exchange and allowing me to use the XoR exoskeleton, and in particular Jun Morimoto and Takamitsu Matsubara for their supervision and making me feel welcome. In addition, I am very grateful for the generous help provided by IUVO with hardware issues near the end of my PhD, which helped me complete some important experiments on time.

A special thank you goes to Chris McGreavy, for numerous discussions on experimental design and helping me with my lack of hardware & electronics know-how, and Graham Henderson, who I closely collaborated with in the early years of my PhD and learned much from about gait analysis.

I am also hugely thankful for my friends in Edinburgh, Buckie and elsewhere who have helped keep me sane during the harder times of my PhD. A particular thank you to my DnD group, for many stress-free Wednesday evenings of escapism. “Stand and fight!”

Finally, my deepest gratitude goes to my family, for always supporting me and pushing me to try my best, and to my partner Caitlin Gillespie, for being my rock throughout the difficult year that was 2020.

Declaration

I declare that this thesis was composed by myself, that the work contained herein is my own except where explicitly stated otherwise in the text, and that this work has not been submitted for any other degree or professional qualification except as specified.

Daniel F. N. Gordon
19th October 2021

Contents

Chapter 1

Introduction

For decades, assistive robotic devices such as exoskeletons, exosuits and prosthetic limbs have been a topic of major interest in the biomechanics and robotics communities [1]. These platforms, many of which have been developed [2], are thought to have huge potential in a wide range of application domains related to human movement. For example, devices such as the Lokomat [3], a gait rehabilitation robot, have demonstrated the potential to be more effective than conventional treatments at restoring mobility to patients with spinal cord injuries [4]. Passive exoskeletons are being developed to help reduce the potential for strain-related injuries in the work-place [5], or to reduce the energy required for locomotion [6]. New powered ankle prostheses continue to be designed with the goal of replicating the energy efficiency of the biological

human ankle [7, 8]. Additionally, exoskeletons are being developed as assistive tools to reduce the metabolic cost of walking, with some recent advances in state-of-the-art soft exosuits [9] demonstrating energy savings of more than 20% [10].

However, many of these devices, particularly those featuring powered assistance, are largely restricted to being used in supervised clinical or research settings, where time and care is taken to ensure that the behaviour of the exoskeleton and the nature of the rehabilitation or assistive regime is well-suited to the subject in question [11]. The use of exoskeletons in a real-world setting is made difficult by the number of variables to consider as a human walks in an uncontrolled environment - for example, walking speed, or whether the subject is walking on an incline. Each of these variables can affect the gait pattern of an individual, and therefore the optimal torques to be applied by an assistive device [12]. Moreover, the effectiveness of applied assistance has been shown to be dependant upon its magnitude and timing [10, 13], the optimal values of which vary between subjects. Therefore, it is important that the design and control-algorithms underpinning assistive robotic devices are sufficiently subject-specific.

If exoskeletons are to become widely used devices outside of a clinical setting it is important that suitable techniques are developed that can account for these difficulties. To this end, this thesis discusses the use of model-based methods and optimisation frameworks for better optimising the control and design of exoskeletons.

1.1 Exoskeleton Control as an Optimisation Problem

Evidence suggests that an underlying goal of human gait is the minimisation of energy consumption[1] [14]. Any external assistance that is applied via an external agent, such as an exoskeleton or prosthetic limb, is likely to disrupt this optimisation process if not controlled appropriately. Classical exoskeleton control algorithms typically aim to reinforce measured signals from the

[1] Human gait appears to be energetically optimal in the absence of other goals, e.g when able to walk at a comfortable speed on flat terrain. However, humans commonly sacrifice some degree of energy economy in favour of pursuing other objectives, such as maintaining balance on slippery terrain or making a quick journey [14].

subject, e.g muscle activations [15, 16]. However, such techniques have been shown to often result in comparatively small reductions in energetic cost [17]. If we wish to efficiently assist the human body in its movements, we should do so in a way that respects, and can reinforce, the underlying optimisation of energy and gait stability. One approach to achieve this is to treat exoskeleton control as an optimisation problem.

1.1.1 Mathematical Optimisation

The general form of an optimisation problem of real variables, as specified by Nocedal & Wright [18], is as follows:

$$\min_{x \in \mathbb{R}^n} f(x), \tag{1.1}$$

$$c_i(x) = 0, \quad i \in \mathcal{E}, \tag{1.2}$$

$$c_i(x) \geq 0, \quad i \in \mathcal{I}. \tag{1.3}$$

Here, x is a vector containing our *input variables* and f is the *objective function*. The functions c_i are the *constraints*, of which p are *equality constraints* and q are *inequality constraints*, where $p = |\mathcal{E}| \geq 0$ and $q = |\mathcal{I}| \geq 0$. We will follow this generic formulation throughout this thesis when specifying optimisation problems.

1.1.2 Rigid Body Dynamics

A rigid body system is a collection of rigid bodies connected by joints [19]. Bodies are structures with known dynamic properties e.g. mass and inertia, while joints act to constrain the motion of bodies relative to one another. The equation of motion for a general rigid-body system can be written as follows:

$$M(\mathbf{q})\ddot{\mathbf{q}} + \mathbf{c}(\mathbf{q}, \dot{\mathbf{q}}) + \mathbf{g}(\mathbf{q}) = \boldsymbol{\tau}. \tag{1.4}$$

Here, $\mathbf{q} \in \mathbb{R}^n$ is the vector of generalised positions — the joint angles or displacements of the joints in the rigid body model. The parameter n, which describes the number of unconstrained joint axes, is known as the number of degrees of freedom of the system. On the left hand side, M is known as the

Implicit Time Dependence

The variables in the equations of multibody dynamics either explicitly depend on time ($\mathbf{q}$) or are functions of these variables ($\mathbf{M}, \mathbf{c}, \mathbf{g}$). Moving forward, we will continue to avoid explicitly expressing time dependence in our dynamics equations so as keep the equations uncluttered, but it should be kept in mind that, for example, the joint angle vector $\mathbf{q}$ actually represents a time-series of joint-angle vectors, and likewise for other parameters.

mass or inertia matrix, $\mathbf{c}$ is the summed contribution of non-linear terms such as friction and Coriolis forces, while $\mathbf{g}$ is the force due to gravity. Finally, on the right hand side, $\boldsymbol{\tau} \in \mathbb{R}^n$ is the generalised force (force or torque) acting at each degree of freedom of the model.

1.1.3 A Simple Base-Case

Consider a human subject moving with some goal in mind. We will assume in the first instance that we can represent the human as a rigid composition of bodies and joints, as in the manner of rigid body dynamics, and that the goal takes the form of a trajectory of joint angles over time. We can then phrase the problem of the subject carrying out the desired motion as an optimisation problem, like so:

$$\min_{\boldsymbol{\tau}_h} \|\mathbf{q} - \mathbf{q}_d\|, \tag{1.5}$$

$$M_h(\mathbf{q})\,\ddot{\mathbf{q}} + \mathbf{c}_h(\mathbf{q}, \dot{\mathbf{q}}) + \mathbf{g}_h(\mathbf{q}) = \boldsymbol{\tau}_h + \boldsymbol{\tau}_g. \tag{1.6}$$

These equations specify an optimisation problem that aims to identify the optimal human torques for completing a specified motion. We use the subscript h to denote *human-centric* quantities, so for example M_h denotes the mass matrix associated with the rigid body model representing the human, while $\boldsymbol{\tau}_h \in \mathbb{R}^n$ denotes the torques generated at the joints of the human model. So far, the only quantity which is not human-centric is $\boldsymbol{\tau}_g$, which denotes the torques generated at the joints of the model by external forces.

Ground Reaction Forces

In most cases, $\boldsymbol{\tau}_g$ results from the combined effects of the reaction force between each foot and the ground, i.e.

$$\boldsymbol{\tau}_g = \boldsymbol{\tau}_L + \boldsymbol{\tau}_R = J_L^\top \mathbf{f}_L + J_R^\top \mathbf{f}_R,$$

where $J_L^\top$ is the transpose of the Jacobian defined at the centre of pressure of the left foot, which maps the 6D spatial force $\mathbf{f}_L$ on to the generalised torque component $\boldsymbol{\tau}_L$, and similarly for those terms subscripted with R.

1.2 Open Problems & Assumptions

At this point, we can consider the task of modifying or adding to the optimisation problem outlined in the previous section so as to model the assistance of a robotic agent, i.e an exoskeleton. However, in its current form, this system of equations contains a number of implicit assumptions pertaining to human locomotion that ultimately prove problematic.

1.2.1 Incorporating Exoskeleton Assistance

Consider the problem of assisting the subject to achieve the goal via the means of an attached powered exoskeleton. Adding a device to the system has two main effects:

1. The motion of the human is affected by the inertia of the exoskeleton.
2. The motors of the exoskeleton apply additional external forces, via some sort of attachment to the human.

The above effects each result in modifications to the optimisation problem, which we must ensure are dynamically accurate while remaining computationally efficient to solve.

1.2.2 Musculoskeletal Dynamics

So far, we have presented our optimisation problem in joint-space, essentially assuming the presence of ideal torque actuators at each joint of our rigid-body

model. Human motion, however, is driven by the action of muscle-tendon units, often referred to as MTU's. There are two compelling reasons to analyse human motion at the scale of muscles:

1. Muscles can influence the motion of all the joints that they cross - which, crucially, can be more than one. Muscles which cross two joints are known as *bi-articular*; such muscles induce a coupling between joints that is not present in the joint-space formulation, but is important to consider for accurate simulations.

2. We gain a much greater level of insight in to the dynamics of human motion, which is made more realistic through use of appropriate muscle parameters, ascertained through decades of research in to human muscle physiology.

Given these points, an exoskeleton control problem should likely be at least partly based in the *muscle-space* of motion, rather than the *joint-space* formulation presented thus far.

1.2.3 Optimisation Criteria

The objective function for our base-case optimisation problem is a simple minimisation of trajectory error. However, humans can exhibit significant variation in kinematic trajectories depending on the current walking context [12]. Humans walking in normal environments may indeed seek to optimise cost of transport, whereas humans walking in unsafe environments (e.g. on an icy surface) may instead optimise more for stability, increasing muscle stiffness at the cost of energy efficiency.

Previous works suggests that, in general, human locomotion is optimised for energy efficiency and stability [14] rather than adherence to kinematic trajectories. Given this, it is important to identify metrics for use in the objective function of our optimisation problem which can either explicitly or implicitly work towards the same goal.

1.2.4 The Shared Control Problem

In Equation (1.6), the exoskeleton contribution $\boldsymbol{\tau}_e$ and human contribution $\boldsymbol{\tau}_h$ are assumed to be independent components of the generalised net force vector. However, it is both intuitive and suggested by the literature [20] that humans adapt their own behaviour (muscle activations, in this case) in response to external physical stimuli, more so than what is predicted by dynamics alone[2]. This can quickly lead to a chicken and egg type problem: exoskeleton torques are prescribed assuming certain muscle activations, which induces an unexpected change in muscle activation, so the applied torques must be adjusted, which again induces an unexpected change in muscle activation, and so on ad infinitum. The human and exoskeleton agents can be considered to *share control* over the combined human-exoskeleton system. To apply exoskeleton torques in a way that benefits the human-exoskeleton system as a whole, we must be able to predict or learn how human behaviour will change according to the applied magnitude and form of exoskeleton assistance.

In exoskeleton-asssisted locomotion, the shared control problem only surfaces when the human agent can exert some control over system behaviour, i.e $\boldsymbol{\tau}_h \neq \mathbf{0}$. A sub-class of exoskeletons exist which are designed to compensate for a complete lack of muscle activity in one or more muscle groups, i.e. those designed for quadriplegic or paraplegic patients [21, 22]. In some sense, the lack of human contribution in this subcase simplifies our optimisation formulation as the influence of uncertainty due to the shared control problem is reduced. However, in these cases the burden of system stability lies entirely with the exoskeleton, and so typically such devices are designed with a preference for stiff, position-based control systems [2, 22].

In this thesis, our aim is to produce a framework that can optimise human-exoskeleton motion on the musculoskeletal level, and so moving forward we will assume that there is a measurable human contribution to the net torque vector, i.e $\boldsymbol{\tau}_h \neq \mathbf{0}$. Note that under this assumption our methods are still widely applicable to those with significant muscle weakness due to injury or gait pathologies, as well as those with healthy gait patterns.

[2]Indeed, in [20] healthy subjects were observed to exhibit increased activation of leg muscles in response to exoskeleton assistance, despite expectations to the contrary.

1.3 Thesis Structure

Our findings from the previous section can be summarised in the form of three open questions in the field of model-based exoskeleton control.

1. How can we effectively model the dynamic interaction between a human and an attached exoskeleton on a musculoskeletal level?

2. What is the appropriate objective function to optimise for to ensure the resultant exoskeleton-assisted motion is both stable and energetically efficient?

3. How can we model or otherwise account for the effects of shared control on underlying neuromuscular control strategies?

It is the answers to these three questions which make up the primary contributions of this thesis.

To begin, Chapter 2 provides an overview of modern techniques in experimental gait analysis. Much of the analysis presented in the thesis is based on collected human motion data, and so it is worthwhile to outline the hardware and data processing details in full. Next, Chapter 3 discusses approaches for modelling human-exoskeleton systems. In addition, methods for modelling human-exoskeleton interaction forces are presented and compared. Chapter 4 introduces a formalisation of the concept of gait metrics, for use in the objective function of the exoskeleton control problem, and presents an analysis of the invariance properties of a range of commonly used gait metrics within the wider biomechanics literature. In Chapter 5, a framework is presented for optimising exoskeleton control & design parameters online using experimental data. Then, an application of this framework is presented in the space of optimising exoskeleton design parameters. In Chapter 6, a further application is presented in the space of optimising exoskeleton assistance strategies. Finally, the contributions of this thesis are summarised in Chapter 7, and possible future research directions are discussed.

1.3.1 Original Contributions

This thesis adapts material from a number of publications by the author:

1. Gordon, D.F.N., Henderson, G. and Vijayakumar, S., 2018. Effectively quantifying the performance of lower-limb exoskeletons over a range of walking conditions. Frontiers in Robotics and AI, 5, p.61.

2. Gordon, D.F., Matsubara, T., Noda, T., Teramae, T., Morimoto, J. and Vijayakumar, S., 2018, August. Bayesian optimisation of exoskeleton design parameters. In 2018 7th IEEE International Conference on Biomedical Robotics and Biomechatronics (Biorob) (pp. 653-658). IEEE.

3. Henderson, G., Gordon, D. and Vijayakumar, S., 2017, December. Identifying invariant gait metrics for exoskeleton assistance. In 2017 IEEE International Conference on Robotics and Biomimetics (ROBIO) (pp. 520-526). IEEE.

In particular, parts of Chapter 3 are based on work from (1), parts of Chapter 4 are based on work from (1) and (3), and parts of Chapter 5 are based on content from (2). The content of Chapter 6 is currently undergoing the journal submission process.

Chapter 2

Experimental Gait Analysis

Exoskeletons and prosthetic limbs have made great strides in becoming more power efficient, comfortable, and lighter [1]. However, it is only relatively recently that exoskeleton hardware has been shown to have the ability to substantially reduce the energetic cost of walking [17], and even then only in a laboratory setting[3]. This makes clear the complexity of exoskeleton-assisted locomotion — and shows that if we wish to assist gait, we must first understand it. For this reason, gait analysis is a crucial tool; both for increasing our understanding of human locomotion in general, but also for gaining detailed insights in to individual gait patterns, which may differ greatly from group

[3]These results were achieved using human-in-the-loop optimisation — a technique which we will discuss in Chapter 5.

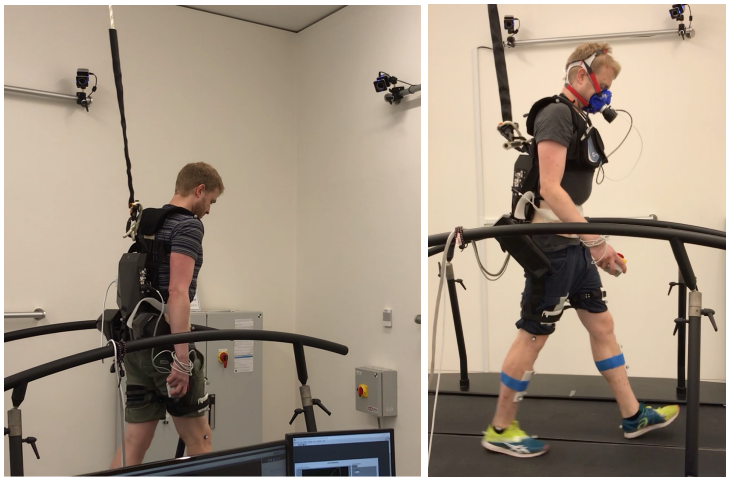

Figure 2.1: A subject walking in the Gait Lab at The University of Edinburgh. Equipment shown includes a Vicon motion capture system, Motek Medical treadmill, active pelvis orthosis, and respiratory gas analysis device.

means, especially in the case of pathological gait. Many techniques exist for studying human gait patterns. In this chapter, we provide a broad overview of four common methods.

The original contributions presented in this thesis involved significant collection of motion data. Largely, this data collection took place at The University of Edinburgh, where over several years a state-of-the-art gait analysis lab has been assembled. The lab (Figure 2.1) features a powerful gait simulation platform, detailed motion capture equipment, physiological evaluation capabilities, and state-of-the-art exoskeleton hardware — thus providing a detailed view in to exoskeleton-assisted locomotion. The remaining data was collected in collaboration with ATR at their research facility in Kyoto, Japan. In each of the following sections, as well as providing an overview of gait analysis techniques, we provide a detailed account of the specific experimental hardware used.

The final consideration of this chapter is the topic of processing raw motion data. This is an important step in producing usable information from what are often noisy data sources. So as to increase the replicability of the experiments and results discussed within this thesis, the various data processing steps taken are outlined in detail in the subsequent sections. These methods were implemented in the custom *Motion Data Processing* MATLAB toolbox[4], designed to enable efficient processing of experimental motion data.

[4] https://github.com/DanielFNG/motion-data-processing

2.1 Motion Capture

Motion capture is, in a general sense, the process of recording movement. Typically, this is done with the intent of later analysing or reconstructing the recorded motion in detail, so although the history of the field begins with mathematical analyses of still images [23] and the animation technique of rotoscoping [24], modern techniques are based on high precision, digital technologies. The scope for use of motion capture technology is vast, with a range of applications in fields such as clinical gait analysis [25], sports science [26] and character animation [27].

The most widespread motion capture systems are optical in nature, and use high-precision cameras to track the positions of experimental markers which are affixed to the object or subject to be tracked [28]. These markers can be active, in which case they emit infrared light which is received by the surrounding cameras, or passive, in which case they are designed to easily reflect infrared light emitted by the cameras themselves [29]. Active systems enable easy automatic labelling of markers, while passive systems rely on a combination of well designed labelling skeletons and manual post-capture clean-up of data. In either type of system, the output is the position in space of the experimental marker set over time, i.e a set of time-indexed marker trajectories which we can write as the following matrix

$$P = \begin{bmatrix} \mathbf{p}_{11} & \mathbf{p}_{12} & \cdots & \mathbf{p}_{1m} \\ \mathbf{p}_{21} & \mathbf{p}_{22} & \cdots & \mathbf{p}_{2m} \\ \vdots & \vdots & \ddots & \vdots \\ \mathbf{p}_{t1} & \mathbf{p}_{t2} & \cdots & \mathbf{p}_{tm} \end{bmatrix}, \tag{2.1}$$

where $\mathbf{p}_{ij} = \left(x_{ij}, y_{ij}, z_{ij}\right) \in \mathbb{R}^3$ is the 3D position of the j^{th} marker in the experimental marker set as measured at the i^{th} timestep of the recorded motion, relative to the origin of the motion capture system, which is set during calibration. Typically motion capture systems operate at a fixed frequency, so the above matrix corresponds to data collected over t frames using m experimental markers.

In Figure 2.2, a subject is shown wearing a set of reflective markers, along-

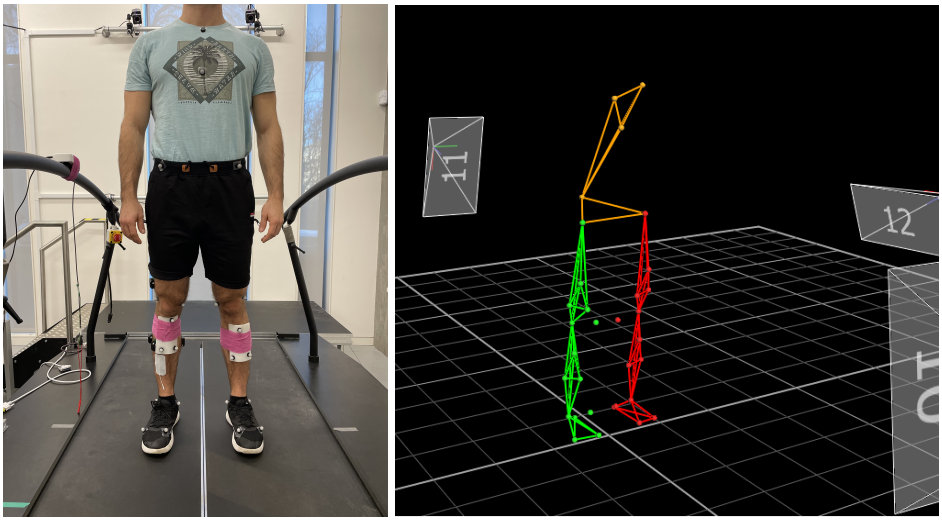

Figure 2.2: A subject wearing markers (**left**), and the corresponding reconstruction of the markers in the Vicon Nexus software (**right**).

side the digitally represented markers and connecting skeleton constructed by the motion capture software. For gait analysis, a common means of utilising the output data is via direct kinematics, whereby placing markers at known and fixed locations on the human body can directly infer joint centre locations and joint angles during motion [30]. Another method is to fit the movement of the experimental markers to a model of the system being studied. This is a key component of musculoskeletal modelling, which is a concept we will return to in Chapter 3.

Marker-free methods for motion capture are available [31] and an active area of research, though they do not currently match the accuracy or reliability of marker-based systems [32–34]. The most prevalent alternatives to optical motion capture are inertial systems [35]. This approach utilises inertial measurement units to approximate the joint angles of a biomechanical model customised to suit each participant. There are advantages and disadvantages to either type of motion capture: camera-based systems require clear open spaces or many cameras to ensure object occlusion is not problematic, and by their nature are restricted to a fixed capture volume covered by the cameras; meanwhile, inertial system suffer from measurements drifting over time, but are typically much more mobile.

Data Synchronisation

The frequencies listed in Sections 2.1.1 — 2.4.1 are the default sampling rates associated with each device. However, as of 2019 a Vicon Lock+ synchronisation box/ADC was used to directly interface with the analogue data measured in the gait lab (i.e. GRF data and EMG signals). All data measured via the Vicon Lock+ box was sampled at a rate of 1000Hz. Prior to this upgrade, synchronisation was handled by triggering data recording via an external phidget board with a known delay.

2.1.1 Hardware

Experimental marker trajectories collected during this thesis were captured at a frequency of 100Hz using a passive optical motion capture system[5]. Initially, the system contained 6 cameras, but was upgraded to a 10-camera system in 2019. The capture volume is centred on the walking area so as to easily capture gait patterns. The collected data consists of 3D position data for each marker attached to the subject (see Equation (2.1)).

A custom marker set was designed to carry out gait analysis with a particular focus on lower limb movements. This was adapted from the Cleveland marker set and consisted of 32 markers: 12 placed as rigid clusters to track thigh and shank movements, and 21 placed at bony landmarks on the human body [12, 36]. In Figure 2.3, we list the names associated to each marker and mark the locations on a reference subject.

Notably, our custom marker set represents the upper body using only three markers located on the chest and shoulders, and therefore the movements of the arms and hands were ignored during our experiments. This choice allowed for more markers (and hence resolution) to be focused on body parts which are more strongly linked to locomotion e.g. the feet, legs & pelvis, while still allowing upper-body movement to be approximated as that of the torso. This choice of marker placement is common when considering healthy human gait driven by lower-body movements [37], especially if computationally intensive analysis techniques are to be used [38].

[5]Vicon, Oxford, UK.

1 R. Acromium
2 L. Acromium
3 Clavicle
4 V. Sacral
5 R. ASIS
6 L. ASIS
7 R. Thigh Upper
8 R. Thigh Medial
9 R. Thigh Lateral
10 L. Thigh Upper
11 L. Thigh Medial
12 L. Thigh Lateral
13 R. Knee Medial
14 R. Knee Lateral
15 L. Knee Medial
16 L. Knee Lateral
17 R. Shank Upper
18 R. Shank Medial
19 R. Shank Lateral
20 L. Shank Upper
21 L. Shank Medial
22 L. Shank Lateral
23 R. Ankle Medial
24 R. Ankle Lateral
25 L. Ankle Medial
26 L. Ankle Lateral
27 R. MTP1
28 R. MTP5
29 R. Heel
30 L. MTP1
31 L. MTP5
32 L. Heel

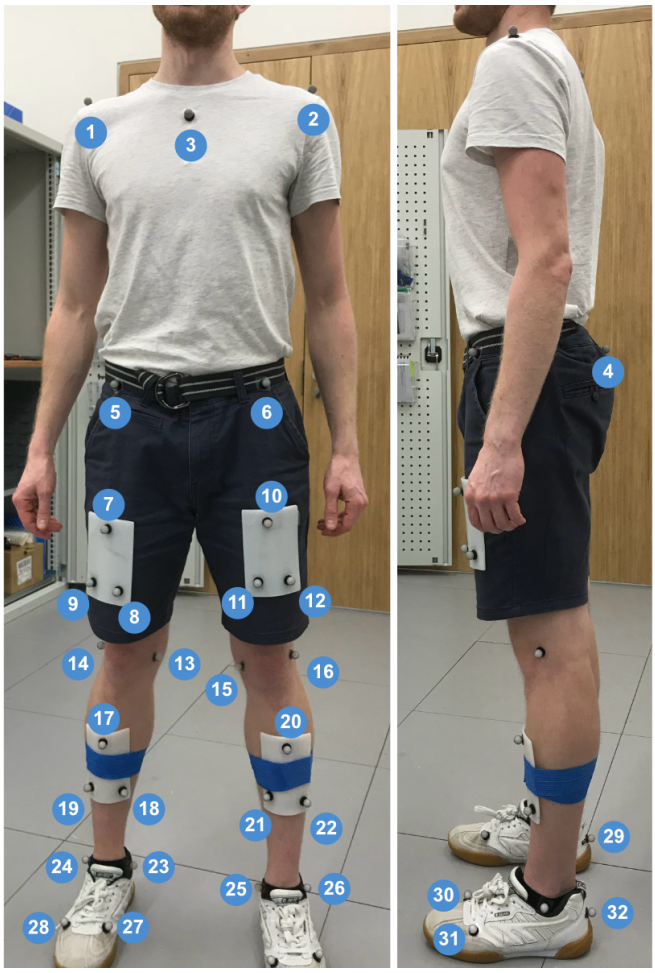

Figure 2.3: A graphical depiction of the gait analysis marker set.

2.1.2 Data Processing

Due to the occurrence of occlusions during data collection, marker trajectories typically contain 'gaps' which must be filled in order for the data to be useful for motion reconstruction. The Vicon Nexus software supports a number of gap-filling routines as standard, including spline, cyclic and rigid-body methods [39]. Spline filling is suitable for small, isolated gaps; cyclic fill is suitable when capturing repetitive data (e.g. gait cycles on a treadmill) and gaps are present in relatively few gait cycles; while rigid-body filling is appropriate for markers placed on inflexible surfaces (e.g. the thigh and shank

The OpenSim Co-ordinate System

OpenSim uses a right-handed coordinate system defined relative to the motion of the subject under investigation. From the perspective of a subject walking in the capture volume, the x axis is pointed forwards, the y axis is directed upwards, and the z direction is to the right. For consistency and ease of analysis, data presented throughout this thesis uses OpenSim coordinates where appropriate.

cluster markers pictured in Figure 2.3). The first and most time consuming step of processing marker data is to use an appropriate combination of these gap filling algorithms to correct for any gaps present in the raw data[6].

Once gaps are removed, the next step is to remove high frequency noise in the data which results from errors in camera calibration. This presents as a jitter in the recorded trajectories which can be removed by low-pass filtering with a Butterworth filter. More specifically, all marker data presented throughout this thesis has undergone low-pass filtering with a 6Hz, 4^{th} order, zero-lag Butterworth filter [12]. Then, the resultant gap-filled and filtered data is exported as a TRC file for use with the OpenSim software package [40]. Before motion reconstruction takes place, the data is converted to the OpenSim coordinate system via multiplication with a suitable rotation matrix. The orientation of the Vicon coordinate system relative to the OpenSim coordinate system is shown in Figure 2.4.

In summary, the post-collection data processing procedure for marker data is as follows:

1. Fill gaps present in the collected data;

2. Filter marker trajectories using a 6 Hz Butterworth filter;

3. Transform to OpenSim coordinate system.

4. Export to an OpenSim readable format.

[6] A Vicon system with sufficient coverage of the capture volume and a good (recent) camera calibration leads to fewer gaps which are therefore easier to fill.

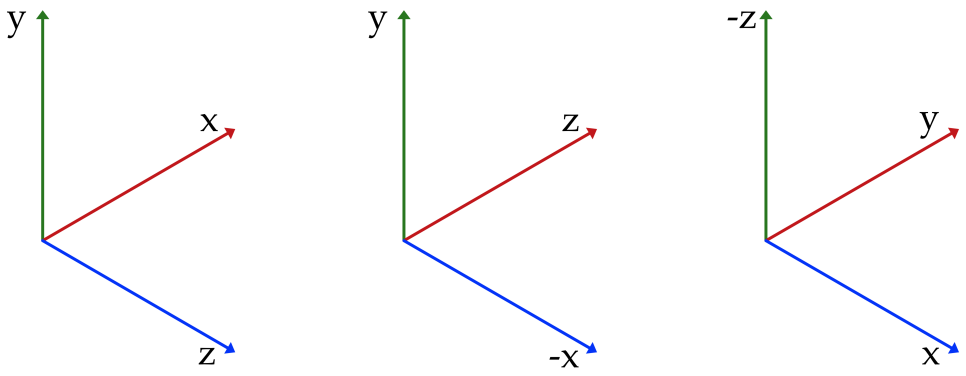

OpenSim Vicon Treadmill

Figure 2.4: The OpenSim, Vicon and Treadmill coordinate systems. In each case the red, green and blue arrows correspond to the forward, upwards and right directions, respectively, from the point of view of the subject.

In Figure 2.5, we show the result of the marker processing procedure on a sample of Vicon data collected in the gait lab.

2.2 Force Analysis

While motion capture alone can inform us of the kinematics of motion, to assess the dynamics of motion – joint torques or muscle forces, for example – we must also consider the action of external forces. In general such forces can arise from a number of sources: gravity, which is of course always acting, but can be easily modelled; external disturbances (e.g. pushes), which may necessitate an active balancing or push recovery response; or even a patient utilising a support rail during a rehabilitation program, thus distributing their weight over multiple contact points. As this thesis is focused particularly on locomotion, we will focus on the measurement of forces occurring due to interaction between the feet and the ground.

For each foot in contact with the ground, a person experiences a ground reaction force (GRF), equal and opposite in direction to the force exerted by the person on the ground due to gravity and forces of acceleration (Figure 2.6). The vertical component of the ground reaction force is due to gravity, while the horizontal components act due to friction between the foot and the ground surface. On flat ground, shear forces in the horizontal plane introduce a twist-

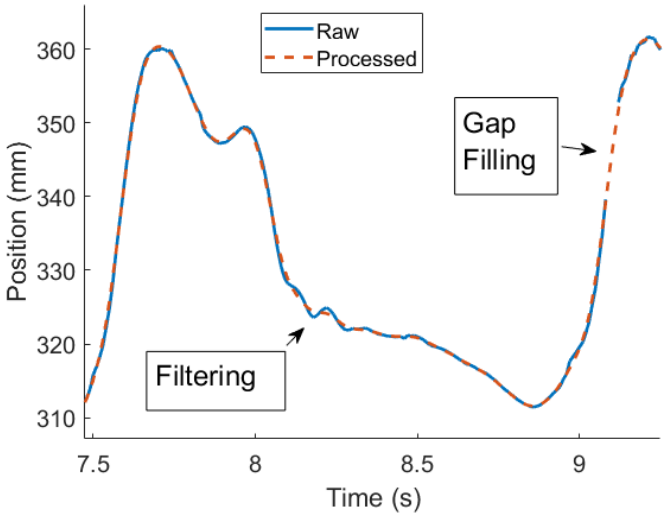

Figure 2.5: Raw (blue, solid) & processed (red, dashed) samples of marker data.

ing torque about the vertical axis. We will express ground reaction forces as 6D vectors by concatenating the force and torque components, e.g.

$$\mathbf{f}_g = \left(f_x, f_y, f_z, 0, T_y, 0\right) \in \mathbb{R}^6, \tag{2.2}$$

where here we have assumed that the vertical axis is in the y direction. Twists in other directions could be introduced if vertical shear forces were present e.g. when walking on unstable ground, however we will not cover this case here. The point of action of a ground reaction force is known as its centre of pressure,

$$\mathbf{c}_p = \left(c_x, c_y, c_z\right) \in \mathbb{R}^3, \tag{2.3}$$

which naturally varies in its location along the foot over the course of a gait pattern.

Ground reaction forces are most commonly measured using force plates. These devices used load cells to convert forces applied to the plate in to voltage changes which can be measured and reinterpreted as force data using the appropriate calibration information [41]. A number of competing force plate technologies exist which may differ in the types of load cell used or number of sensors [42, 43].

An alternative to force plates are pressure sensitive insoles [44]. These devices are worn in-shoe, and can measure the distribution of pressure over the sole of the foot [45]. Pressure insoles can prove useful when an increased

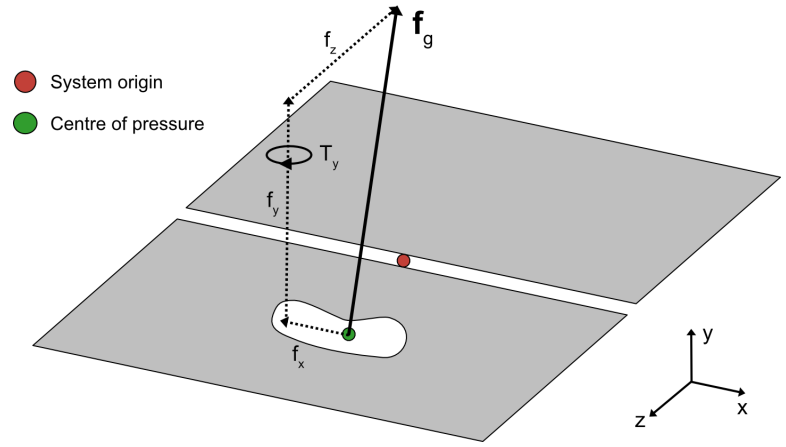

Figure 2.6: Diagram depicting the composition of the ground reaction force vector measured via a pair of force plates. In this example, only the right foot is in contact with the ground.

level of mobility is required e.g for use in tandem with a mobile exoskeleton or as part of a commercial prosthesis package. However, they cannot yet provide data which is as accurate or complete as force plate data [46], and therefore force plates remain the preferred measurement tool within laboratory and other research settings.

2.2.1 Hardware

Ground reaction force data was collected using the M-Gait[7], a split-belt treadmill with integrated force plates. In addition to allowing for coupled or independent control of belt speed, the treadmill allows for dynamic alterations to pitch & sway, even during operation. This allows for a high degree of flexibility in terms of simulating gait patterns, for example:

- normal gait on flat ground at a steady speed;
- pathological gait, using a slower speed on one belt to simulate a limp;
- walking on uneven terrain, by dynamically modulating the treadmill pitch.

The integrated force plates can measure the 3 dimensional force and moment experienced at the origin of each plate, i.e. $\mathbf{F} = (F_x, F_y, F_z)$ and $\mathbf{M} = (M_x, M_y, M_z)$. These values are updated at a framerate of 600Hz.

[7] Motek Medical B.V., Amsterdam, Netherlands.

2.2.2 Data Processing

The data collected output by the Motek Medical treadmill internally undergoes a conversion from voltages to force measurements using an internal calibration matrix, meaning the quantities we consider raw are the unfiltered ground reaction forces and moments acting on each plate[8]. The first processing step is to orientate the data in the OpenSim coordinate system (see Figure 2.4), after which the inclination of the treadmill is used to determine the appropriate level of gravity compensation. This is an important step; if the treadmill is set at an incline while recording, i.e to simulate walking up a hill, the mass of the system itself affects the ground reaction force measurements and must be filtered out to isolate the true GRF vector. This process involves the use of a gravity compensation matrix which was determined manually for our treadmill system[9]. Next, the GRF data is filtered using a 6Hz, 4^{th} order, zero-lag Butterworth filter [12], and clipped when the measured vertical force falls below 40N.

Once these initial processing steps are complete, the centre of pressure and torque measurements are calculated. For a given force plate p, given 3D force and moment vectors $\mathbf{f} = (f_x, f_y, f_z)$ and $\mathbf{m} = (m_x, m_y, m_z)$, we have:

$$\mathbf{c} = (\frac{m_z}{f_y} + d_x^p, d_y^p, \frac{-m_x}{f_y} + d_z^p), \tag{2.4}$$

where $\mathbf{c}$ is the centre of pressure vector and $\mathbf{d}^p = (d_x^p, d_y^p, d_z^p)$ is the displacement between the origin of the force plate p and the global origin. In this case the global origin corresponds to the treadmill origin, which is at a fixed distance of $0.25m$ from the centre of either force plate, i.e. $\mathbf{d}^l = (0, 0, -0.25)$ and $\mathbf{d}^r = (0, 0, 0.25)$, where l and r denote the left and right force plate, respectively, from the point of view of the subject. Next, to compute the torques $\mathbf{T}$ we have

$$\mathbf{T} = (0, m_y - c_z f_x + c_x f_z, 0). \tag{2.5}$$

[8]The treadmill also reports centre of pressure values directly, however computing these quantities from filtered data results in significantly less noise.

[9]A similar process would have to be run if another treadmill was used. A simple zeroing process could be used in lieu of determining a gravity compensation matrix if the treadmill remains at a fixed angle throughout an experiment, however this is not always the case.

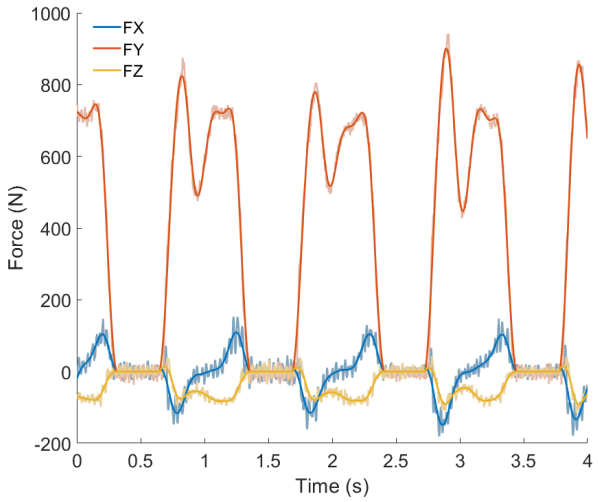

Figure 2.7: Raw & processed samples of GRF data. We show the processed force components in solid colours and the raw data greater transparency. For ease of comparison we show the raw data transformed to the OpenSim reference frame. This data corresponds to 3 – 4 gait cycles collected during steady walking with no incline.

Once both the centre of pressure and torques have been computed, we rotate the ground reaction forces to match the tilt of the treadmill. To summarise, the post-collection data processing procedure for ground reaction force data is as follows:

1. Transform to OpenSim coordinate system.
2. Perform gravity compensation.
3. Filter using a 6 Hz Butterworth filter.
4. Threshold based on the vertical GRF component ($f_y > 40$N).
5. Compute centre of pressure and torque vectors.
6. Rotate GRFs to match treadmill inclination.
7. Export to an OpenSim readable format.

In Figure 2.7, we show the result of the GRF processing procedure on a sample of treadmill data collected in the gait lab.

2.3 Electromyography

Electromyography is the process of measuring the electrical activity of muscles. The signals resulting from this technique are called electromyograms, however

they are most often described in abbreviated form as EMG signals. Typically measurement of EMG signals occurs via electrodes which interface with the muscles of interest, and a grounded electrode which provides a voltage differential. These electrodes are either placed on the skin covering the muscle to be studied, in which case the methodology and signals are termed surface EMG, or they are inserted directly in to the muscles, which is known as intramuscular EMG. Surface EMG data is noisy and typically only works well for muscles which are close to the surface of the skin. Intramuscular EMG achieves a cleaner signal and can target deeper muscles, but requires invasive surgery to insert the electrodes [47].

EMG signals can provide an approximation to the level of activation experienced by a muscle, which in turn is related to the magnitude of force that muscle is currently producing. They have been used widely in fields involving human movement: for example, quantifying muscle behaviours during gait at various speeds [48–50]; sensors for classification of intended movements in the control algorithms of upper-limb prostheses [51]; and as a feedback mechanism for exoskeleton controllers intended to minimise human effort [52].

2.3.1 Hardware

At the ATR Lab in Kyoto, Japan, a custom EMG sensing kit was used which comprised two electrodes and a battery pack wired in to a microcontroller (Figure 2.8a). A third adhesive electrode was affixed to the elbow bone so as to provide a reference zero voltage and ground the incoming EMG signals. Signals were recorded at a frequency of 150Hz.

At the Edinburgh Centre for Robotics, a more advanced wireless EMG sensing kit known as a Trigno Avanti system[10] (Figure 2.8b) was used, consisting of a base station together with a set of 16 wireless sensors with EMG electrodes and inbuilt IMU sensing. The base station was integrated with the Vicon Lock+ box enabling synchronised measurement of up to 16 EMG channels at 1000Hz.

[10] Delsys, Massachusetts, USA.

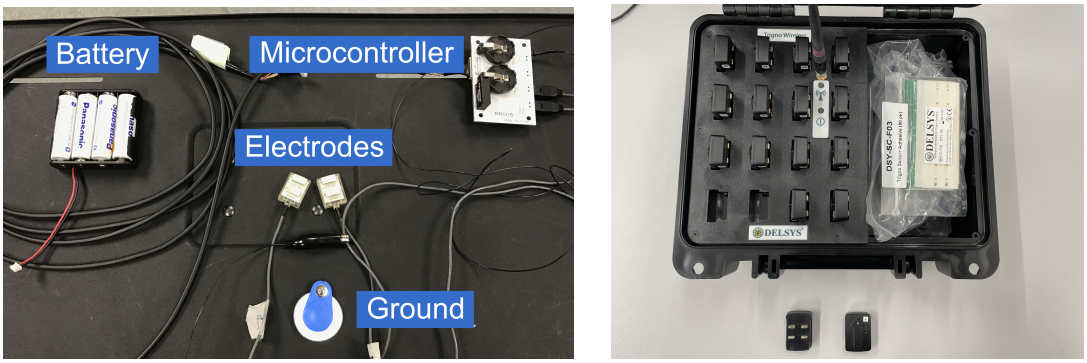

(a) (b)

Figure 2.8: **(a)** The custom EMG sensor kit at the ATR lab. **(b)** The Delsys Trigno EMG system in use at the University of Edinburgh gait lab. The image shows the base station as well as two electrodes.

2.3.2 Data Processing

In this thesis, EMG sensors are used to obtain an estimate of the effort expended by a muscle, or the subject as a whole, in response to some form of robotic assistance. We are significantly more interested in the moving average of the EMG signal rather than the timing of muscle activations. Therefore, our EMG signal processing is focused on smoothing the raw data to produce the linear envelope of the signal.

First, low and high frequency noise is removed from the signal via band-pass filtering. Low frequency noise can occur due to perspiration or gradual movement of the sensors, while some level of high frequency noise appears due to ambient EM radiation and the electronics within the electrodes themselves [53]. The exact values of lower and upper frequency cut-offs are muscle dependent, but should lie within the range $[5, 300]$. Next, the resultant signal is rectified in order to ensure a strictly positive waveform. Finally, we again filter the data - this time with a low pass filter at 6 Hz - to produce the smoothed shape, traditionally termed the linear envelope of the signal. Note that the rectification step is required as EMG signals are naturally zero-mean, and without this step our smoothed signals would cancel out to the line $y = 0$ [54, 55].

To summarise, the sequence of processing steps involved in our analysis of EMG signals is as follows:

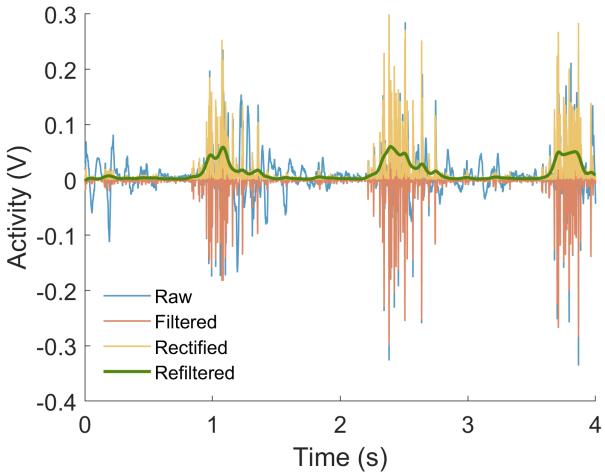

Figure 2.9: Raw & processed samples of EMG data. We show the progress from raw EMG data to the linear envelopes via filtering, rectification, and re-filtering. This data corresponds to 2 – 3 gait cycles collected from the hamstrings during steady walking with no incline.

1. Band-pass filtering of the signal with a zero-lag, 2^{nd} order Butterworth filter and muscle-appropriate lower & upper threshold frequencies.

2. Rectification of the signal.

3. Low-pass filtering of the rectified signal with a zero-lag, 2^{nd} order Butterworth filter at a frequency of 6Hz.

In Figure 2.9, we show the result of the EMG processing procedure on a sample of data collected in the gait lab.

2.4 Calorimetry

Humans without gait pathologies are able to optimise their gait pattern over a range of speeds in order to reduce the energetic cost of walking [14]. Increasingly, exoskeletons and other assistive robotic devices are being developed to impart this ability, via mechanical means, to those with gait pathologies or muscle weakness, or indeed to further improve the energy efficiency of locomotion in healthy people. Commonly, when assessing the efficacy of such devices, energy consumption is quantified via the use of indirect calorimetry.

Indirect calorimetry is a method for estimating the amount of energy consumed by the human body over time. To do this, the rate of oxygen consumed by the body is measured and converted in to metabolic rate. One commonly

Figure 2.10: A subject wearing the Cortex Metamax 3BR2 portable calorimetry system.

used approximation is the following relationship from Brockway [56]:

$$V_e = \frac{4.184}{60}(3.972 + 1.078R)\dot{V}O_2, \tag{2.6}$$

where R is the respiratory exchange ratio (CO_2 production/O_2 uptake), and $\dot{V}O_2$ is the mean relative oxygen uptake measured in ml/min/kg, meaning V_e has units of W/kg. Note that here we have used a subscript to denote experimentally measured metabolic rate, which we will consider to be an approximation to the ground truth metabolic rate V, which describes rate of energy consumption per unit mass.

There are a number of methods for performing indirect calorimetry which vary in levels of confinement — from fully enclosed to open-circuit systems [57]. The most portable systems are wearable devices which compare breath-by-breath measurements of exhaled gases to a reference gas of known composition. Such systems may be less accurate than stationary calorimetry devices, but offer an increase in mobility which is invaluable for sports science [58] or testing other wearable devices such as exoskeletons [59].

2.4.1 Hardware

Calorimetry measurements were recorded using a Cortex Metamax 3BR2 system[11]. This device (Figure 2.10) consists of a facemask connected to a base

[11] Cortex, Leipzig, Germany.

station, worn on the chest, which communicates wirelessly with PC software. Rather than recording data at a fixed frequency, quantities of interest are measured on a breath-by-breath basis. For our purposes, where our interest lies in approximating metabolic rate via Equation (2.6), the useful quantities were oxygen uptake ($\dot{V}O_2$) and respiratory exchange ratio (R). Prior to usage the calorimetry system was calibrated against gases of known composition.

2.4.2 Data Processing

As illustrated in Figure 2.11, calorimetry measurements are typically noisy and low frequency, with portable systems taking measurements on a breath-by-breath basis. In addition, there is a significant lag between instantaneous energy usage and the metabolic rate measured via calorimetry, due to various delays in the biomechanical processes underpinning energy production [60]. Consequently, common methods for approximating metabolic cost via calorimetry inevitably require long measurement times. Under the most widely used approach, termed *steady-state approximation*, a fixed amount of time is allowed for physiological acclimatisation after every change in walking con-

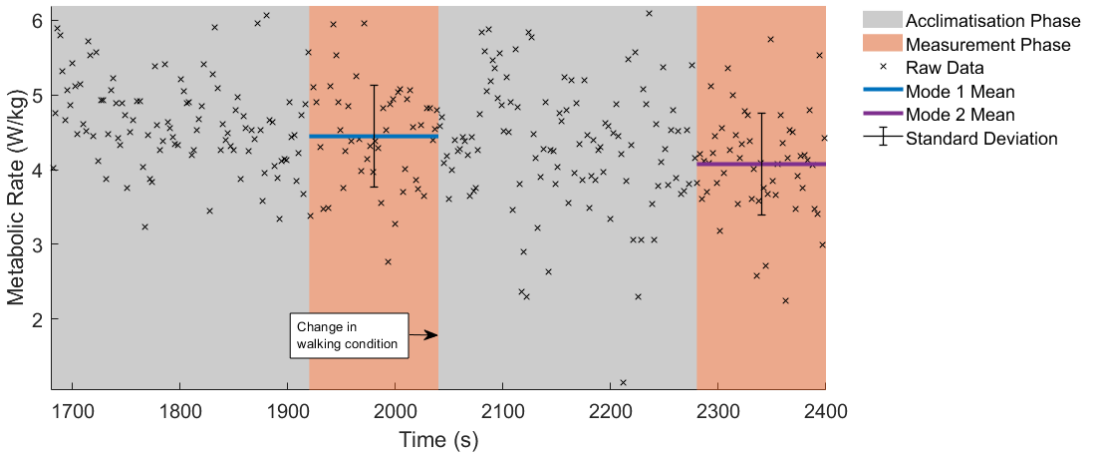

Figure 2.11: Raw & processed samples of calorimetry data. Here, we show data collected during assisted walking; each cross corresponds to data from a single breath, At a time of 2200s, the exoskeleton assistance mode is changed, inducing a reduction in the mean metabolic cost of walking by the end of the 6 minute measurement period. Note the high variance present in the raw data.

Combined Data Processing

After the data-specific processing steps outlined in Sections 2.1.2 - 2.4.2, a number of combined processing steps can be required depending on how the gait data will be used. These steps include:

1. *Synchronisation* — correcting for time delays in one or more data streams. This is a simple but nevertheless important process; particularly with marker and GRF data, where small temporal offsets can lead to large errors in joint torque estimation.

2. *Speed compensation* — accounting for any relative motion within the laboratory reference frame. Here, this is exclusively used to correct for the motion of the treadmill belts, which is important when considering certain aspects of gait such as centre of mass movement.

3. *Gait segmentation* — splitting gait data in to discrete elements termed *gait cycles*. Typically, a full gait cycle is defined as the period between consecutive heel strikes of the same foot. The concept of gait cycles will be discussed in more detail in Chapter 4.

These combined processing methods are implemented in the *Motion Data Processing* toolbox (see Footnote 4).

dition. After this period, the subject is assumed to be in a steady state of O_2 production. Then, additional data is collected and averaged to produce the steady state approximation of metabolic cost. Typical collection times are not less than 3 minutes for the acclimatisation phase and 2 minutes or greater for the data collection phase [9, 61, 62]. In this thesis we use a collection period composed of 4 minutes for acclimatisation and 2 minutes for collecting measurement data. The calculation of steady-state metabolic cost from raw breath-by-breath measurements is illustrated in Figure 2.11.

2.5 The Active Pelvis Orthosis

The Active Pelvis Orthosis (APO) is a rigid pelvis exoskeleton which is designed to offer flexion and extension assistance at the hip joint during walking [63]. It was developed at The BioRobotics Institute of Scuola Superi-

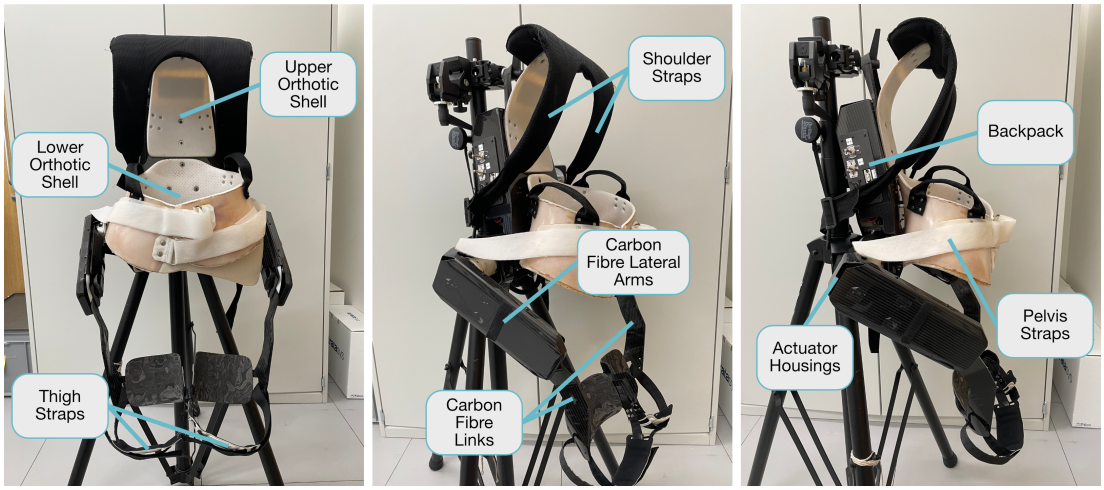

Figure 2.12: A series of closeup images of the APO illustrating the various components which comprise the device. Labels indicate the position of the orthotic shells, fastening straps, and the three main components of the exoskeleton itself: the backpack, actuator housings, and carbon fibre lateral arms.

ore Sant'Anna (Pisa, Italy); the technology is currently licensed to IUVO Srl (http://www.iuvo.company, Pontdera, Italy). The version of the APO used in this study is an evolution of an earlier design [63], which is now fully portable featuring an on-board battery with a total mass of 6.8kg.

The physical structure of the APO consists of a backpack segment, which houses the battery and internal electronics; housings for the actuation units; two carbon fibre lateral arms which contain a 4-bar power transfer mechanism [64]; and two carbon fibre links which interface directly with the human thighs. Two orthotic shells attached to the backpack help to distribute the weight from the device evenly over the subject. The exoskeleton is secured to the wearer via a series of straps: one securing each thigh to the corresponding carbon fibre link, two straps securing the shoulders to the upper orthotic shell, and two further straps which secure the lower orthotic shell to the pelvis. The components of the APO are labelled for reference in Figure 2.12.

The APO is driven by two series elastic actuation units which drive flexion and extension assistance on either side of the device [63]. Each actuator contains a 100 W DC motor in series with torsional spring of stiffness 100 Nm/rad. A harmonic drive and 4-bar mechanism are used for gear reduction and power transmission, respectively. More detail on the actuation system is

Table 2.1: APO Technical Specifications

Mass (kg)	Torque Limits (Nm)		Joint Limits (°)	
	Hardware	Software	Hardware	Software
6.8	±35	±15	$[-27°, 108°]$	$[-25°, 85°]$

provided by Giovacchini et al. [63]. Each actuation unit contains an absolute encoder, which measures the angle of each hip, as well as an incremental encoder which measures the deflection of the torsional spring, which is used in combination with the known spring stiffness to compute the torque at each joint. The APO is capable of producing a peak torque of 35 Nm [63], however for safe and consistent operation a limit of 15 Nm of peak torque is recommended [64]. In our work, we found a limit of 10 Nm more suitable to maintain consistent operation of the device. The exoskeleton is controlled via a software interface built in LabView which allows access to a low-level torque controller [63]. The absolute limits for extension and flexion angle of the carbon fibre links are $-27°$ and $108°$, respectively. However, software limits are in place to limit the range of motion to $[-20°, 85°]$ in practice for purposes of safety. The technical specifications of the APO provided in this section are summarised in Table 2.1 for ease of reference.

The torque sensing capabilities of the APO are used to enable a low-level torque controller which tracks desired torques, τ_{des}, using PID control. The device also supports a number of high-level control modes by default, two of which were used extensively throughout this work. These control modes are described next.

2.5.1 Transparent Mode

In this mode, the APO is commanded via the low-level torque controller to apply zero torque [63]; that is, we specify $\tau_{\text{des}} = 0$. This causes the device to account for its own natural joint resistance, and provide neither assistance nor resistance to the wearer [65]. Data collected from subjects experiencing this control mode is used to quantify the effect of device inertia on gait, independent of the effects of assistance, and so this control mode serves as a good

baseline for the evaluation of APO-assisted locomotion.

2.5.2 Adaptive Oscillator Mode

This mode is designed to provide assistance to drive the wearer naturally towards their intended future joint angle. The APO applies an assistive torque according to the following relationship:

$$\tau_{\text{des}} = K_v(\theta(\phi + \Delta\phi) - \theta(\phi)), \tag{2.7}$$

where K_v and $\Delta\phi$ are tuneable parameters known as virtual stiffness and phase lead, respectively, ϕ is the current phase of the gait cycle, and θ is a function which translates current phase in to an approximation of the current hip joint angle [63]. In other words, this control scheme applies torques proportional to the difference between current and future joint angles, where the future angle is determined by the phase lead, and the difference is scaled by the selected virtual stiffness. Key to this control mode is the concept of adaptive oscillators [66], which are in general used to provide a zero-delay estimates of periodic signals. In this context, adaptive oscillators are used to track and predict the current phase of the gait cycle based on the periodicity characteristics of the hip joint angle measurements [63].

2.6 The XoR Exoskeleton

The XoR, pictured in Figure 2.13, is a powerful lower-body exoskeleton robot developed by ATR in Kyoto, Japan. The XoR has 14 joints in total, of which 6 are actuated (the hip, knee and ankle flexion degrees of freedom). These joints are powered via a hybrid actuation system involving both DC motors and pneumatic artificial muscle (PAM) actuators [67]. Depending on whether the PAM system is in use, which requires additional valves to be fitted, the device weighs between 20 and 25 kilograms. In terms of sensing, the XoR features position encoders at each actuated degree of freedom. The technical specifications of the XoR are summarised for reference in Table 2.2.

The XoR is somewhat unique in that it features a degree of customisability in its design. More specifically, it features 4 adjustable cuffs which attach to

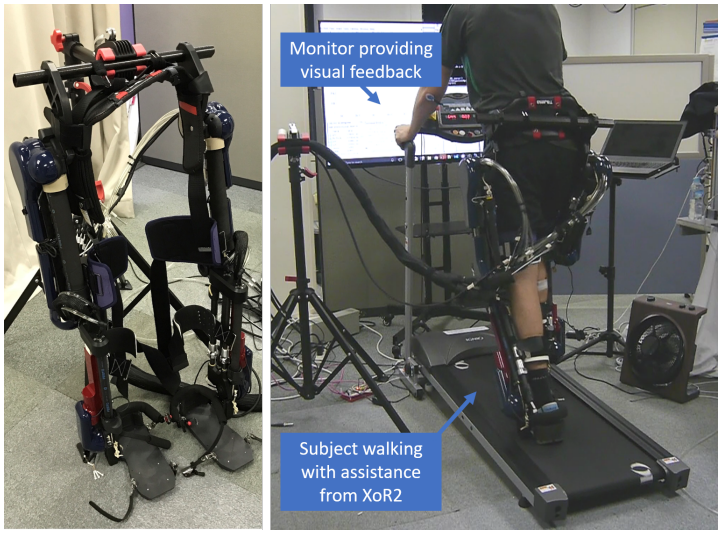

Figure 2.13: **Left:** the XoR exoskeleton. **Right:** a snapshot during a data capture. A subject is wearing the XoR while walking on a treadmill, with a monitor providing visual feedback so the subject can attempt to track the reference trajectory.

Figure 2.14: A close-up view of the thigh and shank cuffs on the XoR. Each cuff can be adjusted vertically on the shaft to which it is attached.

Table 2.2: XoR Technical Specifications

Mass (kg)	Torque Limits (Nm)			Joint Limits (°)		
	Hip	Knee	Ankle	Hip	Knee	Ankle
20	±60	[−60, 20]	±37	[−120, 30]	[0, 120]	[−60, 40]

the left/right thigh and shank of the user, providing a structural link between the human and robotic systems (see Figure 2.14).

For the investigation presented in this thesis, a simple PD controller was implemented as an assistance controller for the XoR. Reference trajectories were collected from the subject walking at a steady pace on a treadmill, using

the on-board joint encoders. The pneumatic actuators were disabled in order to simplify the low-level control problem, leaving only the 6 DC motors which were limited to ±5V in order to protect the motors. Walking experiments were undertaken on a treadmill platform with no integrated sensing.

2.7 Hardware Reference

This section is intended to act as a point of reference for the hardware used throughout this thesis. In Table 2.3 and Table 2.4 we summarise key characteristics of the motion capture equipment and exoskeleton hardware.

Table 2.3: Motion Capture Equipment Reference

Name	Measurement	Frequency (Hz)
Vicon System	3D position of each marker in capture volume	100
Treadmill	3D force and moment at the origin of each plate	1000 (600)
ATR EMG	EMG signals (up to 2 channels)	150
Delsys Trigno	EMG signals (up to 16 channels)	1000 (2000)

Frequencies listed in parentheses are those obtained when **not** *using the Vicon Lock+ box for synchronisation, as discussed in Section 2.1.*

Table 2.4: Exoskeleton Hardware Reference

Name	Joints (**A**)	Sensing	Frequency (Hz)
APO	4 (**2**)	Position, Torque	100
XoR	14 (**6**)	Position	100

*We use (**A**) to denote the number of active joints i.e. those which can be actuated. For detailed information on the APO and XoR joint and torque limits, see Table 2.1 and Table 2.2, respectively.*

Chapter 3

Modelling Human-Exoskeleton Systems

The human body can be modelled generically as a connected system of bodies, joints and muscles[12] [68]. Each body (for example the thigh or femur) is described by its mass, centre of mass and inertial properties, while joints are defined relative to the parent and child bodies which they connect. Joints can be one-dimensional hinge joints (e.g. the ankle), three-dimensional ball-and-socket joints (e.g. the hip), or in general could have even more complex definitions (e.g. the knee). The root body is typically the pelvis, which is connected to the ground frame by a 6 degree of freedom free joint.

Previous works have identified the appropriate anthropometry [69], joint

[12] Additional structures are ligaments which connect bodies (bones) together, and tendons which attach muscles to bones.

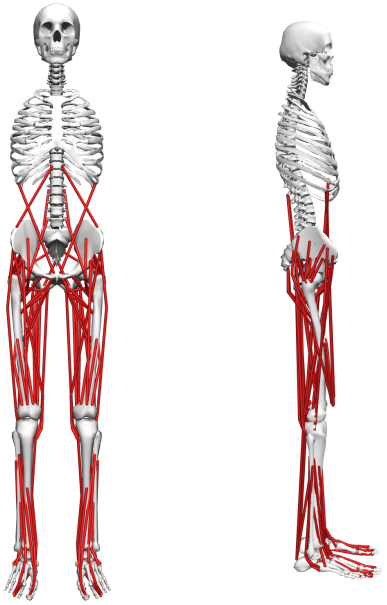

Figure 3.1: The *gait2392* model, used primarily for musculoskeletal analysis of the lower body. The model consists of 23 joints driven by 92 musculotendon actuators.

definitions [38, 70], and muscle properties [71, 72] corresponding to the human body through simulation and comparison with experimental data. These works were incorporated in to a specific human musculoskeletal model by Frank C. Anderson, Scott L. Delp, Ajay Seth and Darryl Thelen, which is referred to as the *gait2392* model [73] and is pictured in Figure 3.1. This is a rigid body system, consisting of 12 bodies, 12 joints representing 23 degrees of freedom, and 92 musculotendon actuators to drive the joints. Due to the simplification of the upper-body in to one 'torso' segment, the model is intended for the modelling of human movements which are dictated primarily by muscles in the lower extremity. The *gait2392* model has been used both in its default form as a tool for simulating human gait [74], and also as a base on which to build customised models, such as those which can more explicitly represent the dynamics of the upper-body [75, 76]. In theory, OpenSim models can contain an arbitrary number of bodies and muscles, and therefore, moving forward, we will consider a generic musculoskeletal model with n degrees of freedom and m muscles.

3.1 Constraining an Exoskeleton to a Musculoskeletal Model

Implementing a fully actuated model of a human-exoskeleton system would require a non-trivial coupling of the exoskeleton joints with the joints of the user. Instead, we employ a strategy of splitting the exoskeleton in to two components: bodies, which are attached to a model in such a way[13] as to properly represent the inertial properties of the full human-exoskeleton system; and constraint forces. Note that under this approach the number of degrees of freedom of the human-exoskeleton system model remains unchanged from that of the generic human model, however due to the addition of the exoskeleton as a combination of bodies, the dynamic parameters $\mathbf{M}$, $\mathbf{b}$, and $\mathbf{g}$ will all change. In addition, we must introduce a new component, $\boldsymbol{\tau}_{\mathrm{e}} \in \mathbb{R}^n$, which gives the system torque due to the actuation of the exoskeleton. From the starting point of the human-centric relationship outlined in Equation (1.6), we make a number of modifications which results in the following system of equations:

$$M_c(\mathbf{q})\ddot{\mathbf{q}} + \mathbf{c}_c(\mathbf{q}, \dot{\mathbf{q}}) + \mathbf{g}_c(\mathbf{q}) = \boldsymbol{\tau}_h + \boldsymbol{\tau}_g + \boldsymbol{\tau}_e, \tag{3.1}$$

$$\boldsymbol{\tau}_e = \mathbf{E}(\boldsymbol{\mu}). \tag{3.2}$$

Note that we have changed our subscript from h to c to denote quantities which now represent the *combined* human-exoskeleton system. The exoskeleton motor torques are mapped on to a generalised torque component $\boldsymbol{\tau}_e$ by $\mathbf{E}$, which for now we leave as a generic black box function known as a *force model*. At this stage, it is not obvious precisely how $\boldsymbol{\tau}_{\mathrm{e}}$ should be calculated, except as some function of the exoskeleton motor torques.

3.2 Musculoskeletal Dynamics

In Equation (3.1), the human force contribution still implicitly depends only on torque commands, stored in $\boldsymbol{\tau}_h$. To consider muscle-control within our

[13] Examples of suitable attachment methods include weld joints (which allow no relative movement) for fixations which are relatively rigid, or spring-damper forces if compliant interaction is required.

System Models

In this Chapter we discuss two different types of models: those describing the relationship between the bodies, joints and muscles comprising a human or human-exoskeleton system; and those describing how the joint-space forces due to an exoskeleton are related to its motor torques. In order to clearly distinguish between types of model, those of the first type will be described more verbosely as *system models*.

optimisation problem, we must introduce the following additional constraints:

$$\boldsymbol{\tau}_h = \mathbf{F}\left(\mathbf{f_0}, \mathbf{l}, \dot{\mathbf{l}}\right)^{\mathsf{T}} R(\mathbf{q})\,\mathbf{a}, \tag{3.3}$$

$$\dot{\boldsymbol{l}} = \mathbf{C}(\mathbf{a}, \mathbf{l}, \mathbf{q}, \dot{\mathbf{q}}), \tag{3.4}$$

$$\dot{\boldsymbol{a}} = \mathbf{A}(\mathbf{a}, \boldsymbol{\nu}), \tag{3.5}$$

$$\boldsymbol{\nu}_{\min} \leq \boldsymbol{\nu} \leq \boldsymbol{\nu}_{\max}. \tag{3.6}$$

Together, Equations 3.3 - 3.6 comprise the equations of musculoskeletal dynamics. The m-dimensional vectors $\mathbf{f}_0$, $\mathbf{l}(t)$, $\mathbf{a}(t)$ and $\boldsymbol{\nu}(t)$ are maximum isometric force, fibre length, muscle activation and muscle excitation, respectively. Muscle excitations are neural commands produced by the central nervous system, which affect the level of muscle activations according to an *activation dynamics* model, A. Muscle *contraction dynamics*, C, relates the rate of change of muscle fibre length to the current state & level of activation. The force produced by each muscle is determined by its maximum isometric force, fibre length, and shortening velocity according to the *force-length-velocity* surface, F. Finally, these isometric forces are mapped on to the joint space of the rigid-body model by the muscle moment arm, $R \in \mathbb{R}^{n \times m}$. The isometric force produced by a muscle is distributed over the joints it crosses, with a relative weighting described by R.

In practice, the OpenSim API was the primary method used throughout this thesis to solve the equations of musculoskeletal dynamics and perform other operations related to musculoskeletal modelling and simulation. Further details of the tools and algorithms provided by OpenSim are provided in Appendix A.

3.3 The Human-APO Model

Thus far this chapter has remained agnostic to any specific exoskeleton or human musculoskeletal model. Here, we provide specific implementation details for a model of a human wearing the APO exoskeleton[14], which we will hereafter refer to as the *human-APO* system model. The majority of experimental data presented in this thesis was collected using the APO, and therefore this model underpins much of the simulation-based analysis presented in subsequent sections and chapters.

The human-APO system model consists of the joint-space version of the *gait2392* model, combined with the inertial properties of the APO. The APO CAD files, mass, and inertia properties were supplied by the manufacturer of the APO. To constrain the APO to the human system model three sets of weld constraints (constraining any relative translations and rotations between two bodies) were applied to the model: one located between the backpack and the pelvis, and the other two between each APO link and the corresponding thigh. The position of the weld joint connecting the pelvis and backpack is chosen so that the system model accurately represents how the APO is worn in reality. The position of this weld joint then determines the location of the other two, so that the APO links and the APO group bodies meet at the appropriate point without clipping. The generic human-APO model is calibrated for a particular subject via a scaling step which minimises the squared error between model markers and experimental markers from motion capture; more information about this process is provided in Appendix A.4.

In Figure 3.2, the human-APO system model is shown, with labels illustrating the different APO bodies and the locations of the weld joints which constrain the APO to the human system model.

3.4 Interaction Dynamics

In the ideal case, we can assume that the entirety of the energy (or torque) generated at exoskeleton joints can be transferred to the human joints to which they are attached. Under this assumption, the force model $\mathbf{E}$ from Equation

[14] A detailed description of the APO hardware can be found in Section 2.5.

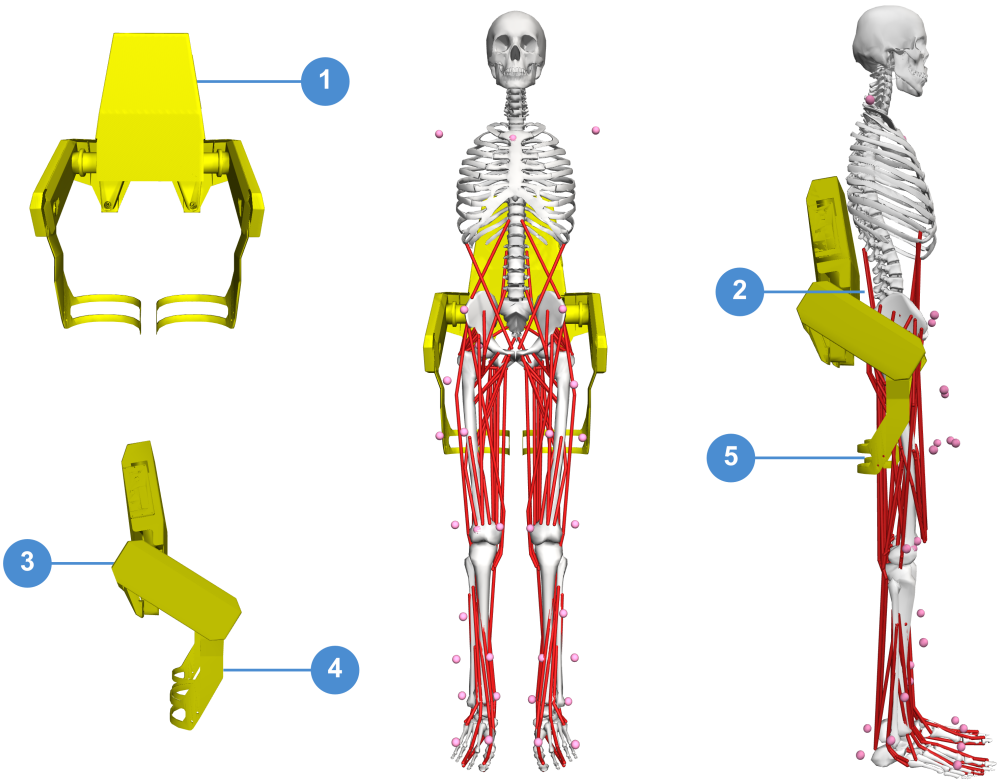

Figure 3.2: An overview of the human-APO model. The labelled components of the model are as follows: (1) APO backpack; (2) weld constraint between APO backpack and pelvis; (3) right motor housing; (4) right link, which interfaces directly with the human thigh via a weld joint (5).

(3.2) would become a simple mapping from the space of exoskeleton motor torques to the space of human joint torques.

In practice however, perfect transmission of energy from exoskeleton to human is not achievable. In this section, we will discuss the effects of joint misalignment and compliance in human-exoskeleton torque transfer, as well as corresponding modelling approaches which can help to account for these phenomena. Results based on musculoskeletal simulations from experimental motion data are presented, which allow for qualitative discussion of the merits of these modelling approaches. We will focus specifically on APO-assisted locomotion, modelled with the human-APO system model.

3.4.1 Joint Misalignment

The problem of joint misalignment is well known when dealing with physically coupled systems e.g. humans wearing exoskeletons [77–79]. If joints are perfectly aligned, exoskeleton forces can be modelled as equal and opposite torques applied to the relevant exoskeleton and human bodies. However, the presence of joint misalignment results in imperfect transmission of torque from the exoskeleton to the human user [80], ultimately resulting in reduced torque about the human joint and the introduction of undesirable forces parallel to the human limb, which can cause discomfort or unintended changes to muscle activation patterns [81].

3.4.2 Compliant Torque Transmission

Due to the presence of compliance in human-exoskeleton systems, largely due to flexible straps and soft biological tissues, power loss occurs between the torques generated by the exoskeleton and the torques experienced by the human subject. A relatively limited number of previous studies have investig-

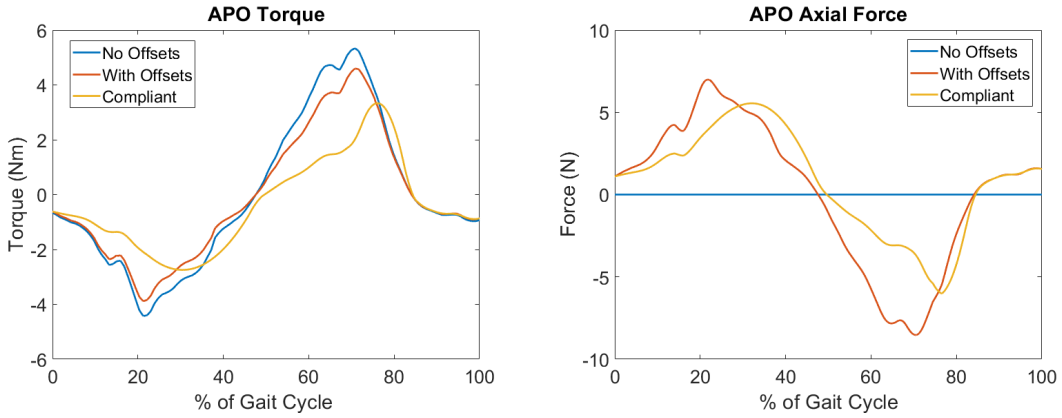

Figure 3.3: A graphical representation of the APO force models for a single gait cycle. The ideal force model (*With Offsets*) and compliant force model (*Compliant*) are shown relative to the measured APO torques (*No Offsets*). **Left:** the torque applied to the human femur as a result of the transverse force applied by the exoskeleton. Note the delayed onset of the peaks in the compliant force model. **Right:** the introduction of undesired interaction forces directed parallel to the thigh. These forces are introduced due to the presence of joint offsets, which introduce an axial component to the force vector.

ated these interface dynamics in more detail, using a mix of kinematic and load sensing measurement systems to estimate the visco-elastic properties of the human-exoskeleton system [82] or the relative timing and magnitude of power loss [83].

The second study, which posits what we will hereafter refer to as the **compliant** torque transmission model, assumes that the energy exchange is subject to absorption-return dynamics [83]. Under this model, exoskeleton assistance is partitioned in to phases categorised as **loading** while the torques are increasing in magnitude and **unloading** while the torques are decreasing in magnitude. A percentage A of the power generated by the exoskeleton during loading phases is absorbed by the soft tissue in the system, and a percentage of this absorbed power, R, is returned during the next unloading phase. This results in a temporal offset in peak torque between the ideal and compliant models. In Figure 3.3, a comparison between the ideal and compliant torque models is displayed for a single reference gait cycle. The absorption and return rates were chosen to be $A = 0.55$ and $R = 0.75$, respectively, to match the observations of Yandell et al and allow for qualitative discussion on the compliant human-APO interface.

3.4.3 Methodology

Determining Joint Offsets

The design of the APO is such that the exoskeleton joints should closely align with those of the human [63], however, it is not realistic to expect perfect alignment. By fixing a reflective marker on the rear of the exoskeleton, it was possible to identify the offsets between the human and exoskeleton joints for each subject. The protocol for calculating the offsets is outlined below.

1. Measure the distance from a fixed reflective marker on the back of the APO to the left and right exoskeleton joint centres.

2. Using static pose data which includes this fixed marker, calculate the position in the ground frame of the left and right exoskeleton joint centres for each subject.

Subject	Right hip offset (m)		Left hip offset (m)	
	x	y	x	y
S1	0.0818	0.0158	0.0817	0.0097
S2	0.0546	-0.0222	0.0621	-0.0288
S3	0.0847	0.0127	0.0843	0.0141
S4	0.0770	0.0057	0.0636	0.0105
S5	0.0929	0.0067	0.0648	0.0017
S6	0.0615	-0.0017	0.0584	0.0006
S7	0.0881	0.0209	0.1081	0.0213
S8	0.0753	0.0024	0.0580	0.0022

Table 3.1: The static joint offsets between the hip joints of each subject and the APO joint centres. Note that the x axis is directed forward from the pelvis and the y axis is directed upwards.

3. Using the reflective markers situated on the pelvis, coupled with a variation of the Harrington method [84] for estimating the hip joint centre, calculate the locations of the left and right human hip joint centres in the ground frame.

4. Calculate the offset between the exoskeleton and human joint centres.

The offsets for each subject are summarised in Table 3.1.

Experimental Protocol

The force models derived in Sections 3.4.1 - 3.4.2 were tested on exoskeleton-assisted locomotion data from 7 subjects walking with assistance from the APO. This investigation required static marker data for each subject and motion data (marker trajectories and ground reaction forces) of both assisted and unassisted walking over a range of walking conditions.[15] The tested walking conditions included four assistance scenarios: walking without the APO (NE); walking with the APO in transparent mode (ET); walking with APO assistance assuming no compliance (EA-I); and walking with the APO assistance assuming compliance (EA-C). In addition, five walking contexts were investigated: walking at baseline speed (BW); walking at an incline of 5 degrees (UW);

[15]The data used was a subset of a full dataset which is outlined in more detail in Chapter 4.

walking at an incline of -5 degrees (DW); walking at 1.2 × baseline speed (FW); and walking at 0.8 × baseline speed (SW).

For each combination of assistance mode and walking context, a metabolic analysis (see Appendix A.7) was run to determine the change in energy rate over the set of tested walking scenarios.

Statistical Analysis

The number of samples for each combination of muscle, walking context and assistance scenario was 35 (5 gait cycles × 7 subjects). For each muscle in Table 3.2, a two-way ANOVA was used to investigate the effective of assistance mode and walking context on the power output of each muscle. To determine statistical significance, the MATLAB multiple comparison procedure 'multcompare' was used with the comparison type based on Tukey's honestly significant difference criterion. The statistical significance level was set at $\alpha = 0.05$.

In order to compare the effect of active exoskeleton assistance between different contexts, a one-way ANOVA was performed for each context over all assistance levels and for each muscle in the model[16]. Within each context, the muscles which had significantly different average metabolic power consumption when in non-compliant mode (EA-I) or compliant mode (EA-C) compared

[16]This includes muscles which are not listed in Table 3.2.

Muscle	Actions
Adductor brevis	Hip adduction
Adductor longus	Hip adduction, hip flexion
Adductor magnus	Hip adduction, hip flexion, hip extension
Psoas	Hip flexion
Gluteus maximus	Hip extension, hip rotation
Biceps femoris long head	Knee flexion, hip extension
Rectus femoris	Knee extension, hip flexion
Vastus medialis	Knee extension
Medial gastrocnemius	Ankle plantar flexion, knee flexion
Soleus	Ankle plantar flexion

Table 3.2: The muscles for which a metabolic analysis was carried out, along with their main actions.

Parsing 3D Significance Plots

In Figures 3.4 & 3.5 we show 3D plots that illustrate the behaviour of a quantity over a two dimensional range of conditions. In addition to illustrating the general landscape of the quantity in question, these plots provide information as to the statistical significance of any differences in behaviour between conditions.

To identify whether there is a significant difference between any two conditions on the same axis, check for a line connecting the two conditions on the opposite axis of the plot. As a concrete example, consider the plot for the adductor brevis (Add. brev.) muscle in Figure 3.4. Note that there are two horizontal lines opposite the assistance level axis: one conecting ET and EA-I and one connecting ET and EA-C. This means that there is a statistically significant difference between the metabolic power consumption of the adductor brevis muscle between these combinations of assistance levels. On the other hand, note that there is no horizontal line connecting the BW and UW contexts opposite the walking context axis. This means there is no statistically significant difference in the metabolic power consumption of the adductor brevis when going from baseline walking to uphill walking.

This style of plot is re-used in future chapters to analyse the behaviour of other quantities related to human gait, so it is useful for the reader to familiarise themselves with this process for identifying signficant differences between conditions.

to transparent mode (ET) were identified. The relative change in metabolic power consumption going from transparent mode to active mode was then calculated as a percentage in order to quantify the effectiveness of the exoskeleton assistance.

3.4.4 Results

For each muscle in Table 3.2 the percentage difference in average metabolic power consumption from the baseline condition (no exoskeleton assistance and walking at baseline speed) as a function of walking context and assistance level is demonstrated in Figures 3.4 - 3.5. Additionally, the raw mean and standard deviation values for every context and assistance scenario combination are detailed in Appendix B.2.

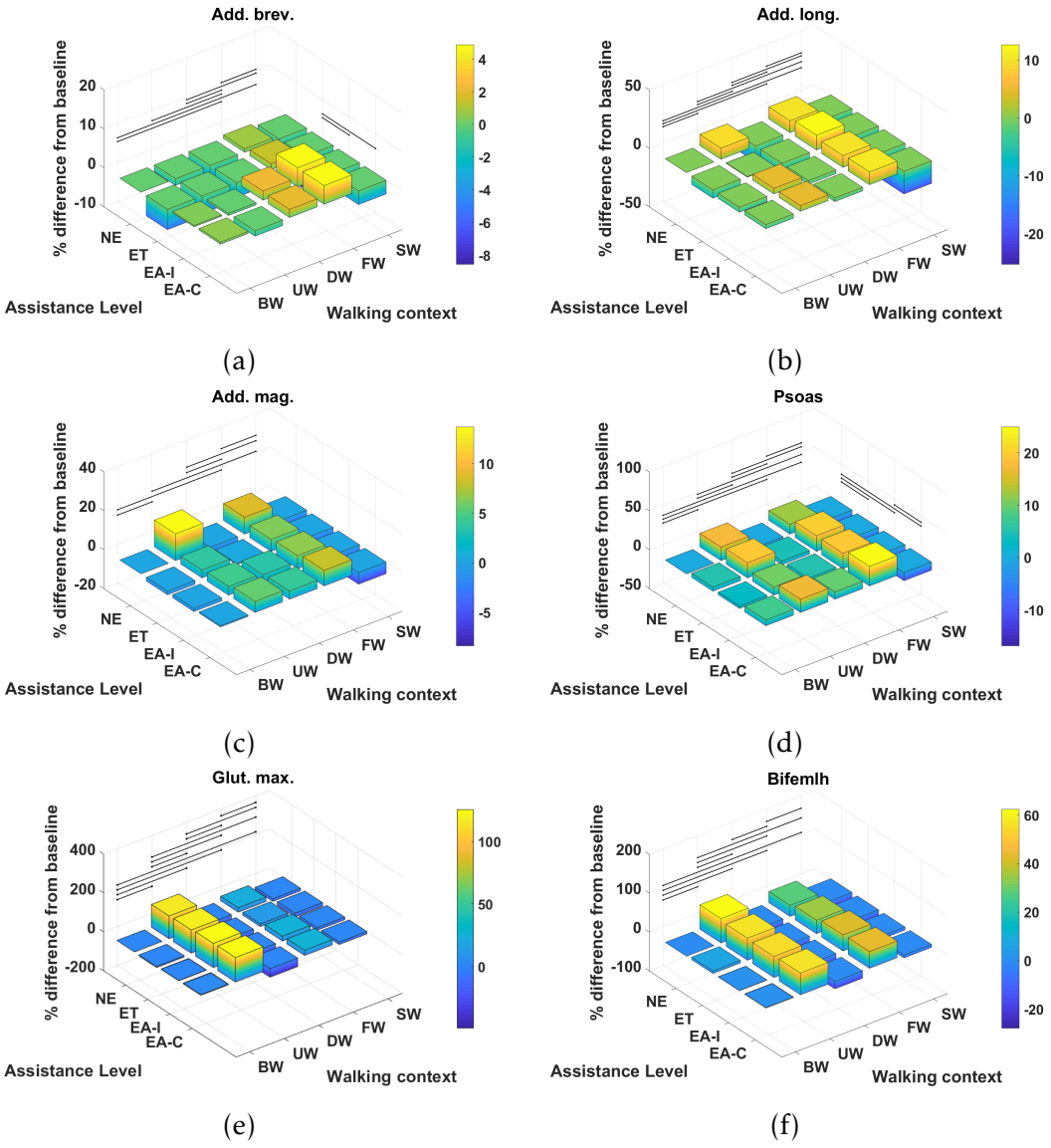

Figure 3.4: The % difference in average metabolic power consumption of the (a) adductor brevis, (b) adductor longus, (c) adductor magnus, (d) psoas, (e) gluteus maximus and (f) biceps femoris long head muscles. Black lines indicate significant differences.

From Figures 3.4 - 3.5, we can see that only one muscle from our subset shows a significant difference in metabolic energy consumption on average over all contexts due to the transition from transparent mode to active assistance, namely the adductor brevis muscle. Five muscles, the psoas, rectus femoris, vastus medialis, medial gastrocnmeius and soleus show significant

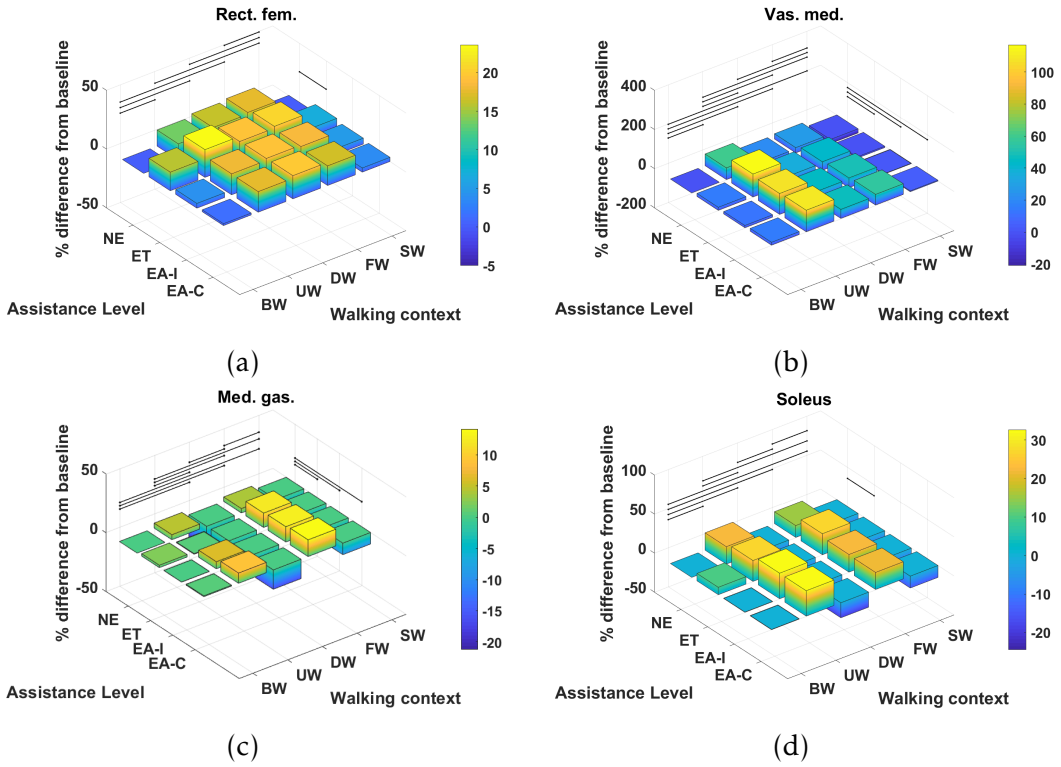

Figure 3.5: The % difference in average metabolic power consumption of the (a) rectus femoris, (b) vastus medialis, (c) medial gastrocnemius and (d) soleus muscles. Black lines indicate significant differences.

differences between the NE and ET assistance levels, which implies the change in metabolic energy consumption of these muscles is attributable to the increased physical load of wearing the exoskeleton rather than the presence of active assistance itself. One muscle, the psoas, shows a significant difference between the APO force models.

The muscles from the full set which were identified via the context-specific one-way ANOVAS to experience a significant change in metabolic energy consumption between the ET and EA assistance levels are listed by context in Table 3.3. Note that significant differences were seen for the uphill walking, downhill walking and slow walking contexts for both force models. Significant differences were seen in the flat walking context, but only when the compliant model was used. No significant differences were seen in the fast walking context. The relative change in metabolic power consumption is shown for the muscles in these contexts in Figure 3.6. The overall effect, calculated from total

significant metabolic energy change in each context, is presented in Figure 3.7. We see from these results that the active exoskeleton assistance has a positive effect in the BW scenario, but only when the compliant APO force model is used. There is a disagreement in the UW context, where the ideal APO force model predicts a net assistance of approximately 8%, whereas the compliant force model predicts that human metabolic energy consumption is increased. The ideal force model predicts that the iliacus and psoas muscles are assisted; the main actions of these muscles is to assist hip flexion. Meanwhile, both force models agree that the active exoskeleton assistance is detrimental in the SW and DW scenarios, where human metabolic energy consumption is seen to increase by between approximately 5% and 12% depending on the walking context and which force model is used.

3.4.5 Discussion

In general, we observed that applying exoskeleton assistance had significantly less effect on metabolic energy consumption than changes in walking context. However, this analysis was limited by the fact that while there were three assistance scenarios, only one of these scenarios explored active assistance, and therefore comparison between different magnitudes of active assistance was not explored. A source of further work could be to collect data using a wider range of virtual stiffness levels, which would allow for an analysis of how the metabolic effect of active assistance varies with assistance magnitude. It should be noted that the motor torques commanded to the APO during active

Baseline walking	Uphill walking	Downhill walking	Slow walking
Adductor brevis	Iliacus	Adductor longus	Adductor brevis
Rectus femoris	Psoas	Adductor brevis	Tibialis posterior
-	Quadratus femoris	-	Biceps femoris long head
-	Medial gastrocnemius	-	Lateral gastrocnemius
-	-	-	Flexor hallucis longus
-	-	-	Peroneus brevis
-	-	-	Peroneus longus

Table 3.3: The muscles which are significantly affected by exoskeleton assistance for each context. Note that no muscles were significantly affected in the fast walking condition.

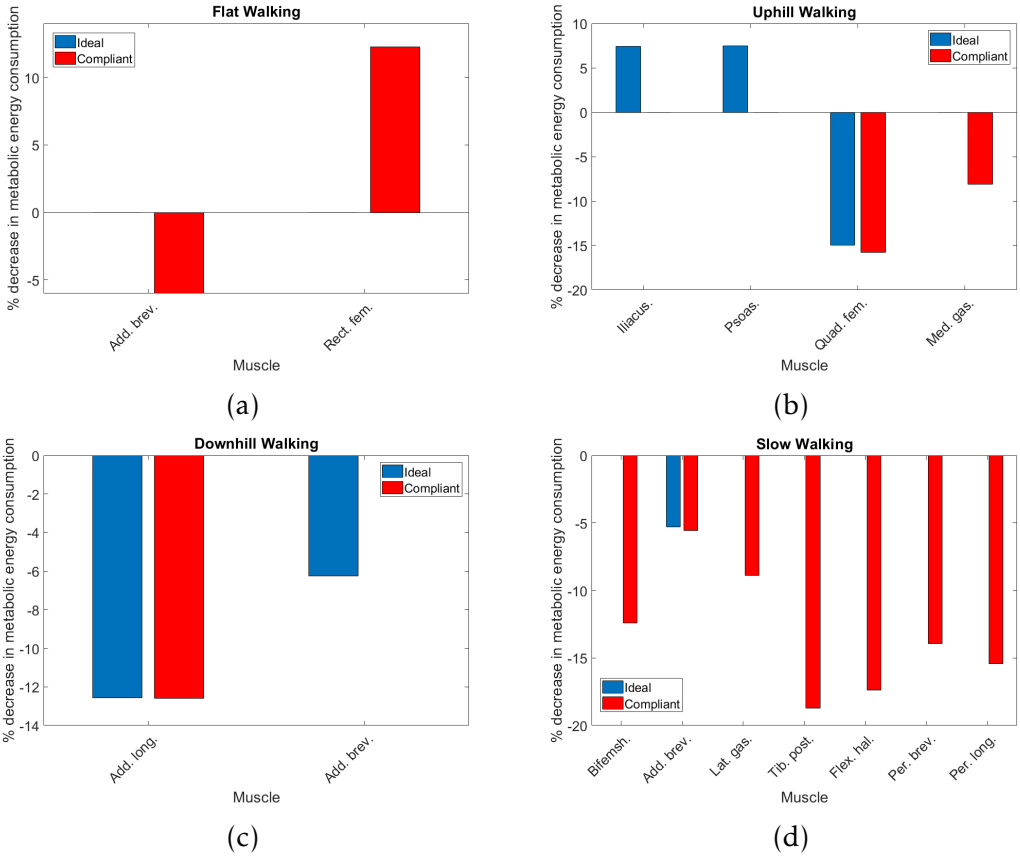

Figure 3.6: The percentage change in average normalised metabolic energy consumption of muscles which show a significant change between the ET and EA assistance modes during (a) flat walking, (b) uphill walking, (c) downhill walking and (d) slow walking. Note that red bars correspond to the compliant force model whereas blue bars correspond to the ideal force model. Absence of data denotes that no significant differences were observed in this case.

assistance trials were already close to the torque limitations in place on the device.

The relative effect of applying exoskeleton assistance was most pronounced in the flat walking, uphill walking, downhill walking and slow walking scenarios. In the latter two of these scenarios, both the ideal and compliant APO force models predicted increased metabolic cost. The compliant model predicted that flat walking benefited from assistance, while the ideal model predicted that uphill walking benefited from assistance. Anecdotally, this result agrees with feedback from subjects following data collection (e.g. the exoskel-

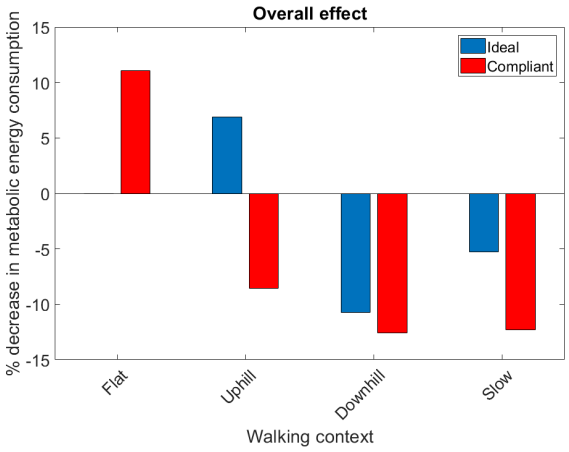

Figure 3.7: The overall metabolic effect of exoskeleton assistance in each walking condition, for both the ideal APO force model (blue) and the compliant APO force model (red). Absence of data denotes that no significant differences were observed in this case.

eton assistance was most beneficial when walking uphill). The negative effect of the exoskeleton when walking at slow speed may be a result of the choice of control algorithm.

It should be noted that the implementation of a compliant APO force model was intended largely as a point of qualitative comparison between the results from the ideal APO force model. Indeed, several differences between the experimental setup used for this work and the work on interface dynamics [83] could lead to differing compliant behaviour in our case. However, these results do suggest qualitatively that including compliance in the system, as certainly is the case for contact between exoskeletons and soft straps or human tissue, can cause marked differences in the effectiveness of exoskeleton assistance. Further work is needed to implement control algorithms which can account for human-exoskeleton interface dynamics in real-time.

Formulation Update

From what we have learned in this chapter with regards to human-exoskeleton system models and simulating musculoskeletal dynamics, we are in a position to update the optimisation-based exoskeleton control formulation from Section 1.1.3. The updated formulation is as follows:

$$\min_{\boldsymbol{\mu}_e} \|\mathbf{q} - \mathbf{q}_d\|, \tag{3.7}$$

$$M_c(\mathbf{q})\ddot{\mathbf{q}} + \mathbf{c}_c(\mathbf{q}, \dot{\mathbf{q}}) + \mathbf{g}_c(\mathbf{q}) = \boldsymbol{\tau}_h + \boldsymbol{\tau}_g + \boldsymbol{\tau}_e, \tag{3.8}$$

$$\boldsymbol{\tau}_e = \mathbf{E}(\boldsymbol{\mu}), \tag{3.9}$$

$$\boldsymbol{\tau}_h = \mathbf{F}\left(\mathbf{f_0}, \mathbf{l}, \dot{\mathbf{l}}\right)^{\mathsf{T}} R(\mathbf{q})\,\mathbf{a}, \tag{3.10}$$

$$\dot{\boldsymbol{l}} = \mathbf{C}(\mathbf{a}, \mathbf{l}, \mathbf{q}, \dot{\mathbf{q}}), \tag{3.11}$$

$$\dot{\boldsymbol{a}} = \mathbf{A}(\mathbf{a}, \boldsymbol{\nu}), \tag{3.12}$$

$$\boldsymbol{\mu} \leq \boldsymbol{\mu}_{\max}, \tag{3.13}$$

$$\boldsymbol{\nu}_{\min} \leq \boldsymbol{\nu} \leq \boldsymbol{\nu}_{\max}. \tag{3.14}$$

Compared to the previous case, we have incorporated the equations of motion of the combined human-exoskeleton system (Equations 3.8 - 3.9), as well as introduced constraints on the variable $\boldsymbol{\tau}_h$ such that the human joints behave as if they are muscle-actuated (Equations 3.10 - 3.12). We also must respect any limitations we have on our ability to apply exoskeleton torques due to motor limits (Equation (3.13)); likewise, we similarly constrain the level of muscle excitation (Equation (3.14)).

Our optimisation variables now consist of exoskeleton torques $\boldsymbol{\mu}$ rather than the human contribution $\boldsymbol{\tau}_h$ from the previous formulation, because while we can command modulations in exoskeleton torque we have no means of *directly* altering the behaviour of the human (though of course we can still use exoskeleton assistance to implicitly alter human behaviour).

Currently we still assume that minimising joint trajectory error, as we specify in the objective function of the above optimisation, is a good strategy for exoskeleton-assisted locomotion. We will see if that is the case in the next chapter.

Chapter 4

Gait Metrics

Gait metrics are quantitative measures of some aspect of walking style. Their use is ubiquitous throughout the study of human locomotion - for example, a highly cited paper from 1953 posited that six determinants (or gait metrics) in particular were responsible for the energy efficiency of human walking [85][17], and in more recent years complex gait metrics have been introduced to gauge the relative severity of gait pathologies [88, 89].

To begin this chapter, we will construct a formalisation of the concept of a gait metric. Then, we introduce the concept of gait cycles, and discuss two important properties — *resolution* and *invariance* — that allow us to determine

[17] The six determinants of gait theory has fared very poorly in recent decades, to the point of being largely discredited [14, 86, 87].

Gait Metrics as Objective Functions

Another way of describing a gait metric is as a real function defined on gait data. With this description, it is clear to see that gait metrics could be candidates for the objective function of the exoskeleton control problem.

which gait metrics in particular are suitable for use in the objective function of our optimisation-based approach to exoskeleton control.

4.1 Definitions

Definition 4.1. *A gait parameter $p_g(t) \in \mathbb{R}$ is a quantitative feature of a gait pattern which dynamically varies with time t. We will use the notation $\mathcal{G}$ to denote the space of gait parameters.*

Gait parameters are typically related to movement of the human body or forces which are directly applied to it. Some example gait parameters are:

- trajectories of experimental markers attached to the body,
- kinematic data (e.g. joint angles throughout a motion),
- external forces acting on the body (e.g. ground reaction forces),
- derived parameters (e.g centre of mass position).

Definition 4.2. *A subject parameter $p_s \in \mathbb{R}$ is a static quantity associated with a particular subject, which may affect gait pattern but nevertheless is independent of it. We will use the notation $\mathcal{S}$ to denote the space of subject parameters.*

Subject parameters are typically descriptors of the human body which are required for normalisation or comparison between subgroups of the general population. Some example subject parameters are:

- age,
- mass,
- height,

- limb lengths or other important kinematic features.

Definition 4.3. *An environmental parameter $p_e \in \mathbb{R}$ is some aspect of the external environment which affects gait pattern but is independent of it, and is not directly associated to a particular subject. It can be either a static or dynamic quantity. We will use the notation $\mathcal{E}$ to denote the space of environmental parameters.*

Environmental parameters encode the walking context in which a gait pattern is observed. This can include factors like:

- speed of a treadmill,
- walking incline,
- ground friction,
- altitude.

Definition 4.4. *A gait metric is a quantitative measure of some aspect of walking style. More formally, it is a function $g : \mathcal{X}^n \to \mathbb{R}$ where $\mathcal{X} \subseteq \mathcal{G} \times \mathcal{S} \times \mathcal{E}$ is the combined space of gait, subject and environmental parameters and $n \in \mathbb{N}$.*

4.2 Examples

One example of a simple gait metric is *step length*, which can be defined as the distance travelled (in the direction of motion) between consecutive steps of the same foot. If the foot location is known at all times, e.g. in simulation, this can be calculated directly; in practice, the information can be tracked using an optical motion capture system or recorded video data. If $p_x(t)$ is the position of a point on the right foot in the x direction, which is the direction of motion, then:

$$L = |p_x(t_1) - p_x(t_0)|\,, \tag{4.1}$$

where L is step length and t_1, t_0 are the timesteps corresponding to consecutive steps. Only gait parameters are involved in the calculation of the step length metric.

Often, it is beneficial to normalise raw gait data relative to the subject in question. For instance, it is common in the literature to normalise step length

relative to subject height [90] or leg length [91], though some studies have used the metric without normalisation [92]. Using h to denote either of these parameters, we have:

$$\bar{L} = \frac{|p_x(t_1) - p_x(t_0)|}{h}. \tag{4.2}$$

In this case, a combination of subject parameters and gait parameters is required for the computation of *normalised step length*.

Environmental parameters appear most commonly as an index — quantifying how gait metrics are affected by a change in walking condition. For instance, a number of studies have investigated the relationship between step length and walking incline [93, 94], which could be considered a distinct *context specific* measure of normalised step length, $\bar{L}_I$, where I denotes the incline index. Such metrics can be useful in quantifying fall risk [95].

4.3 Gait Cycles

Gait patterns can be broken down in to a cyclical sequence of events [96, 97]. These events are typically different between gaits of a different type. For example, walking gait is characterised by the presence of a double stance phase (when both feet are in contact with the ground), whereas running gait is characterised by the presence of two double swing phase (when neither foot is in contact with the ground) [98]. In this thesis we are primarily concerned with walking gait, the features of which are outlined in Figure 4.1.

A gait cycle is the period between two consecutive instances of the same gait event. Conventionally, it is common to designate the heel strike event to mark the beginning of a gait cycle[18]. However, other events can be selected if this is beneficial for the task at hand [99].

4.4 Gait Metric Resolution

An important characteristic of a gait metric is the scale at which it operates. For example, the step length metric defined in Section 4.2 requires data from

[18]Note that each foot has a distinct heel strike event. If a gait cycle begins at right heel strike, then it ends at (or just before) the next right heel strike, and includes the intervening left heel strike.

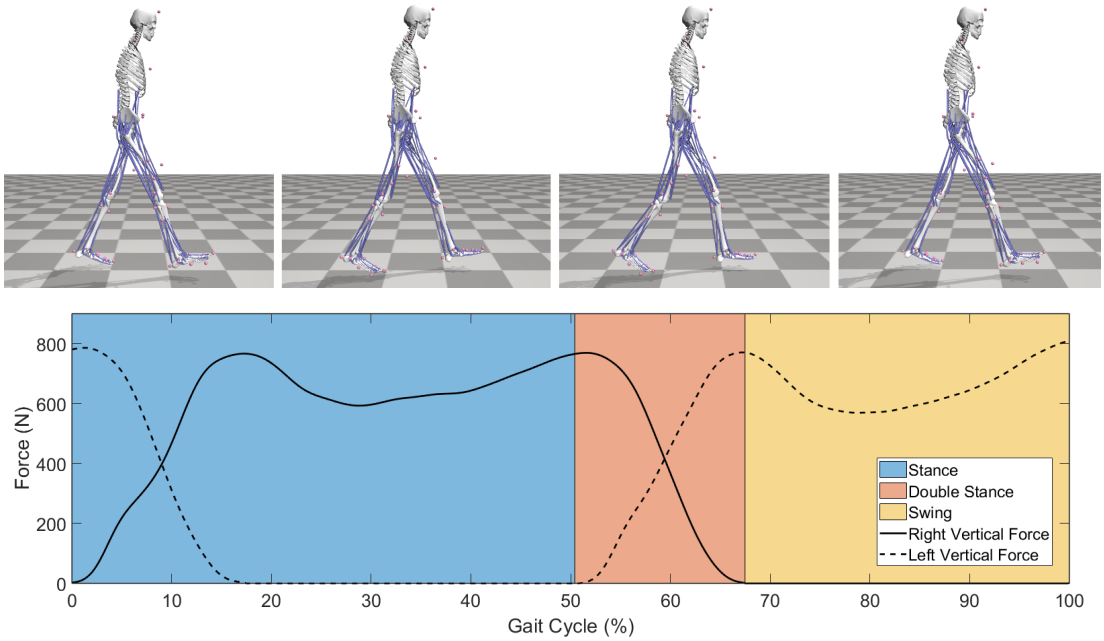

Figure 4.1: **Top:** snapshots from a motion reconstruction of a gait cycle. From left to right, the pictured events are: right heel strike, left heel strike, right toe off, and finally (just before) the closing right heel strike. Other events (e.g. maximal hip flexion) occur between these key points [96]. **Bottom:** the vertical component of the ground reaction force vector corresponding to the above motion sequence. The shaded areas on the graph partition the stance, double stance and swing phases. Note that during the swing phase the left foot is in stance, but conventionally the phases are described according to the leading foot.

a full gait cycle in its calculation. Other metrics are defined on subsets of the gait cycle — for example, those involving trajectories of the centre of pressure can only be computed during stance phase, when contact is made with the ground. On the other hand, gait metrics which have been developed to score gait relative to the normal of a population [88, 89] may require many gait cycles, both from the subject in question and a database of healthy gait data.

Moving forward, we will adopt the term *resolution* to describe this behaviour. Metrics which are defined at individual timesteps or subsets of a gait cycle can be described as *high resolution*, while those requiring multiple gait cycles of data to compute are *low resolution*.

Resolution is an important property which, depending upon the context

in which it is used, in some ways determines the usefulness of a given gait metric. For example, for purposes of comparing against the normal of a population, low resolution gait metrics requiring many gait cycles are likely ideal. A concrete example of this is Gait Profile Score [89], which compares mean kinematic variables over large amount of gait data. On the other hand, for our purposes (i.e. use as part of a real-time exoskeleton control scheme), high resolution gait metrics which can be calculated at a fast rate on small timesteps are clearly preferred.

4.5 Gait Metric Invariance

Current control paradigms frequently use normalised kinematic trajectories [100], muscle amplification [15], or finite state controllers [101]. The respective issues with these paradigms are that the kinematic trajectory might not be appropriate for the user's task or their environment, the muscle firing patterns may be abnormal, and there are a large number of parameters to tune.

The human neuromuscular system optimises for gait stability [14]. By studying the effect of different walking contexts and constant perturbations (applied via an exoskeleton) on healthy walking, it is posited that there will be an underlying invariant metric that reflects the optimisation of the stability of human gait. Once identified, this metric can then be optimised as part of an exoskeleton control paradigm which provides assistance while maintaining balance, implicitly accounting for the effects of changing walking context and varying exoskeleton assistance. Previous work has been carried out to determine what effect walking speed [102–104], the environment [105, 106], and exoskeleton forces have [107–109] on a user's gait, but these are constrained by using limited metrics and, for the work done on exoskeletons, limited walking contexts.

In this section, we analyse the invariance properties of exoskeleton-assisted locomotion over a variety of walking conditions. Three walking scenarios are tested: walking without an exoskeleton, walking with an exoskeleton in transparent mode, and walking with an exoskeleton in assistive mode. For each of these scenarios five different walking contexts were investigated: walking at baseline speed, walking up an incline, walking down an incline, fast walking,

and slow walking. A number of gait metrics were compared to identify those which demonstrated the most invariance and therefore would be suitable for optimising in an exoskeleton control paradigm.

4.5.1 Candidate Stability Metrics

The set of gait metrics were chosen so as to cover a range of spatial, temporal and derived metrics. The metrics and corresponding definitions were as follows:

- Step width was determined as the medial-lateral distance between the lateral malleolus markers at the heel strikes of consecutive steps.
- Step frequency was calculated as the inverse of the time between the heel strikes of consecutive steps.
- The hip range of motion ($\theta_{\text{hip-RoM}}$) was calculated by subtracting the maximum hip flexion joint angle from the minimum over the gait cycle.
- Hip peak to peak torques ($\tau_{\text{hip-pp}}$) were calculated by subtracting the maximum hip flexion joint torque from the minimum over the gait cycle.
- The centre-of-mass (CoM) displacement was calculated by subtracting the maximum CoM position from the minimum over the gait cycle. This was calculated in both the vertical and medial-lateral directions, resulting in two distinct metrics: CoM-V_{disp} and CoM-ML_{disp}, respectively.
- The centre-of-pressure (CoP) displacement was calculated by subtracting the maximum CoP position from the minimum over the stance phase. This was calculated in both the anterior-posterior and medial-lateral directions, resulting in two distinct metrics: CoP-AP_{disp} and CoP-ML_{disp}, respectively.
- The margin of stability was calculated as specified by Hof [110]:

$$MoS = \left| u_{max} - (x + \frac{v}{\omega_0}) \right|, \tag{4.3}$$

where u_{max} is the boundary of the base of support, x is the centre of mass position, v is the centre of mass velocity, and ω_0 is equal to:

$$\omega_0 = \sqrt{\frac{g}{l}}, \tag{4.4}$$

with g denoting acceleration due to gravity and l being the distance from the pelvis ASIS to the lateral malleolus. The MoS was calculated in both the anterior-posterior (MoS-AP) and medial-lateral (MoS-ML) directions, resulting in two distinct metrics.

These metrics are summarised for reference in Table 4.1, which provides the names, unit and notation for each metric.

4.5.2 Experimental Protocol

Subjects were invited to the Gait Lab at The University of Edinburgh where they walked under a variety of conditions. The APO was used to provide assistance, while the Vicon system and instrumented treadmill were used to record marker trajectories and ground reaction forces, respectively. Full details of the equipment including the raw data processing procedure for all data streams is provided in Chapter 2.

To capture data in different walking contexts, a script was implemented in

Metric	Direction	Notation	Unit
Step width	-	-	cm
Step frequency	-	-	steps/min
Sagittal hip angles RoM	-	$\theta_{\text{hip-RoM}}$	degrees
Sagittal peak to peak hip torques	-	$\tau_{\text{hip-pp}}$	Nm/kg
CoM displacement	Vertical	CoM-V_{disp}	mm
CoM displacement	Medial-lateral	CoM-ML_{disp}	mm
CoP displacement	Medial-lateral	CoP-ML_{disp}	mm
CoP displacement	Anterior-posterior	CoP-AP_{disp}	mm
Margin of stability	Medial-lateral	MoS-ML	mm
Margin of stability	Anterior-posterior	MoS-AP	mm

Table 4.1: The dimensions, notations, and units of the tested gait metrics.

the Motek D-Flow software to programmatically change the speed or incline of the treadmill appropriately. Each subject was made to walk in five different walking contexts, as follows: at baseline walking speed with no incline (BW), at baseline walking speed with an incline of 5 degrees (UW), at baseline walking speed with an incline of -5 degrees (DW), at a fast walking speed with no incline (FW), and at a slow walking speed with no incline (SW). The baseline walking speed used for the BW context was calculated using the principle of dynamic similarity as described by the Froude number [111]:

$$v = \sqrt{F_r g L}, \tag{4.5}$$

where v is the baseline speed, F_r is the Froude number (chosen to be 0.1), g is gravitational acceleration (9.81m/s^2), and L is leg length (as measured from the greater trochanter to the medial malleolus). The speeds for FW and SW were calculated by adding and subtracting 20% to the baseline speed respectively. Each context was timed to last 135 seconds, with data collection triggered to happen after 120 seconds to allow for the participant to become accustomed to the context.

The contexts were repeated for 3 different assistance scenarios: one without wearing the APO (NE), one wearing the APO set in transparent mode (ET) and one wearing the APO set in assistive mode (EA) with the virtual stiffness set to 15 Nm/rad. For each subject, a static pose was collected in both the NE and ET assistance scenarios.

4.5.3 Modelling Approach

The processed data for each subject was divided in to 10 gait cycles per combination of walking context and assistance scenario. A range of analyses were then carried out using OpenSim tools in combination with the gait2392 and human-APO musculoskeletal models[19].

The first step was to scale (Appendix A.1) the generic versions of these models using the static pose data. The gait2392 model was scaled using static pose data from the NE assistance scenario, while the human/APO model was

[19]Full details of these models are provided in Chapter 3.

scaled using data from the ET assistance scenario. After scaling, the following sequence of analyses was carried out for each gait cycle:

- The **Inverse Kinematics Tool** (Appendix A.2) was used to calculate joint angles given the marker trajectories.
- The **RRA Tool** (Appendix A.3) was used to produce dynamically consistent joint angles and a corrected model file from joint angles and ground reaction forces.
- The **Inverse Dynamics Tool** (Appendix A.5) was used to calculate joint torques given the RRA-corrected joint angles and ground reaction forces.
- The **Analysis Tool** was used to solve for the position and velocity of the model centre of mass given the RRA-corrected kinematics.

The outputs of these analyses were used in the calculation of the stability metrics. A schematic of the overall data processing and analysis pipeline is provided in Figure 4.2.

4.5.4 Statistical Analysis

The mean and standard deviation of each stability metric was averaged over all recorded gait cycles and all subjects, for each combination of walking context and assistance scenario. Therefore, the number of samples for each combination of stability metric, walking context and assistance scenario was 70 for most metrics (10 gait cycles $\times$ 7 subjects[20]). An exception was the step-width metric, which relies on pairs of adjacent gait cycles for its computation, and therefore had a sample size of 63 (9 pairs of adjacent gait cycles $\times$ 7 subjects).

To investigate the effects of the exoskeleton assistance and the walking context on the stability metrics, a two-way ANOVA was used. For the post-hoc analysis, the MATLAB multiple comparison procedure 'multcompare' was used with the comparison type based on Tukey's honestly significant difference criterion. The statistical significance level was set at $\alpha = 0.05$.

[20]The data from one subject had to be discarded due to an issue with the force plate calibration.

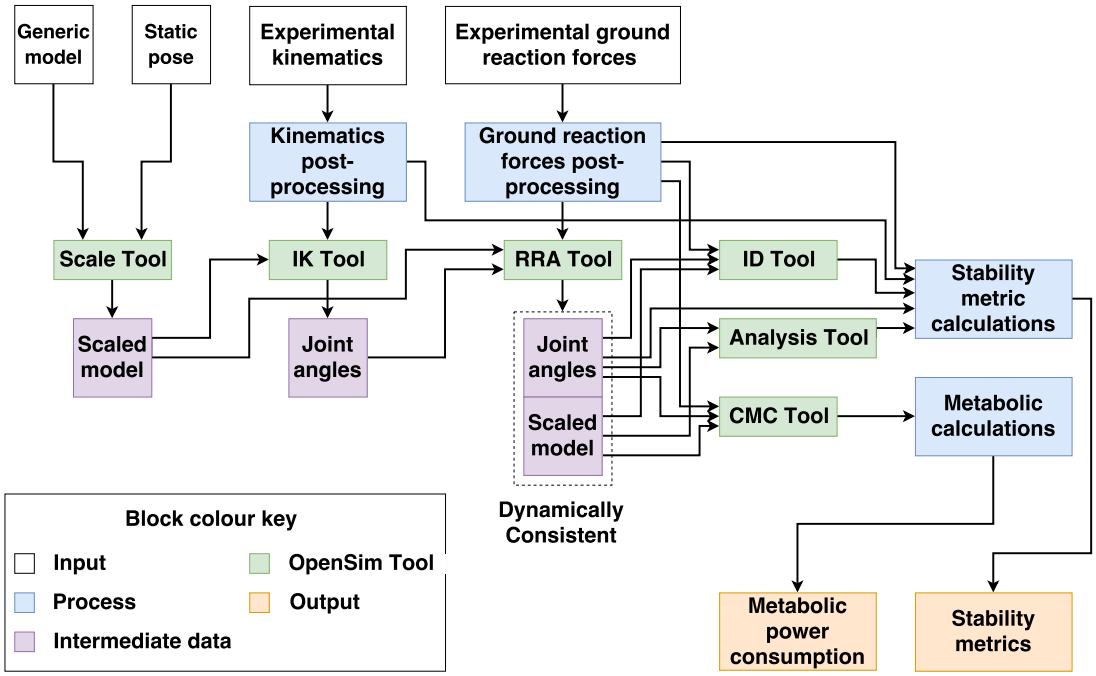

Figure 4.2: A schematic demonstrating the data collection and analysis pipeline.

For combinations of walking context and assistance scenario which demonstrated a significant difference in the mean of a metric, the effect size was measured by computing the absolute value[21] of Cohen's d. These values were then averaged to produce a quantitative measure of invariance for each metric relative to changes in assistance level, changes in walking context, and overall. Qualitative analysis of the effect size of each metric was undertaken according to typical cut-offs for the value of Cohen's d [112, 113], which are provided for reference in Table 4.2.

Effect size	Cohen's d range
Very small	$0.01 \leq d < 0.20$
Small	$0.20 \leq d < 0.50$
Medium	$0.50 \leq d < 0.80$
Large	$0.80 \leq d < 1.20$
Very large	$1.20 \leq d < 2.00$
Huge	$d \geq 2.0$

Table 4.2: A mapping from qualitative descriptions of effect size to the corresponding range of Cohen's d.

[21] The decision to take the absolute value was motivated by an interest in the magnitude of an effect rather than it's direction.

Subject	Height (m)	Weight (kg)	Walking velocity (m/s)		
			BW	FW	SW
S1	1.84	76.4	0.95	1.14	0.76
S2	1.79	67.1	0.95	1.14	0.76
S3	1.74	58.8	0.94	1.13	0.75
S4	1.76	77.2	0.94	1.13	0.75
S5	1.88	83.0	0.97	1.18	0.78
S6	1.80	61.4	0.96	1.15	0.77
S7	1.77	66.6	0.97	1.16	0.78
S8	1.80	75.8	0.95	1.14	0.76

Table 4.3: The subjects' anthropometric features and walking velocities. ©IEEE 2017

4.5.5 Results

The anthropometric measurements and calculated walking velocities for each subject are presented in Table 4.3.

Running the RRA tool for all the data sets generated residual forces and moments FX, FY, FZ, MX, MY, and MZ. These residual forces and moments are applied to the pelvis in simulation to account for the dynamic inconsistency between the dynamic model and the recorded data. These residuals should be low to ensure accurate simulations. All of the average residual forces measured during our simulations were less than the thresholds specified by the OpenSim developers (see Table 4.4).

For each combination of metric, context, and assistance scenario the percentage difference from the baseline condition (no exoskeleton assistance and walking at baseline speed) is demonstrated in Figures 4.3 - 4.4. The mean and

Quantity	Value	OpenSim Benchmark
RMS Residual force (N)	7.1 ± 3.4	< 10
Peak Residual force (N)	17.9 ± 7.6	< 25
RMS Residual moment (N)	7.3 ± 4.0	< 50
Peak Residual moment (N)	16.9 ± 8.7	< 75

Table 4.4: RRA residuals in OpenSim. ©IEEE 2017

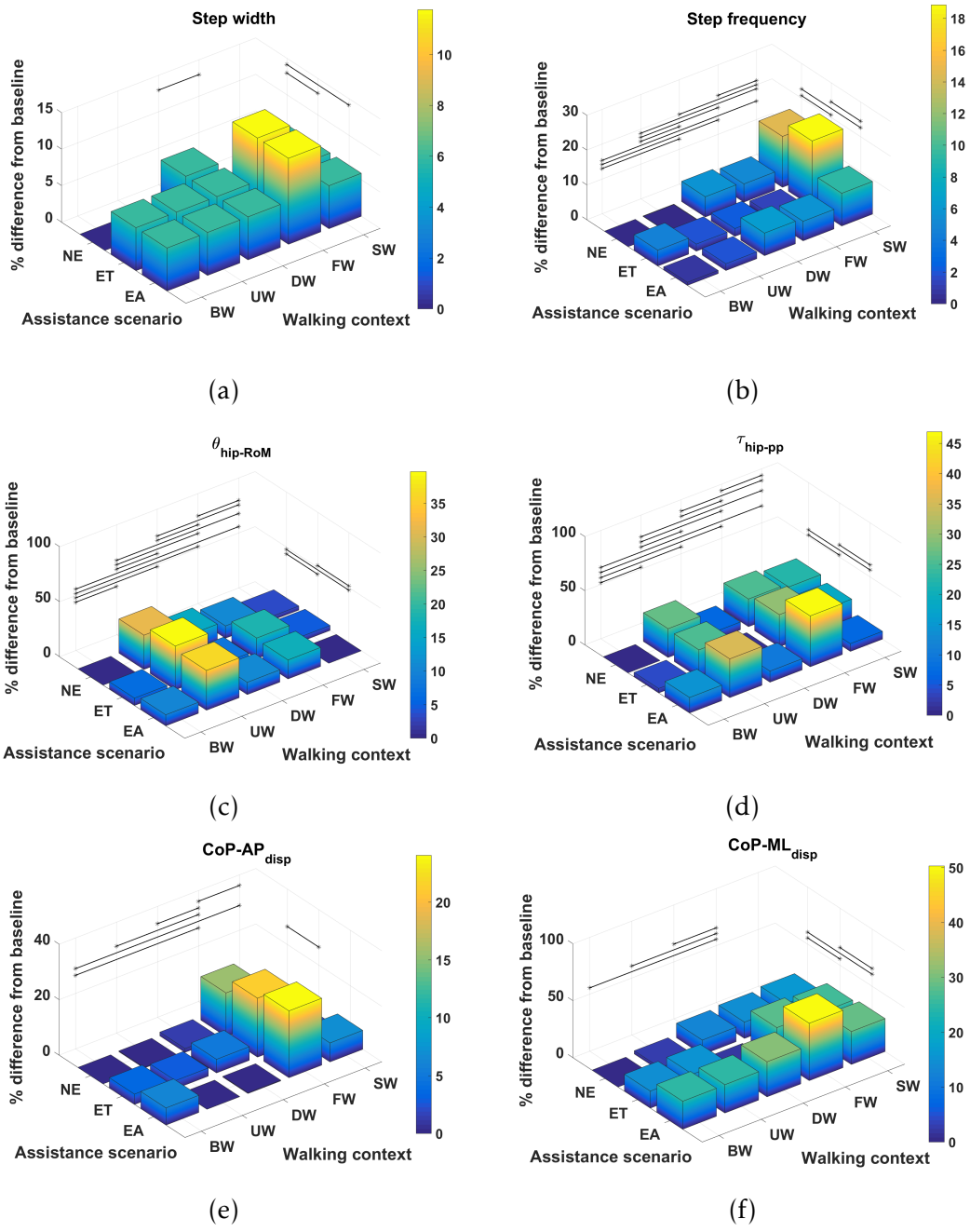

Figure 4.3: Percentage difference from baseline, categorised by walking context and assistance scenario, for (a) Step width, (b) step frequency, (c) $\theta_{\text{hip-RoM}}$, (d) $\tau_{\text{hip-pp}}$, (e) CoP-AP$_{\text{disp}}$ and (f) CoP-ML$_{\text{disp}}$. Black lines represent significant differences. ©IEEE 2017

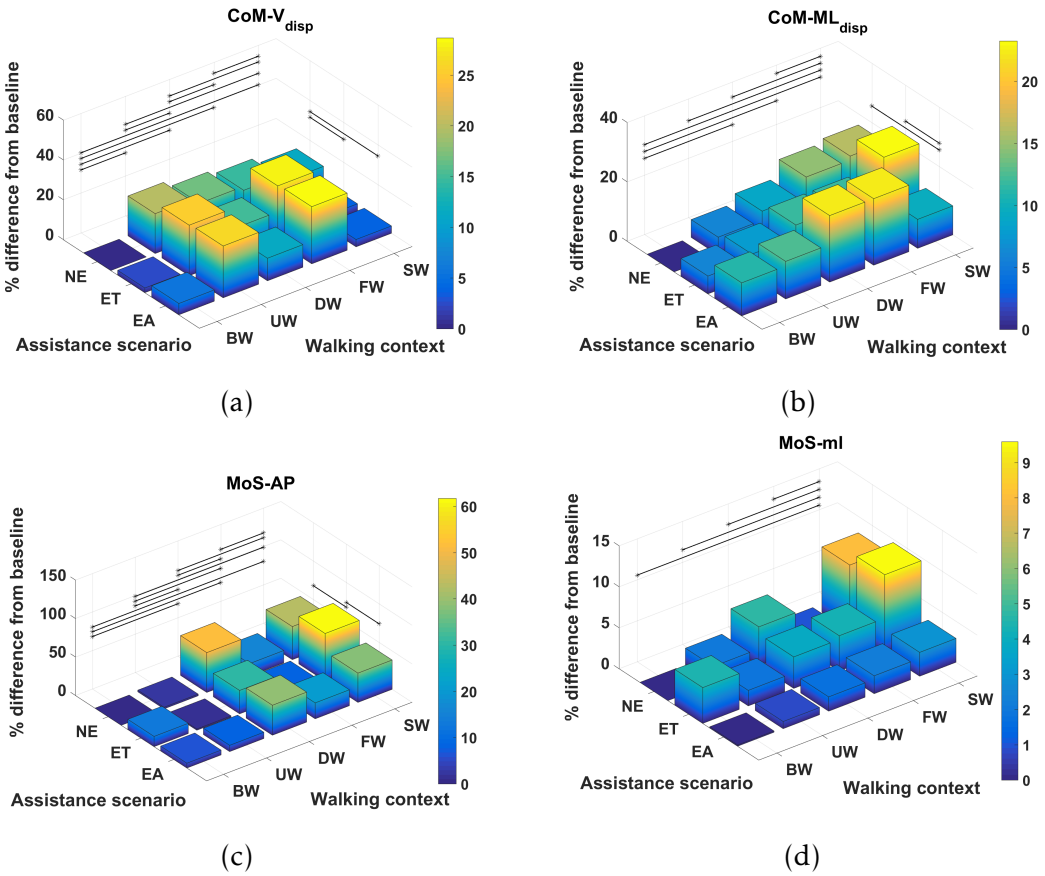

Figure 4.4: Percentage difference from baseline, categorised by walking context and assistance scenario, for (a) CoM-V_{disp}, (b) CoM-ML_{disp}, (c) MoS-AP and (d) MoS-ML. Black lines represent significant differences. ©IEEE 2017

standard deviation values for every context and assistance scenario combination are detailed in Appendix B.1.

The effect sizes for each metric, averaged separately by walking context and by assistance scenario, are displayed in Figure 4.5. Comparing the effect sizes averaged over walking contexts, we see that step width, CoP-ML_{disp}, and MoS-ML have the lowest average effect size. These metrics demonstrate Cohen's d values that indicate between small and medium effect sizes. The $\theta_{\text{hip-RoM}}$ metric exhibits a Cohen's d of $d > 2.0$, which implies a huge effect size. All of the other metrics show effect sizes of large or very large. This analysis implies that, relative to changes in walking context, the step width, CoP-ML_{disp}, and MoS-ML metrics demonstrate the highest level of invariance.

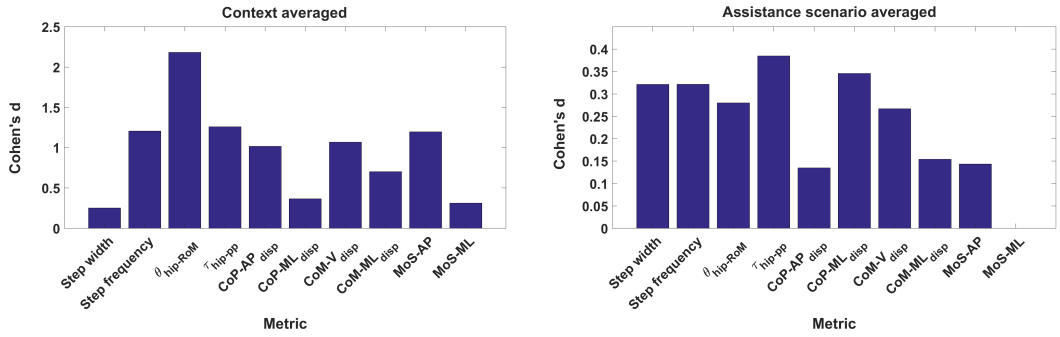

(a) (b)

Figure 4.5: The effect sizes averaged over (a) context and (b) assistance.

Comparing the effect sizes averaged over assistance scenario, the metrics which exhibit the lowest average effect size are CoP-AP_{disp}, CoM-ML_{disp} and, similarly to the context results, MoS-ML. These metrics exhibit a Cohen's d of $d < 0.2$, which indicates a very small effect size. All other metrics exhibit a small effect size. Compared to the results for walking context, the effect of changing assistance scenario is in general less than for changing walking context. This analysis implies that the CoP-AP_{disp}, CoM-ML_{disp} and MoS-ML metrics demonstrate the highest level of invariance relative to changes in the assistance scenario.

In Figure 4.6, the effect size is shown for each metric, averaged over both walking context and assistance level simultaneously. From these results, we see that step width, CoP-ML_{disp} and MoS-ML are the metrics which exhibit the lowest effect size, with values of Cohen's d between 0.2 and 0.5 corresponding to a medium effect. Analysing the remaining metrics, we see that the CoM-ML_{disp} metric exhibits a medium effect size, the $\theta_{\text{hip-RoM}}$ metric exhibits a very large effect size, and all remaining metrics exhibit large effect sizes. From this analysis we conclude that overall, taking in to account both changes in walking context and assistance scenario, the three metrics which exhibit the most invariance are step width, CoP-ML_{disp} and MoS-ML.

4.5.6 Discussion

It is well known that walking speed is a cause of gait variability for kinematic, kinetic, and CoM_{disp} metrics [102–104] and the results from this study also

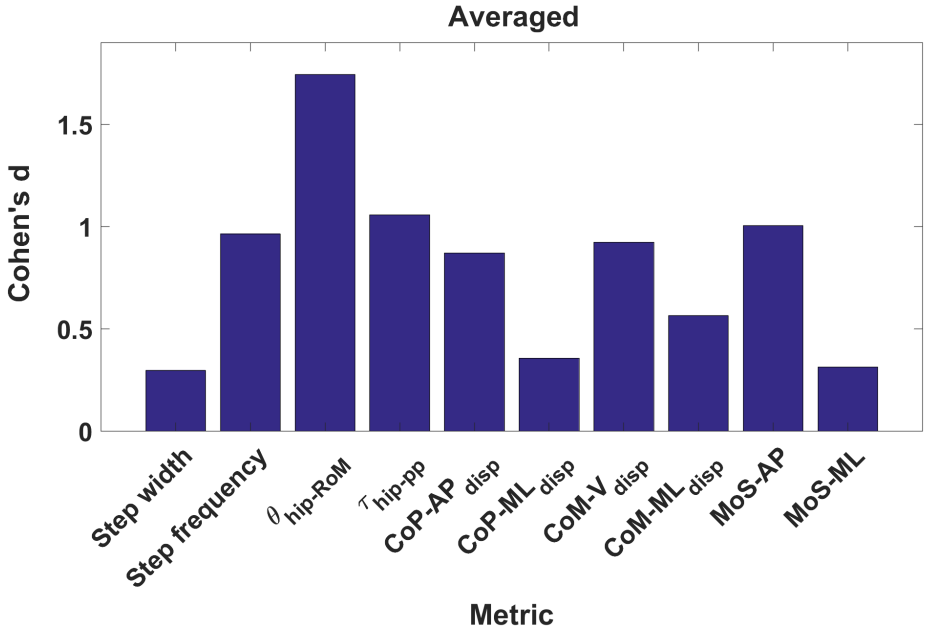

Figure 4.6: The effect sizes averaged over all combinations of walking context and assistance scenarios.

demonstrate the same findings. This study demonstrates that step frequency increases due to speed and anecdotally suggests that step length increases as well (step length was not included in the analysis due to unavailability of complete consecutive step data for some of the participants due to cross-talk on the force plates). The step width was demonstrated to be invariant with only one significant difference with a small effect size between walking downhill and walking at a fast speed. Walking speed causes variation for the CoP-AP_{disp} and the CoP-ML_{disp} metrics, however, the effect on the CoP-ML_{disp} metric is small and only significant between the fast and baseline walking speed contexts. Walking speed affects the MoS-AP and MoS-ML metrics, however there is only a small effect in the medial lateral direction between the slow and baseline walking speed contexts. It is a logical result that walking speed has a greater effect on the metrics measured in the anterior posterior direction compared to the medial lateral direction because walking speed is a change of direction mainly in the anterior posterior direction.

The effect of walking up and down an incline has previously been demonstrated to have significant kinematic and kinetic changes [105] and the find-

ings from this study support this result. In additional to the effects on kinematics and kinetics the results from this study indicate that walking on an incline affects the CoM-V_{disp} metric and that walking down an incline affects the step frequency, CoM-V_{disp}, CoM-ML_{disp}, and MoS-AP metrics. The increase in step frequency is expected due to a shorter step length being taken. The effects on the CoM vertical displacement are also expected due to the change in height caused by the slope. The effect on the MoS-AP metric is expected because it is clear that when the torso is tilted forwards, the projection of the centre-of-mass becomes located further from the centre of the base of support, and thus the MoS-AP metric should increase. Neither walking up or down an incline had any effect on the MoS-ML metric.

This study demonstrates there are significant differences in the $\theta_{\text{hip-RoM}}$ metric caused by context and assistance scenario changes. This result aligns with the work by d'Elia et al. [114], and similarly their claim that the differences in the $\theta_{\text{hip-RoM}}$ metric between the ET and EA assistance scenarios lie within the natural variation of gait is also applicable. There was a significant increase in the $\tau_{\text{hip-pp}}$ metric from the ET to the EA scenario. This result suggests a disagreement with a study by Lewis and Ferris [109], which found that the net torques did not change between walking with an exoskeleton in passive mode and with it in assistive mode. The result from our study suggests that torque from the exoskeleton is not entirely being transferred to the individual, which is quite probable due to the non-rigid attachments of the exoskeleton. There is a significant increase in the CoP-ML_{disp} metric from the NE and the ET and EA scenarios, which can be attributed to the extra weight of the exoskeleton laterally located to the participant. One consideration for the above findings is that the effect sizes for all the metrics for the assistance scenarios were between small and medium, which suggests the differences are small between the assistance scenarios. This is in contrast to the context effect sizes, where 6 out of the 10 metrics had large or greater effect sizes.

Overall, our results quantify the effect that varying walking context has on the effectiveness of active exoskeleton assistance. All tested metrics demonstrated some significant differences due to the changes in walking context and assistance scenario. After factoring in the effect sizes the most invariant metrics were shown to be the step width, CoP-ML_{disp}, and MoS-ML met-

Resolution Considerations

Using the terminology from Section 4.4, the CoP-ML_{disp} and MoS-ML metrics are more suitable for use in a control paradigm because they are high resolution — they can be calculated at any given time during the stance phase of a gait cycle and therefore enable a significantly more responsive controller than the step width metric, which is comparatively low resolution.

rics. All three metrics have been demonstrated to be associated with stability [14], [110], [115], and therefore it is intuitive that they remain fairly constant despite changes in walking context and the application of constant perturbations. As a source of further work, our investigation of stability metrics could be repeated with patients, to determine how the invariance properties of the metrics are affected by gait pathologies. Additionally, A limiting factor of our study is that the adaptive oscillator control scheme was the only exoskeleton controller tested. A further source of further work could be to apply or develop additional control paradigms, so that their relative performance over different contexts can be analysed.

Formulation Update

In this chapter we have seen that kinematic trajectories are particularly susceptible to changes in walking context — therefore, kinematic error minimisation alone is unlikely to be a useful optimisation goal for assistive exoskeletons. Instead, for a metric set $\mathcal{M} = \{m_1, m_2, \ldots, m_k\}$, where $m_i : \mathcal{X}^n \to \mathbb{R}$ for $1 \leq i \leq k$ is a *gait metric* as defined in Definition 4.4, with a corresponding weight set $W = \{w_1, w_2, \ldots, w_k\}$, a more suitable objective function might be:

$$
\begin{aligned}
\min_{\boldsymbol{\mu}_e} \sum_{1}^{k} w_i m_i \,, \\
M_c(\mathbf{q})\ddot{\mathbf{q}} + \mathbf{c}_c(\mathbf{q}, \dot{\mathbf{q}}) + \mathbf{g}_c(\mathbf{q}) &= \boldsymbol{\tau}_h + \boldsymbol{\tau}_g + \boldsymbol{\tau}_e \,, \\
\boldsymbol{\tau}_e &= \mathbf{E}(\boldsymbol{\mu}) \,, \\
\boldsymbol{\tau}_h &= \mathbf{F}\left(\mathbf{f_0}, \mathbf{l}, \dot{\mathbf{l}}\right)^{\mathsf{T}} R(\mathbf{q})\mathbf{a} \,, \\
\dot{\boldsymbol{l}} &= \mathbf{C}(\mathbf{a}, \mathbf{l}, \mathbf{q}, \dot{\mathbf{q}}) \,, \\
\dot{\boldsymbol{a}} &= \mathbf{A}(\mathbf{a}, \boldsymbol{\nu}) \,, \\
\boldsymbol{\mu} &\leq \boldsymbol{\mu}_{\max} \,, \\
\boldsymbol{\nu}_{\min} \leq \boldsymbol{\nu} &\leq \boldsymbol{\nu}_{\max} \,.
\end{aligned}
$$

For assistive exoskeletons, we are motivated make use of those gait metrics which are low resolution with high levels of invariance to changes in walking context. Therefore, we select $\mathcal{M}_A = \{\text{MoS-ML}, \text{CoP-ML}_{\text{disp}}\}$, including contributions from margin of stability and centre of pressure, respectively, which were identified in this chapter to have those properties.

Note however that human locomotion is complex and often humans walk with different goals in mind - for example, a casual walk is very different to a rushed one (both in appearance and in terms of energetics). In general, the metric set $\mathcal{M}$ should contain terms which are weighted appropriately according to the task at hand. For instance, certain exoskeletons may indeed benefit from kinematic trajectories in the objective function to accurately track rehabilitation programmes, and thus may adopt a different weight set $\mathcal{M}_R$.

Chapter 5

Human-in-the-loop Optimisation

Human gait is unique and complex [116], and predicting adaptations in unassisted gait is challenging [117]. It is unsurprising then that the added complexity of shared control, which invariably means that human neuromuscular patterns are affected by external interaction forces [20], creates additional challenges. For exoskeletons and prosthetics to reach their full potential, methods must be developed which deal with this problem.

In this chapter, we will first outline one such method known as human-in-the-loop optimisation. Then, we discuss an application of the human-in-the-loop optimisation framework applied to an offline example of exoskeleton design optimisation. In Chapter 6, we will see an online application of the framework which deals with the optimisation of assistive control patterns.

Offline vs. Online Human-in-the-loop Optimisation

The terms *offline* and *online* in this chapter refer to the nature of the data acquisition process in the human-in-the-loop optimisation protocol. The example presented in this chapter uses a pre-collected dataset as a surrogate for the 'human-in-the-loop', i.e the data collection occurs *offline*. In the next chapter, however, the data input to the optimisation is collected directly from a human subject during runtime, i.e data acquisition occurs *online*.

5.1 The Human-in-the-loop Optimisation Framework

Human-in-the-loop (HIL) optimisation is a technique which seeks to optimise some aspect of an assistive device by iteratively taking measurements from the intended wearer 'in the loop', evaluating device performance according to some metric, and updating the system according to an underlying optimisation algorithm. Ultimately, the aim of this process is to produce a tailored assistance solution for each individual. A diagram outlining the generic structure of a HIL protocol is provided in Figure 5.1.

Typically, HIL optimisation is used to optimise a parameterised control law [17, 99, 118], though other objectives have included step frequency [59, 119] and parameterised design variables [120]. Most commonly, device performance is evaluated by quantifying metabolic rate via respiratory gas analysis [17, 59, 99, 118, 119], however other physiological signals such as EMG activity [120, 121] or subject feedback [122] have successfully been used as a performance criterion. A number of approaches have been tested for the optimisation step, ranging from linear exploration polynomial fitting methods [119] to evolutionary search strategies [17]. In the next section, we will detail a specific method which has achieved particularly strong results.

5.2 Bayesian Optimisation

Bayesian optimisation is a method of identifying the minimum of a function $f : X \to \mathbb{R}$, for some bounded set X, where samples from f can be readily obtained. To do so, a model for f is created using Gaussian processes, and

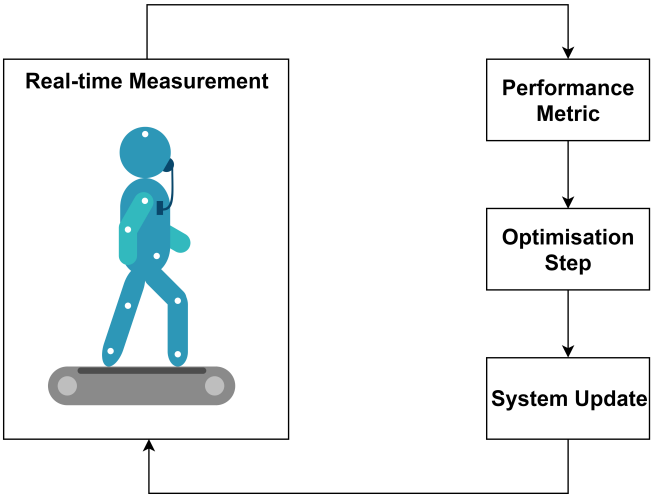

Figure 5.1: A schematic illustrating the key steps comprising a generic implementation of HIL optimisation. To illustrate, a specific implementation [99] could use calorimetry (the real-time measurement) to quantify metabolic cost (the performance metric) while using Bayesian optimisation (the optimisation step) to update some parameterised control law (the system update).

updated with the data from successive samples. The appropriate points in the domain at which to sample from are determined through the optimisation of an acquisition function, which determines the most valuable point according to some criterion [123].

Consider an objective function f with parameters $\mathbf{x}$, where we do not know the analytical form of f but are free to sample from it. Bayesian Optimisation is a process which ultimately seeks to minimise (or maximise) f by repeatedly drawing samples and updating a posterior expectation of f. Bayesian Optimisation assumes that the function f can be described by a Gaussian process [123]. The sample points are chosen in such a way that an *acquisition function* is maximised, which in some sense defines which regions of f are 'most useful' to sample from i.e. provide the highest utility. The Bayesian Optimisation algorithm proceeds as follows:

1. Given known values $\mathbf{y} = \{f(\mathbf{x}_1), f(\mathbf{x}_2), ...\}$, update the posterior expectation of f using Gaussian Processes.

2. From the posterior expectation of f, find the argmax of the acquisition function to determine x_{new}, the next point to sample from.

3. Compute $f(\mathbf{x}_{\text{new}})$ and add it to the list of known values.

Steps 1 - 3 are repeated for a set number of iterations or until some termination criterion is satisfied. The algorithm is typically initialised by sampling from a fixed number of randomly generated points.

There are a number of properties of Bayesian optimisation which make it well suited for use as a HIL optimiser. In particular, it works well even in the presence of noisy data signals, and requires comparatively few iterations to reach an approximate solution [99]. Both of these points are important: human motion data is typically noisy[22], and working with human subjects places a practical limitation on the amount of data that can be collected due to fatigue.

5.3 Personalisation of Exoskeleton Design

Exoskeletons which fit poorly can cause discomfort and even work against the intended aim of the device [79, 82], altering natural muscle activation patterns in undesired ways [81]. As such, the optimal scenario is for exoskeletons to be designed with a particular subject in mind. However, it is not always possible for individuals to obtain these devices on an ad hoc basis. This is especially true in low to middle income countries, where creating personal devices on an individual basis is not feasible due to complexity of the manufacturing process and excessively high cost [124].

Several strategies are being investigated to deal with this problem. One is the creation of modular exoskeleton designs which can be manufactured cheaply and efficiently, in some cases using 3D printable parts [125, 126]. A doctor or physiotherapist could request a specific design and have it cheaply manufactured for patients. Another strategy is to include passive degrees of freedom in exoskeleton designs. The inclusion of passive DOFs can in some sense be used to minimise the kinematic inconsistency between exoskeletons and human subjects [77]. Finally, an additional strategy is to develop exoskeletons which are in some way adjustable, so that they can be easily modified to suit he needs of a particular subject. One example of such a robot is the

[22] Some biomechanical data streams are more noisy than others: motion capture data can be fairly low noise, but calorimetry measurements are notoriously noisy (see Chapter 2).

XoR, developed at ATR in Japan, a lower-body exoskeleton which features 4 adjustable cuffs located on the thigh and shank link segments [67]. Robots such as these could in theory be adjusted on the fly according to the needs of an individual, and would suit being used in rehabilitation centres where many patients require treatment.

One difficulty with the use of such exoskeletons is how to decide which cuff positions are optimal for a specific patient and use case. For example, the ideal cuff positions could differ between healthy people due to different limb lengths, heights, muscle masses and other physical characteristics. Studies have shown that the power loss between the torques generated by an exoskeleton and those experienced by a human subject are significant [82, 83]. These losses are due in part to interface dynamics involving soft biological tissues, and could in theory be mitigated by a suitable selection of the interface position. Additionally, optimal cuff positions could differ between patients with different disabilities or afflictions - whether the aim is to target the hamstrings or gastrocnemius muscles, for example. If adjustable exoskeletons are to be used effectively in a clinical setting, a means of efficiently identifying the optimal cuff positions for an individual is required. A linear search for the optimal exoskeleton configuration is likely to be too time-expensive to perform, especially as the number of design parameters increases.

In this work, we propose the use of Bayesian optimisation as a method to efficiently identify the optimal cuff configuration for an individual. A human-in-the-loop optimisation process was designed and carried out using measurement data obtained from a subject walking with the XoR exoskeleton. An empirical validation of our method is presented, based on recorded EMG data.

Several recent works have begun to explore using optimisation to improve exoskeletons. Hamaya et al. (2017) used a reinforcement learning framework to learn the assistive strategy of a 1-DoF exoskeleton robot which best reduced human EMG measurements [121]. Zhang et al. (2017) and Ding et al. (2018) used a human-in-the-loop optimisation process to improve the torques applied by exoskeletons in terms of metabolic energy reduction [17, 99]. Kim et al. (2017) used Bayesian optimisation to optimize step frequency in unaided human subjects [59]. Our contribution differs from these works in that Bayesian optimisation is used with the intent of optimising exoskeleton design

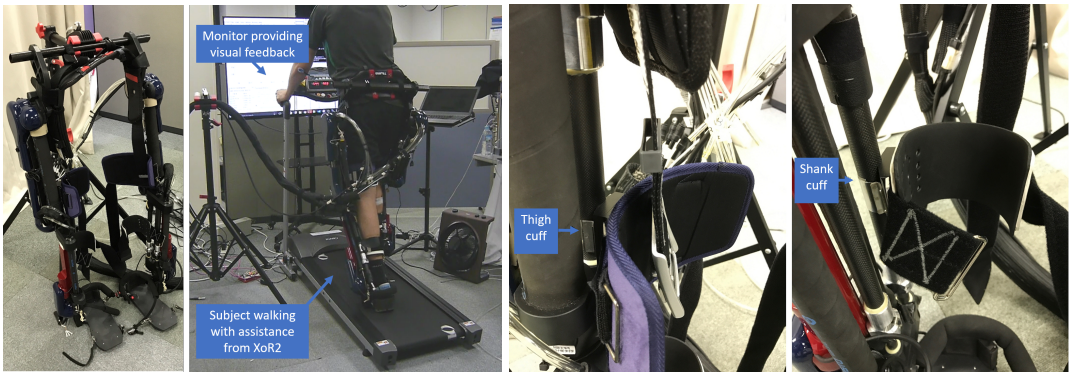

Figure 5.2: **Left:** the XoR exoskeleton. **Centre-left:** a snapshot during a data capture. A subject is wearing the XoR while walking on a treadmill, with a monitor providing visual feedback so the subject can attempt to track the reference trajectory. **Centre-right/right:** a close-up view of the thigh and shank cuffs. The cuffs are adjustable vertically on the bar to which they are connected.

parameters.

5.3.1 Hardware

The exoskeleton which we used to apply assistance is the lower-body exoskeleton XoR, introduced in Chapter 2 but shown for reference in Figure 5.2. The XoR features 4 adjustable cuffs which attach to the left/right thigh and shank of the user, providing a structural link between the human and robotic systems. Therefore, the system has four design parameters: x_L, x_R, y_L and y_R, where x and y denote the thigh and shank cuffs and L and R distinguish between the left and right leg, respectively. The 'usable' lengths of the thigh and shank links (meaning the length on which the cuffs could be attached) were measured at 10.3cm and 12.0cm, respectively. The properties of the XoR's design parameters are summarised in Table 5.1.

The assistance provided by the XoR was governed by a PD controller implemented for this experiment. The controller tracked reference kinematic trajectories for the hip, knee and ankle joints, measured while the subject walked with the XoR in passive mode. While walking, the subject was provided with visual feedback via a screen to aid with alignment to the reference trajectories. The PAM actuators were disabled throughout all walking trials, meaning all

joints were actuated only by the DC motors.

5.3.2 Experimental Design

Two sets of walking trials were undertaken for a single subject wearing the XoR. Each individual trial consisted of 60s of walking at a steady pace on a treadmill. This 60s period was structured as follows:

1. 10s for initial adjustment and alignment with reference trajectories,
2. 20s of recorded unassisted walking,
3. Engaging assistance, followed by a 10s period for adjustment,
4. 20s of recorded assisted walking.

In Trial Set 1, the position of the shank cuffs was kept fixed while the thigh cuff position was varied from 0.5cm to 10.0cm in steps of 0.5cm. In Trial Set 2 the thigh cuffs were kept fixed while the shank cuff position was varied from 0.5cm to 11.5cm in steps of 1.0cm[23]. In both trial sets, the left and right cuff positions were coupled, i.e. $x_R = x_L$ and $y_R = y_L$. Measurements of the cuff locations were made using a tape measure. An example of a walking trial in progress is displayed in Figure 5.2.

5.3.3 Data Processing

Measurements recorded while the subject walked included the encoder readings and motor currents from each active joint of the XoR, as well as EMG

[23]The discrepancy in step sizes was due to the process of changing the shank cuff position being more time consuming and intricate than that of the thigh cuff.

Design parameter	Notation	Domain (cm)
Right thigh cuff position	x_R	$[0, 10.3]$
Left thigh cuff position	x_L	$[0, 10.3]$
Right shank cuff position	y_R	$[0, 12.0]$
Left shank cuff position	y_L	$[0, 12.0]$

Table 5.1: The design parameters of the XoR exoskeleton, including associated notation and values of the domain.

signals taken from a sensor placed on the gastrocnemius muscle of the right leg. This location was chosen because it resulted in less noise compared to sensors placed on the deep muscles of the thigh, and also because previous studies have shown that ankle muscle activations can be affected by active assistance at the hip joint [127]. Therefore, the gastrocnemius muscle should be susceptible to changes in location of both the thigh and shank cuffs.

The recorded data was segmented in to gait cycles and labelled as assisted or unassisted. The EMG signals were band-pass filtered using a zero-lag Butterworth filter, rectified, then low-pass filtered in order to produce a linear envelope for each full gait cycle of data, as described in Section 2.3.2. The average EMG signal for each gait cycle was calculated by integrating the corresponding envelope and dividing by cycle duration. These values were then averaged by label, and the percentage change in average EMG signal from unassisted to assisted walking was calculated.

5.3.4 Post-hoc Optimisation Protocol

After each trial set was complete, a Gaussian process regression (GPR) model was fit to the data using the MATLAB function *fitrgp*. This process resulted in two GPR models, g_t and g_s, representing the ground truth GP posterior for the thigh and shank, respectively. Here, g_t represents the change in activity of the gastrocnemius due to exoskeleton assistance as a function of the thigh cuff position, assuming constant shank cuff position, and similarly for g_s. By collecting EMG measurements in advance and sampling from g_t and g_s offline, the effectiveness of Bayesian optimisation could be investigated without the need for repeatedly taking experimental measurements using the exoskeleton, which was an intricate and time-intensive process.

The GP posterior functions g_t and g_s were sampled from as part of an optimisation process, using MATLAB's implementation of Bayesian optimisation *bayesopt*. The process was repeated for three acquisition functions (the MATLAB implementations of Probability of Improvement (PoI), Expected Improvement (EI) and Lower Confidence Bound (LCB) [123]) to determine whether this affected performance.

Since the objective functions of the optimisation (g_t and g_s) were stochastic,

a set of 100 optimisations were performed for each combination of acquisition function and objective function. Each optimisation was run for a total of 15 iterations. Once all optimisations were completed, the performance was quantified in terms of the mean and standard deviation of the number of iterations required to converge to within some region of the optimal cuff position.

5.3.5 Results

EMG Measurements

The EMG results from the XoR walking trial sets and corresponding ground truth GP posteriors g_t and g_s are shown in Figure 5.3. These results suggest that the location of the XoR cuffs does have a significant effect on the performance of the exoskeleton. In Trial Set 1, the largest observed reduction in EMG activity due to assistance was a reduction of 38.3%, occurring when the thigh cuff was placed at $x = 2.5$cm. In contrast, the most sub-optimal position for the thigh cuff based on the raw observations was $x = 4.0$cm, where the EMG activity was seen to increase by 25.0%. This represents an observed performance differential of 63.3%. According to the model obtained from GP regression, the optimal cuff location is located at $x = 1.9$cm, where the EMG activity is predicted to be reduced by 29.6% due to XoR assistance. The performance differential according to the GPR model was 39.2%.

In Trial Set 2, the optimal observed cuff placement was $y = 8.5$cm, with an EMG reduction of 42.5%. The most sub-optimal position based on the raw observations was $y = 4.5$cm, where the EMG activity was seen to increase by 12.8%, and therefore the observed performance differential had a value of 55.3%. The GPR model predicted the optimal cuff location to be at $y = 9.3$cm, where the estimated EMG reduction was 35.8%. The GPR model for the Trial Set 2 data predicted the performance differential to be 37.2%.

For reference, the analysis of the EMG measurements and subsequent GPR fitting is summarised in Table 5.2.

Bayesian Optimisation

The Bayesian optimisation performance was quantified according to the number of iterations required to converge to a certain minimum value of EMG re-

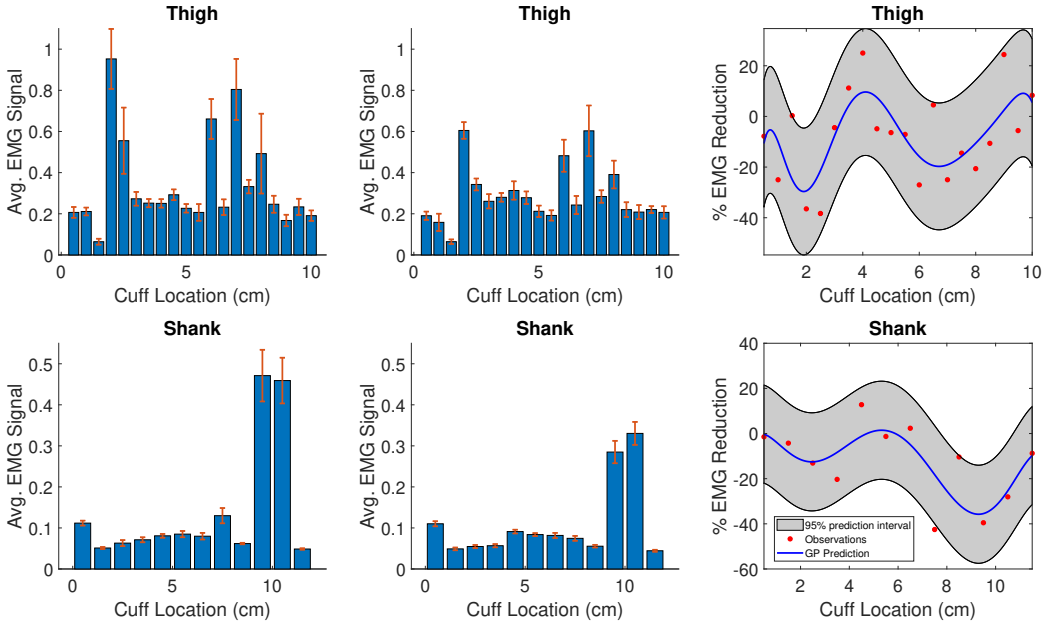

Figure 5.3: **Top row:** the average total EMG signal measured per gait cycle during unassisted walking (left) and assisted walking (centre) as well as the GPR model of the relative change in muscle activation from unassisted to assisted (right) for Trial Set 1. **Bottom row:** analogous results for Trial Set 2. Note that the GPR model fits shown in the rightmost figure of the top and bottom row, respectively, are equivalent to g_t and g_s, discussed in Section 5.3.4.

duction. The lowest value of reduction analysed was 0%, which corresponds to the cut-off between the XoR assistance hindering and helping the wearer. The performance was then analysed in intervals of 5% up to a maximum of 25%, since the true optimum EMG reduction was in the region of 30% for both the thigh and shank posteriors. To illustrate, a single optimisation process converging to a minimum value of 25% in N iterations would mean that after N iterations the predicted optimum EMG reduction is at least 25% and remains so during the remainder of the optimisation process.

The mean and standard deviation of the number of iterations required to reach each minimum value of EMG reduction was computed for the thigh and shank posteriors and for each of the three acquisition functions considered. The results from this analysis are presented in Figure 5.4. For Trial Set 1 we see good performance if the EMG reduction required is less than 20%, with the mean number of iterations required being less than 10. For EMG reductions

of greater than 20%, the mean number of iterations required sharply rises to more than 14. This is less than required for a linear search, but is subject to variability as evidenced by the error bars. For Trial Set 2 we see good performance in terms of mean iterations even up to the highest minimum EMG reduction of 25%.

For Trial Set 1 the performance of each of the tested acquisition functions is comparable in both mean and standard deviation across all values of EMG reduction. For Trial Set 2, the PoI acquisition function is slightly more effective than EI and LCB for minimum EMG reductions of greater than 15%, particularly in terms of standard deviation.

The Bayesian optimisation results are summarised for reference in Table 5.3, which gives the optimum acquisition function as well as mean and standard deviation of the number of iterations for each value of minimum EMG reduction.

5.3.6 Discussion

By collecting EMG data of a subject walking with assistance from the XoR exoskeleton over a range of cuff positions, we observed that changing the attachment point locations meaningfully affected the EMG signals received from the subject, and therefore how their muscles were being assisted by the exoskeleton. Notably, for some configurations of the exoskeleton cuffs, the EMG activity of the subject was increased by active assistance, rather than decreased. In particular, GPR models fit to the EMG data estimated the performance differential, measured in terms of reduction of EMG signals, between the optimal

	Trial Set 1		Trial Set 2	
	Observed	Modelled	Observed	Modelled
Position (cm)	2.5	1.9	8.5	9.3
Value (%)	−38.3	−29.6	−42.5	−35.8
Differential (%)	63.3	39.2	55.3	37.2

Table 5.2: The optimal cuff position, optimal percentage EMG reduction, and performance differential listed for both Trial Set 1 and Trial Set 2. For comparison purposes values are presented based on both the raw EMG results and the GPR models.

Minimum	Trial Set 1		Trial Set 2	
EMG Reduction	AF	Iterations	AF	Iterations
> 0%	LCB	2.39 ± 2.70	LCB	1.12 ± 0.50
> 5%	PoI	2.98 ± 3.31	PoI	2.09 ± 2.21
> 10%	PoI	5.77 ± 5.76	PoI	3.25 ± 3.41
> 15%	PoI	9.09 ± 6.96	PoI	4.43 ± 4.38
> 20%	LCB	14.7 ± 7.09	PoI	5.43 ± 4.97
> 25%	PoI	16.03 ± 5.76	PoI	6.31 ± 5.14

Table 5.3: A summary of the Bayesian optimisation results. The best acquisition function (AF) and mean ± standard deviation of iterations are presented for Trial Set 1 and Trial Set 2, in terms of what is required to converge to the minimum EMG reduction listed in the left-most column.

and most suboptimal cuff configurations to be approximately 40%. These results underline the need to optimise exoskeleton cuff placement to ensure assistive forces are applied correctly.

Collecting the experimental data required 20 measurements in the case of the thigh cuffs and 11 measurements in the case of the shank cuffs. Using Bayesian Optimisation, we were able to identify cuff configurations which performed well in terms of EMG reduction in a far lower number of measurements, as summarised in Table 5.3. Specifically, our analysis suggests that overall EMG reductions of more than 25% could be achieved in a mean of just 6-7 iterations when modifying the shank cuff position, and overall EMG reductions of more than 15% could be achieved in a mean of 8-9 iterations when modifying the thigh cuff position. Using Bayesian Optimisation as an alternative to sampling evenly over the entire domain can therefore potentially offer significant increases in efficiency, which could be particularly useful in a clinical setting such as a rehabilitation centre, where robotic exoskeletons such as the XoR could efficiently be adapted to provide effective assistance to multiple patients.

The Bayesian optimisation process was less successful in identifying the optimal thigh cuff position compared to the shank cuff position. A potential explanation for the difficulty in finding the true optimum of the posterior for Trial Set 1 is that, referring to Figure 5.3, the thigh posterior contains two peaks in EMG reduction (at approximately 2cm and 6.5cm, respectively)

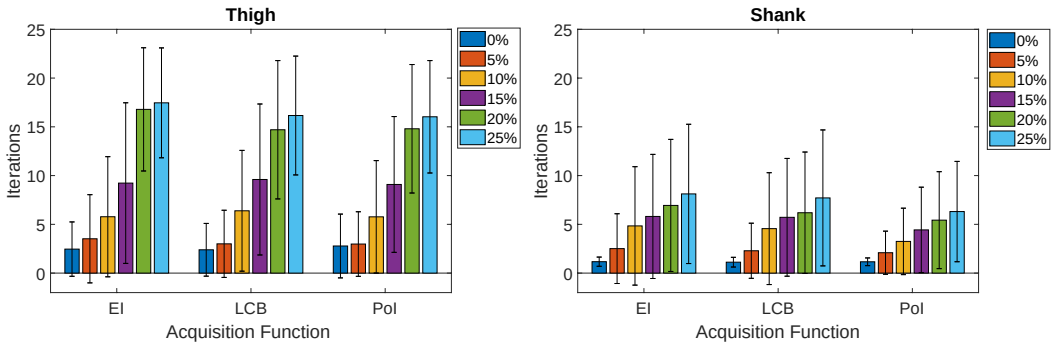

Figure 5.4: The mean and standard deviation of the number of iterations required to converge to a certain minimum EMG reduction for the thigh (**left**) and shank (**right**) GP posteriors. The bars denote the mean number of iterations required to ensure that the point found by the optimisation results in at least a reduction in EMG activity corresponding to some minimum level. Note the legend which illustrates the ordering of minimum EMG reduction zones.

which are close in magnitude. Therefore, the Bayesian optimisation process is more susceptible to becoming trapped in the local minima near the $x = 6.5$cm cuff position. This is not true for the shank posterior, which has a marked global minimum near a cuff position of 9cm.

The Bayesian optimisation process was not significantly affected by the choice of acquisition function, but overall PoI gave the best results for both of our Trial Sets.

A potential source of error in the collected data came from the relatively strenuous data collection process, which introduced subject sweating and fatigue, exacerbating the problem of noisy EMG signals. Additionally, it was difficult to ensure that the position of the sensor was unchanged between walking trials, due to interaction between the exoskeleton and the EMG sensor. To offset these issues, EMG measurements were taken during both passive and assisted walking, and the relative improvement is reported rather than the absolute EMG signals. A potential alternative to using EMG measurements would be to use a respiratory device to measure metabolic rate, similarly to Kim et al. (2017) [59]. Alternatively, kinematic and kinetic data could be collected during walking trials to allow for human effort to be computed using a human-exoskeleton musculoskeletal model [12, 36, 75].

A further test of this technique would be how it performs on higher dimen-

sional problems. In the case of the XoR, considering the 2D problem of optimising the thigh and shank cuff locations simultaneously would require more than 500 measurements using linear search (assuming a resolution of 0.5cm). Bayesian Optimisation could potentially be used as an alternative which could actually be applied in practice. Re-applying this investigation to the 2D case is a potential source of further work.

Overall, we have shown the successful application of Bayesian optimisation to improve the performance of a lower-body exoskeleton by modifying freely adjustable design parameters. This result, combined with recent previous works on human-in-the-loop optimisation for exoskeleton control, illustrates the potential usefulness of Bayesian optimisation as a tool for both the control and design of exoskeletons.

Before moving on from this chapter, it is pertinent to note that a key strength of the human-in-the-loop optimisation framework — the fact that by sampling directly from the subject of interest highly personalised system parameters can be learned — also potentially limits its applicability. In the example presented in this chapter, the identification of optimal cuff locations required a significant period of data collection to produce EMG data over the space of cuff locations. This requirement may significantly limit the method if the subject is experiencing an injury or gait pathology which makes carrying out lengthy data collection protocols or performing repetitive movements difficult. Currently, the HIL framework is largely carried out on healthy individuals [17, 59, 99, 121], and further advances in HIL protocols are necessary before it can be applied to assist patients in a medical or rehabilitative setting. In the next chapter, we will discuss an approach which utilises musculoskeletal modelling to reduce the time investment required by human-in-the-loop optimisation protocols, thus reducing the physical strain on subjects.

Chapter 6

Optimising Assistive Torques for Gait Efficiency

A particularly common design goal for powered exoskeletons and exosuits is to reduce the metabolic cost of walking [9, 61, 128, 129]. Devices which achieve this goal could be used either to augment human locomotion capabilities, for example to assist humans carrying heavy loads over long distances [130], or for long-term mobility rehabilitation or assistance of movement-impaired or elderly people [65]. This latter use case is of particular relevance to modern society, which increasingly faces the issue of mobility loss tied to an aging population [131, 132] along with the associated health problems and reduction in quality of life [133]. However, designing exoskeleton controllers which can efficiently assist human locomotion has proven to be a challenging problem, as the efficacy of these devices is strongly dependant on the timing and

magnitude of the delivered assistance [13, 134–137]. Moreover, this issue is compounded by the fact that, due to variations in age, size, limb proportions, and even internal locomotion strategies, humans can exhibit significant differences in walking styles [48, 138, 139]. The consequence of this is that generic exoskeleton controllers may be suboptimal for a large number of individuals.

Human-in-the-loop optimisation techniques, introduced in the previous chapter, have emerged as a solution to this problem. Using HIL optimisation, researchers have been able to identify individualised control patterns which result in significantly greater energetic savings than traditional control schemes [99]. However, despite the impressive energetic cost reductions achieved by this method over the past five years, a clear limitation exists: the significant time investment required to produce optimised assistance profiles. This is particularly relevant when the aim is to reduce metabolic cost, as to do so typically involves the measurement of noisy, low frequency calorimetric data, which requires large measurement times in order to produce accurate readings [60]. This presents an issue for two main reasons: firstly, as the time spent walking increases, so too does the likelihood that the subject will become fatigued. Not only is this uncomfortable for the subject, increasing the potential for early termination of the process, but due to physiological changes which reduce the energy efficiency of fatigued muscles [140], further measurements cannot be considered valid. Secondly, long measurement times effectively place limitations on the complexity of the optimisation objective. For example, relatively simple control profiles offering unimodal assistance patterns may be used [17, 99], albeit to strong effect. In order to explore the use of more complex control parameterisations which may offer even greater energetic cost reductions, or to optimise the control of multi-joint exoskeletons and exosuits, more efficient HIL optimisation protocols are necessary.

This problem of excessive runtimes in HIL protocols is well recognised, and recent works have attempted to find solutions by implementing early-stopping within the optimisation process [141] or by replacing the use of respiratory gas analysis with machine learning models on less coarse data inputs [142]. In this chapter, an alternative approach is proposed which leverages the strengths of musculoskeletal modelling [40]. Simulation-based approaches have proven useful both for the analysis of exoskeleton-assisted locomotion [12, 36] and the

design of exoskeleton controllers [143]. Utilising dynamic models driven by musculo-tendon actuators [38, 69, 70, 144] combined with models of muscle energetics [145, 146] the metabolic power consumption of movements can be readily estimated [76, 143], providing approximations to the ground truth data from calorimetry [146, 147]. Musculoskeletal models can easily be scaled to match a subject in terms of proportions, but adapting muscle parameters (for example, to differentiate between subjects with different muscle strengths) is challenging. Furthermore, these models do not by themselves account for innate differences in walking styles. By combining musculoskeletal modelling with HIL optimisation, we are able to efficiently simulate the metabolic cost of walking using a scaled generic model, while retaining the ability to learn highly specific and optimised controllers from motion data collected directly from the subject.

To summarise, in this chapter we present a HIL methodology which optimises the assistive torque patterns applied by exoskeletons. We conduct musculoskeletal simulations online in order to simulate metabolic rate, significantly reducing the time investment required to sample specific torque profiles when compared to implementations relying on calorimetric measurements. We then evaluate the effectiveness of the method for 7 subjects wearing an active pelvis orthosis.

6.1 HIL Implementation

In this section the specific components of the HIL protocol are outlined using terminology from Chapter 5. In particular, we specify the real-time measurement, performance metric, optimisation step and system update from Figure 5.1.

6.1.1 Real-time Measurement

The real-time measurement in the protocol consists of marker trajectories and external forces collected in the University of Edinburgh Gait Lab. Here, the external force data includes contributions from ground reaction forces as well as torques applied by the APO. The raw data is segmented in to synchronised

gait cycles during the data processing pipeline. Therefore, we have

$$\mathrm{P} = \{\mathbf{p}_1, \mathbf{p}_2, \ldots, \mathbf{p}_n\}, \tag{6.1}$$

$$\mathrm{F} = \{\mathbf{f}_1, \mathbf{f}_2, \ldots, \mathbf{f}_n\}, \tag{6.2}$$

where P and F contain marker and force data, respectively, for n total gait cycles. Note that vectors in this section are indexed by time, i.e. $\mathbf{p}_1(t)$, but we are assuming this implicitly to simplify notation.

6.1.2 Performance Metric

The performance metric calculation occurs over several steps. For each gait cycle, we first use the collected marker data to define the motion of the model via inverse kinematics (Section A.2),

$$Q = \{\mathbf{q}_1, \mathbf{q}_2, \ldots, \mathbf{q}_n\}. \tag{6.3}$$

Then, we use the modelled joint trajectories and the measured external forces to find the set of muscle activations which correspond to this motion via static optimisation (Section A.6),

$$\mathrm{A} = \{\alpha_1, \alpha_2, \ldots, \alpha_n\}, \tag{6.4}$$

and compute the metabolic energy rate using a muscle energetics model (Section A.7),

$$\mathrm{E} = \{\epsilon_1, \epsilon_2, \ldots, \epsilon_n\}. \tag{6.5}$$

Next, we compute the normalised metabolic rate for each cycle. For the i^{th} gait cycle, which begins at time t_{i-1} and ends at time t_i, we compute the rate of energy consumption, normalised by subject mass M, as follows:

$$V_i = \frac{1}{M(t_i - t_{i-1})} \int_{t_{i-1}}^{t_i} \dot{\epsilon}_i(t) dt. \tag{6.6}$$

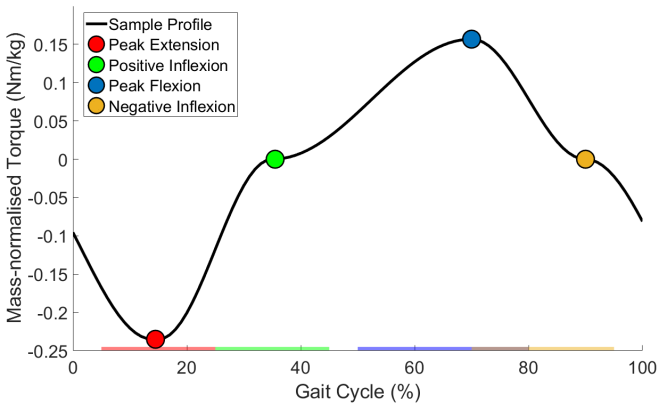

Figure 6.1: The control parameterisation utilised for this HIL study. The four parameters determining the shape of the assistance profile are represented by coloured dots. Each parameter has an associated allowable range which is indicated by a shaded region on the x axis.

The final step in our performance calculation is to average the simulated metabolic rate over all collected gait cycles:

$$V_s = \frac{1}{n} \sum_{i=1}^{n} V_i. \tag{6.7}$$

We refer to V_s as the simulated metabolic rate. Note that, similar to the experimentally measured metabolic rate V_e from Equation (2.6), V_s expresses an approximation to the ground-truth normalised metabolic rate, V.

6.1.3 System Update

The component of our system which we seek to optimise is the assistive torque profile applied by the APO. We define a generic assistance profile which is constructed as a piecewise combination of sinusoidal curves linking 4 node points, $\mathbf{p} \in \mathbb{N}^4$. In order from p_1 to p_4, the node points correspond to the points in the gait cycle at which maximum extension, positive inflexion, maximum flexion and negative inflexion occur, respectively. This generic profile is shown in Figure 6.1. Mathematically, the control signal applied via the APO is a piecewise combination of sinusoids which takes the following form:

$$u(x,\mathbf{p}) = \frac{1}{2}\begin{cases} \tau_e(\sin(g(x,\mathbf{p})+\frac{\pi}{2})-1) & 0 \le x \le p_1, \\ \tau_e(\sin(g(x,\mathbf{p})-\frac{\pi}{2})-1) & p_1 \le x < p_2, \\ \tau_f(\sin(g(x,\mathbf{p})-\frac{\pi}{2})+1) & p_2 \le x < p_3, \\ \tau_f(\sin(g(x,\mathbf{p})+\frac{\pi}{2})+1) & p_3 \le x < p_4, \\ \tau_e(\sin(g(x,\mathbf{p})+\frac{\pi}{2})-1) & p_4 \le x \le 100, \end{cases} \tag{6.8}$$

where we define

$$g(x,\mathbf{p}) = \pi\begin{cases} \frac{(x+101-p_4)}{(100+p_1-p_4)} & 0 \le x \le p_1, \\ \frac{x-p_1}{p_2-p_1} & p_1 \le x < p_2, \\ \frac{x-p_2}{p_3-p_2} & p_2 \le x < p_3, \\ \frac{x-p_3}{p_4-p_3} & p_3 \le x < p_4, \\ \frac{x-p_4}{100+p_1-p_4} & p_4 \le x \le 100. \end{cases} \tag{6.9}$$

Here, $x \in [0,100]$ is the point within a gait cycle expressed as a percentage, while τ_e and τ_f define the magnitudes of the negative and positive peaks, respectively. These magnitudes are determined according to the following relationships:

$$\tau_e = cm, \tag{6.10}$$

$$\tau_f = \frac{2}{3}\tau_e, \tag{6.11}$$

which normalise the assistive torques by subject mass, m. The constant c was chosen based on feedback regarding comfort from subjects, while keeping in mind the hardware limitations of the APO. The conversion factor of 2/3 between extension and flexion torque magnitude is an approximation of what is observed in human gait data [148]. Compared to two existing HIL implementations which have focused on providing unidirectional assistance via 2-dimensional [99] or 3-dimensional [17] control laws, this 4-dimensional control law allows for a smooth transition between extension and flexion assistance. The general shape of this parameterisation was selected due to a close match to experimentally recorded measurements of human hip flexion-extension torques.

The following constraints were placed on the control parameter domains:

$$p_1 \in [5, 25], \tag{6.12}$$
$$p_2 \in [25, 45], \tag{6.13}$$
$$p_3 \in [50, 80], \tag{6.14}$$
$$p_4 \in [70, 95]. \tag{6.15}$$

These ranges were selected to limit the search space for the optimisation while still allowing for significant flexibility in the possible assistance patterns, and in particular were chosen so as to allow for assistance profiles which mirror human joint torques [148].

6.1.4 Optimisation Step

We employ the use of Bayesian optimisation (introduced in Section 5.2) in order to drive the selection of control parameters between loops of the HIL protocol. This approach is particularly well suited to minimising functions which are expensive to evaluate, and as such has been used successfully in a number of previous HIL optimisation protocols [59, 99, 120] which by their nature involve lengthy data collection steps. Here, the function we are aiming to minimise is the unknown relationship between the control parameters and the ground truth metabolic rate, i.e.

$$V = f_s^C(\mathbf{p}). \tag{6.16}$$

We use the subscript s to denote that the learned policy is specific to each subject and the superscript C to denote an underlying set of context parameters, such as walking speed and inclination, which may also affect this relationship.

Our optimisation process is implemented in MATLAB using MATLAB's *bayesopt* function, which is an implementation of Bayesian optimisation, and takes place over a total of 24 iterations. The first 12 samples are randomly selected within the domain, so as to avoid early convergence to a local minima, while the latter 12 follow from optimisation of the *Expected Improvement* acquisition function [123].

6.2 Methodology

6.2.1 Hardware

Our experiments were conducted in the Gait Lab at The University of Edinburgh, making use of the Vicon system and instrumented treadmill to measure marker trajectories and ground reaction forces, respectively. Exoskeleton assistance was provided by the APO, while the Cortex Metamax 3BR2 system was used to experimentally quantify metabolic rate. Full details of the equipment including the raw data processing procedure for all data streams is provided in Chapter 2.

It is worth recalling Equation (2.6), which describes how metabolic rate is approximated from breath-by-breath calorimetric data, and is reproduced below for reference

$$V_e = \frac{4.184}{60}(3.972 + 1.078R)\dot{V}O_2. \tag{6.17}$$

Recall that V_e denotes experimentally measured metabolic rate (rate of energy consumption per unit mass), which we consider to be an approximation to the ground truth metabolic rate V. In accordance with the steady-state strategy for computing metabolic rate outlined in Section 2.4.2, V_e was averaged over the final 2 minutes of collected data to produce a single value per measurement.

6.2.2 Control Modes

Four control modes for the APO were utilised for this study. The first two, **transparent mode** and **AO mode**[24], are default APO controllers which are described in detail in Section 2.5. The latter two control modes were developed for the purpose of this investigation and are introduced below.

HIL mode

This mode corresponds to the HIL-compatible controller outlined in Section 6.1.3, implemented in LabView to run on the APO. Heel-strike events, detec-

[24] Adaptive Oscillator mode.

ted in real-time using the ground reaction force data, are used to scale each profile to match the cadence of each subject by averaging the stride time of the previous 3 gait cycles.

Generic mode

This mode is based on a previous study in which the authors investigated the effect of assistance onset timings on the performance of a hip exoskeleton [13]. A range of possible onset timings for hip flexion and extension assistance was tested on a set of 10 healthy subjects. They found that on average the combination of timing parameters which reduced metabolic rate most effectively was 92.2% for the onset of hip extension assistance and 40.2% for the onset of hip flexion assistance. The duration of applied assistance was 25% for both flexion and extension. This particular study was chosen over similar alternatives [134–136] due to similarities in exoskeleton hardware (i.e use of a rigid pelvis exoskeleton).

A controller was implemented in LabView to allow the APO to apply this generic torque profile to subjects. For consistency with the HIL controller, the relationship between peak flexion and extension assistance specified in Equation (6.11) was enforced.

6.2.3 Simulation Pipeline

A simulation framework was implemented in OpenSim to approximate metabolic rate from raw motion data. The human-APO model, introduced first in Chapter 3 but shown for reference in Figure 6.2, served as the generic musculoskeletal model. OpenSim was used to:

1. Scale the generic model for each subject.

2. Compute joint kinematics from measured marker trajectories.

3. Compute muscle activations from joint kinematics, measured ground reaction forces & APO torques.

4. Compute metabolic cost from muscle activations.

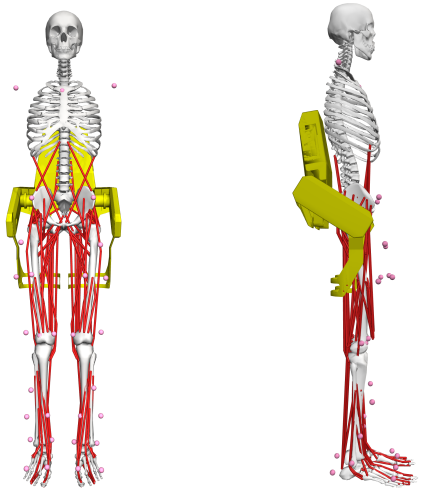

Figure 6.2: The human-APO musculoskeletal model. The APO (shaded yellow) is constrained to the gait2392 model via weld joints. Model markers (shown in pink) are used to scale the model and perform inverse kinematics using experimental markers collected from motion capture.

More information on the mathematics underpinning these OpenSim methods is provided in Appendix A. Custom code was developed to execute the raw data processing and simulation steps online, utilising the OpenSim API and the MATLAB parallel processing toolbox. This code forms a significant part of the *ECHO* MATLAB toolbox[25], which was custom developed for this project.

6.3 Experimental Design

Our experimental protocol consisted of a model calibration step followed by two distinct phases: the parameter identification phase, in which subject specific control parameters were identified, and the verification phase, in which the metabolic cost of walking with a number of control modes was evaluated for each subject. In order to avoid subject fatigue, these phases were conducted over a two day period. Figure 6.3 illustrates the main steps which took place over each day.

All subjects completed the same verification phase, however for comparison purposes two subjects undertook an identification phase based on a grid sampling procedure, while for the remaining five subjects the HIL protocol was used. The identification-phase search strategy employed for each subject is noted in Table 6.1.

The details of each phase (model calibration, parameter identification, and

[25] https://github.com/DanielFNG/echo

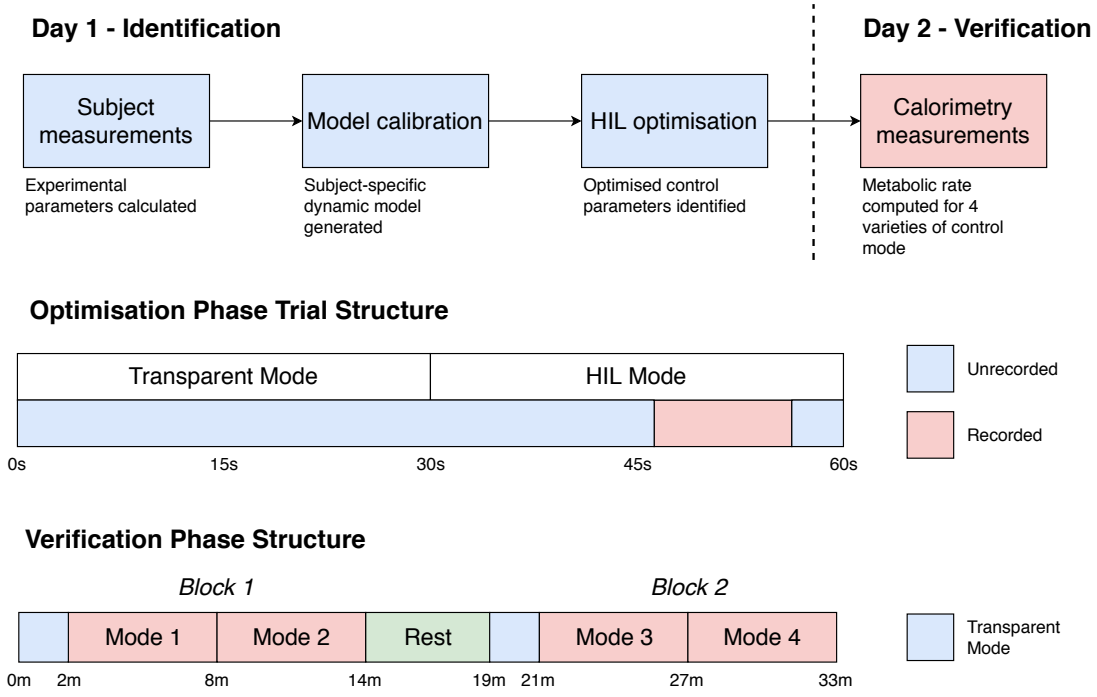

Figure 6.3: **Top**: the sequence of steps which took place over the 2-day experimental protocol. **Middle**: the structure of a single walking trial within the HIL optimisation step. The upper layer of the figure indicates whether the APO was in transparent or active mode, while the lower layer shows the period during which data was collected. **Bottom:** the structure of the verification phase, during which subjects walk whilst experiencing a number of APO assistance modes. The ordering of the four active assistance modes (red background) was randomised for each subject.

verification) are outlined in the forthcoming sections.

6.3.1 Model Calibration

This step ensured that walking speed and musculoskeletal model mass was correctly calibrated for each subject. Subject mass and leg length were measured at the beginning of the experiment and are presented in Table 6.1. The baseline walking speed for each subject was determined according to the principle of dynamic similarity [111], as follows:

$$v = \sqrt{F_r g L}, \tag{6.18}$$

where v is baseline walking speed, F_r is the Froude number (chosen here to be 0.1), g is gravitational acceleration, and L is leg length (measured as the vertical distance from the greater trochanter to the medial malleolus). All subjects were made to walk at a pace equivalent to 120% of their baseline walking speed.

During this step, marker data from a static pose was collected and used along with subject mass to scale the generic human-APO model for each subject. Participants then underwent a 60s walk with the APO in transparent mode. Gait cycles from the latter 30s of this transparent mode data were used to produce a dynamically consistent scaled model via the RRA algorithm [40], and to identify the preferred stride time for each subject, which was taken as the average time of stride across all gait cycles. The preferred stride times for each subject are presented in Table 6.1.

6.3.2 Parameter Identification

During the parameter identification step, subjects undergoing the HIL-based search strategy completed 24 consecutive walking trials, each of which corresponded to a single measurement for the optimisation. Each trial lasted 60s and consisted of 30s walking in transparent mode followed by 30s of assisted walking. Ten seconds of motion data was collected from the end of the assisted period, and used to compute the mean metabolic rate for each tested control

Table 6.1: Physical & Experimental Subject Parameters

ID	Mass (kg)	Height (m)	LL (m)	ST (s)	PAT (Nm)	Identification Mode
1	67.3	1.80	0.93	1.15	15.8	HIL
2	71.3	1.82	0.84	1.09	10	HIL
3	79.3	1.74	0.75	1.03	10	HIL
4	58.6	1.78	0.84	1.09	10	HIL
5	59.9	1.68	0.75	1.03	8	HIL
6	81.4	1.81	0.83	1.08	15	Grid Search
7	68.3	1.62	0.79	1.06	10	Grid Search

The acronyms LL, ST & PAT correspond to leg length, stride time and peak APO torque, respectively.

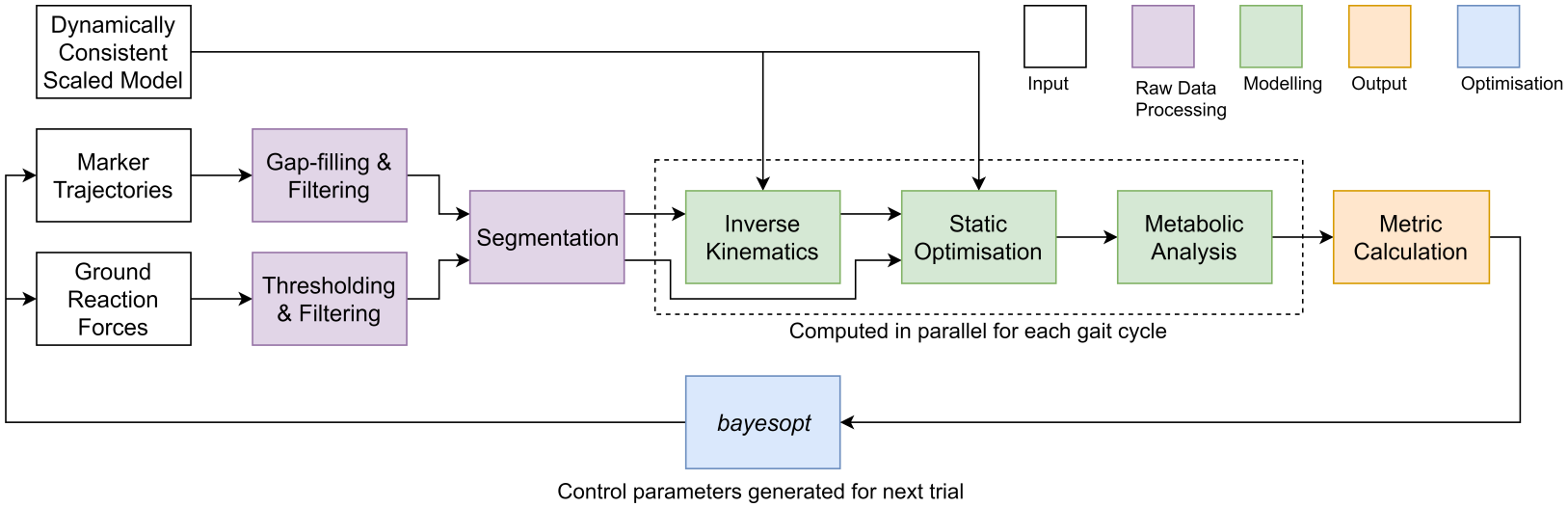

Figure 6.4: A schematic outlining the structure of a single trial taking place during the identification phase. Raw data is collected and run through a series of processing steps, producing data for 4 gait cycles. The normalised metabolic rate is computed for each cycle and averaged to produce a single measurement for the trial. This measurement is input to the Bayesian optimisation algorithm, which then suggests control parameters for the next trial.

parameterisation. For reference, the trial structure described here is illustrated in Figure 6.3. Subjects were given feedback in the form of a 4-second audio cue prior to any change in assistance mode, but after recording was completed for that trial.

The data processing pipeline for each trial is presented in Figure 6.4. Up to eight gait cycles were selected from the 10s of motion data collected in each trial. Using OpenSim's modelling algorithms, the model kinematics, muscle activations and corresponding metabolic rates were computed. Due to the limited time available to complete the data processing, the MATLAB Processing Toolbox was employed to execute these modelling steps for each gait cycle in parallel. The normalised metabolic rate was then calculated before being passed to the *bayesopt* function to select the new control parameters.

The control parameters **p** were updated for each trial according to the optimisation step outlined in Section 6.1.4. The first 12 sets of control parameters were selected randomly, so as to avoid early convergence to a local minima, while the latter 12 were determined automatically by the Bayesian optimisation algorithm. Subjects were given a 5 minute rest period between the first and second block of walking trials. After 24 iterations the optimal control parameters identified for each subject were noted in preparation for the verification phase.

6.3.3 Verification

The verification step is designed as a sanity check on the results of the parameter identification phase. We collect indirect calorimetry from all subjects walking with assistance from the APO in HIL mode, with the optimised control parameters identified during each subject's identification phase. This data is used to compute the steady-state approximation of metabolic cost (see Section 2.4.2), which is widely used in literature where metabolic cost of movement is studied [9, 61, 62]. Then, we contrast this result with further indirect calorimetry measurements taken in other exoskeleton control modes in order to objectively quantify the performance of the HIL-optimised control scheme. The control modes utilised by the APO are outlined in a generic form in Section 6.2.2.

Subjects walked at the speed listed in Table 6.1, so as to match their walking speed during the parameter identification phase, and completed a 6-minute walk per assistance mode in two blocks of 12 minutes each. The blocks were preceded by 2 minutes of warm-up walking in transparent mode, and were separated by a 5 minute rest period. The ordering of the assistance modes was fully randomised for each subject. For reference, the structure of the verification phase is depicted in Figure 6.3. Reference measurements of resting metabolic rate (RMR) and free walking (FW) metabolic rate were also obtained, immediately prior to the main verification phase procedure.

In addition to collecting quantitative metabolic data, participants were also asked to rate the assistance modes they experienced in terms of both comfort and assistance quality. This was done at 3 distinct points during the verification process:

1. Following Block 1, subjects were asked which mode was most comfortable and which mode provided the best assistance between Mode 1 and Mode 2.

2. The same question was asked following Block 2, but with Mode 3 and Mode 4 as possible answers.

3. Upon completion, the same questions were asked, but with any assistance mode allowed as possible answers.

The purpose of the first two questions was to provide subjects with a reference point for the relative strength of each assistance mode. Only the responses to question 3 were recorded and are provided as data points in Section 6.4. A copy of the questionnaire sheet used during the experiment is provided in Appendix B.3.

6.4 Results

All subjects successfully completed both stages of the experimental protocol. In Table 6.2, the optimised control parameters identified for each subject are listed, along with the metabolic rates found in each tested mode of assistance during the verification phase. The RMR value for S1 is unavailable due to an

Subject ID	Control Parameters (%)				Experimental Metabolic Rate (Wkg^{-1})					
	p_{ext}	p_{rise}	p_{flex}	p_{fall}	RMR	Free Walking	Transparent	AO	HIL	Generic
1	9	26	50	88	-	4.56	5.98	5.89	4.96	5.42
2	5	32	71	75	2.13	4.57	4.75*	**4.72**	4.74	4.75
3	5	26	76	83	1.81	4.54	4.35	4.40	**4.26***	4.06
4	5	31	51	84	1.47	4.66	4.81	4.91	4.68*	**4.86**
5	18	27	75	80	1.20	3.42	3.70	3.61	**3.34***	3.35
6	10	30	65	75	1.35	4.11	4.48*	4.66	**4.46**	4.65
7	5	26	50	80	1.50	3.84	3.77	-	**3.90***	3.98
Mean	8.14	28.29	62.57	80.71	1.58	4.24	4.55	4.58	4.35	4.44
Standard Deviation	4.85	2.63	11.98	4.75	0.34	0.47	0.77	0.74	0.55	0.69

Table 6.2: Optimised control parameters & metabolic rate data.

error in the data collection during this period; similarly, the AO measurement for S7 was discarded due to a failure of the adaptive oscillator algorithm to synchronise with the gait of the subject.

The mean metabolic rates for each assistance condition are averaged over all subjects and are collated at the bottom of Table 6.2. On average, only the generic and HIL-optimised controllers are able to reduce metabolic cost relative to transparent mode walking. Among those modes in which the subject is encumbered by the APO, the lowest metabolic cost is incurred by the HIL-optimised control scheme. On the level of individual subjects, the HIL-optimised control scheme performed the best for 4 of the tested subjects, with all other control modes performed best for 1 subject each. These results are summarised in Figure 6.6a.

We found that the shape of the optimised assistive torques varied significantly between subjects. In Figure 6.6d the mean optimised torque profile over all subjects is shown, alongside the individual torque profiles identified for each subject, while the standard deviation associated with each control parameter is provided in Table 6.2. Our data suggests that the point of peak hip flexion moment (p_{flex}) in particular is the most susceptible to variations between subjects, exhibiting more than twice the error range of any other parameter. Meanwhile, the rising point of inflexion (p_{rise}) is the control parameter which exhibits the least variance.

Convergence is difficult to quantify for Bayesian optimisation protocols, due to a tendency for the algorithm to balance exploring areas of the objective function which are either high variance or near the currently expected minimum. In Figure 6.5a, we display the evolution of the iteration at which the minimum value of simulated metabolic cost was achieved. This quantity indicates how many iterations have passed since the Bayesian optimisation has successfully sampled a lower point of the objective function, i.e. found a control parameterisation resulting in lower metabolic rate, in this case. From this figure, we see a levelling off of the minimum index trace for each subject, which ranges from iteration 6 at the earliest for S5 to iteration 18 at the latest for S4. A more detailed example evolution of control parameters is shown for a specific subject in Figure 6.5b.

For Subject 2 - Subject 7, the values in bold in Table 6.2 denote the assist-

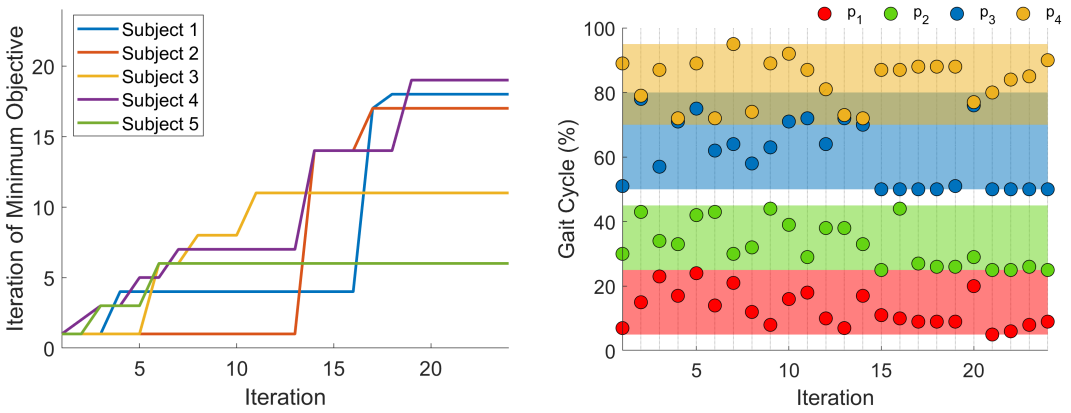

(a) (b)

Figure 6.5: **(a)** The trace of the iteration at which the minimum objective value was observed for each subject who underwent the Bayesian-optimisation based search strategy. **(b)**A diagram showing a sample of control parameter evolution for a single subject (S1). Shaded regions show the allowable values for the corresponding parameter. The random selection of control parameters is evident in the first 12 iterations, after which point the Bayesian optimisation algorithm begins to converge towards a solution, indicated here by stars.

ance mode which the subject identified as providing the best assistance, while the values with an asterisk denote the assistance mode identified as most comfortable. The total number of subjects identifying each assistance mode as either most comfortable or the mode which provided the best assistance is displayed in Figure 6.6b and Figure 6.6c, respectively. From these graphs, we see that the HIL-optimised mode was the most likely to result in an assistance profile which was perceived as comfortable and helpful amongst all assistance modes.

6.5 Discussion

In this section, we discuss the metabolic results & participant questionnaire feedback presented in Table 6.2. In addition, we present a brief analysis of the natural variation in walking style between two of our subjects using techniques from Chapter 4.

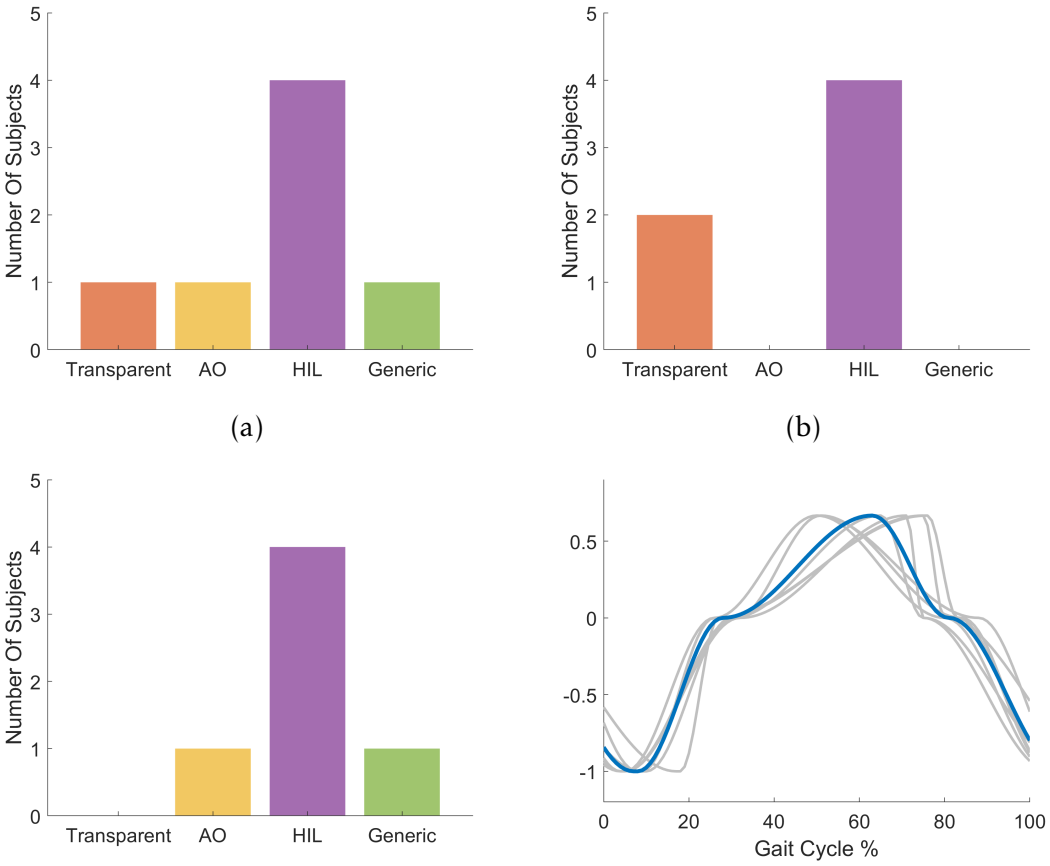

Figure 6.6: **(a)** The number of subjects for which each tested exoskeleton control mode resulted in the largest reduction in metabolic cost. **(b)** The number of subjects who selected each APO control mode as the most comfortable. **(c)** The number of subjects who selected each APO control mode as providing the best level of assistance. **(d)** The mean control profile (blue) obtained by averaging the obtained control parameters over all subjects, overlaid with the standard deviations (red) of each control parameter at the corresponding node points. To illustrate the range of assistance profile shapes, each individual optimised profile is also shown (light grey) with extension magnitude normalised to 1.

6.5.1 Metabolic Cost

The HIL-optimised control scheme resulting from our framework performs favourably compared to the two other active controllers, and is the control mode which results in the lowest assisted metabolic cost for most subjects, as

shown in Figure 6.6a. However, our results also indicate that the efficacy of the exoskeleton control modes is highly affected by variations between subjects. To better illustrate the relative performance of the tested control schemes, we treat the cost of transparent-mode walking as a baseline and calculate relative reduction in energetic cost for the AO, generic and HIL controllers. These results are displayed in Figure 6.7 for Subject 1 and Subject 5. We observe that the metabolic benefit of the AO control scheme is minimal in both cases. Meanwhile, the generic control scheme offers a marked reduction in metabolic cost of approximately 10% when compared to the baseline for both subjects. We find that using the subject-specific control parameters identified by our optimisation, we are able to further improve energy efficiency by a factor of 1.86 when compared to the generic controller for S1, compared to no relative gain for S5.

Though the generic mode performs similarly for S1 and S5, the results are quite different across the remainder of our dataset, and indeed the generic control mode results in increased metabolic cost for S4, S6 and S7. Comparatively, the HIL-optimised mode results in decreased metabolic cost for all subjects except S7. This is an interesting and quite unexpected result - the generic control mode was initially expected to perform fairly well for most or all subjects, being based on a controller which was optimised to be effective on a group level

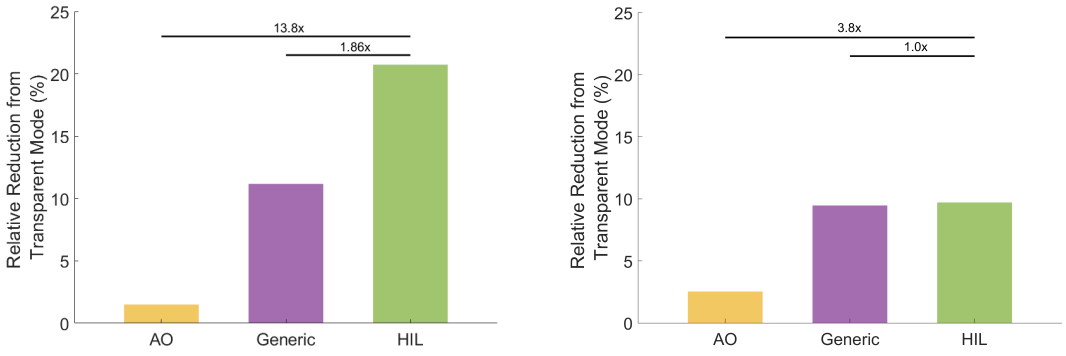

Figure 6.7: The relative reduction in metabolic rate of the active control modes for **(a)** S1 and **(b)** S5, expressed as a percentage of the energetic cost of walking in transparent mode. Labels indicate the relative magnitude of reduction between modes.

[13]. The poor performance of the generic mode over a portion of our dataset may indicate that the optimal exoskeleton assistance strategy is even more sensitive to subject parameters than was expected.

Also interesting to note is that subjects of similar mass and assistance level can exhibit markedly different results for each of the tested assistance modes. This is clear when comparing the results for e.g. the HIL-optimised and generic modes for S4 and S5. Typically, human-in-the-loop optimisation protocols use force & torque magnitudes which are fixed or scaled relative to subject mass. These results suggest that a more appropriate approach may be to include the maximum torque as an optimisation parameter. It is likely that this would require too significant of a time investment for traditional HIL frameworks which rely on calorimetry; however, this may be an interesting source of future work for our simulation-based framework.

6.5.2 Participant Feedback

Although the primary objective of this work was to target metabolic cost reductions, the post-experiment questionnaire results (see Figure 6.6) indicate that our control parameterisation was both comfortable and gave the perception of increased assistance. It is particularly notable that no other active control mode was selected as the most comfortable. Although previous work has shown that subject perception does not necessarily match true metabolic cost [13], it is likely that subject comfort would be an important factor in promoting adherence to rehabilitation regimes or exoskeleton assistance programs, especially if the subject required assistance for extended periods of time. Therefore, increased comfort is a desirable characteristic.

Thus far, the focus of this work has been on collecting data from healthy participants, with a view to targeting exoskeleton assistance for metabolic rate reduction. For patients who deviate further from normal gait patterns, the HIL-optimised results seen here are likely to be magnified. Our framework, while implemented here using metabolic cost as the objective function, could be easily extended to further use-cases due to the depth of analysis enabled by the musculoskeletal modelling approach. For example, rather than looking at metabolic rate as a whole, physiotherapists could select specific muscles to

target for assistance or training, depending on the needs of the subject. Such muscles could include deep muscles which are hard to target experimentally (e.g. via EMG sensors). A source of further work for our framework will be to investigate alternative objective functions, with the aim to recruit patients with gait pathologies.

A key motivation for pursuing a human-in-the-loop optimisation protocol with a simulated objective function was the potential benefit in terms of time investment. The results we have presented here involve only 60s per iteration of the HIL process, compared to at least 120s, but often longer, for methods based on calorimetry [17, 59, 99, 118, 119]. A potential weakness of our approach, however, is a reliance on modelling assumptions which are not present in tradition HIL protocols. An additional source of further work is to test alternative models of human-exoskeleton systems and of metabolic energy consumption.

6.5.3 Gait Analysis

The differences in optimised control strategies seen in Figure 6.6d are likely due in part to the natural variations occurring between subjects, both in terms of the physical characteristics listed in Table 6.1 and in specific locomotion strategies. To elucidate these internal differences, a sequence of diagrams is provided to compare and contrast various aspects of gait between two of the participants. In Figures 6.8a and 6.8b, respectively, we compare the hip kinematics and mass-normalised hip torques between Subject 1 and Subject 2, as measured during transparent walking while wearing the APO. In Figure 6.9b, we use the same dataset to compare a range of kinematic and dynamic gait metrics between the two subjects. These subjects were chosen as S1 experiences the most benefit from exoskeleton assistance, compared to S2 who experiences almost no change in any mode according to the values in Table 6.2.

The metrics used along with their definitions are as follows:

- Step width (SW) is defined as the medial-lateral distance between the heel of the subject at consecutive heel strikes.

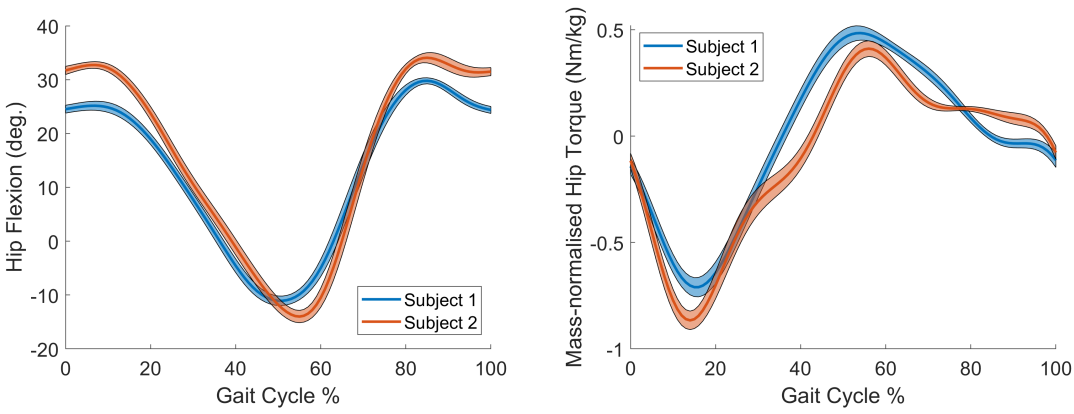

(a) (b)

Figure 6.8: A comparison of gait data between Subject 1 & Subject 2. These plots were obtained from data collected during the model calibration phase, which corresponds to 30s of walking in transparent mode. **(a)** Mean and standard deviation of hip flexion/extension kinematics. **(b)** Mean and standard deviation of hip flexion/extension moments, normalised by subject mass.

- Stance ratio (SR) is defined as the proportion of the gait cycle in which the leading foot is in stance.
- GRF peak ratio (GR) is the ratio between the primary and secondary peaks of the vertical ground reaction force of the leading foot (see Figure 6.9a).
- Hip flexion/extension range of motion (HK) is the absolute difference between the points of maximum and minimum hip flexion.
- Peak to peak hip flexion/extension torque (HT) is the absolute difference between the maximum and minimum hip flexion torque, normalised to subject mass.

Three of these metrics (SW, HK and HT) were first introduced in Chapter 4, while the SR and GR metrics are first introduced here.

6.5.4 Closing Remarks

In this chapter, we have presented a framework for optimising exoskeleton control strategies based on a combination of musculoskeletal modelling and

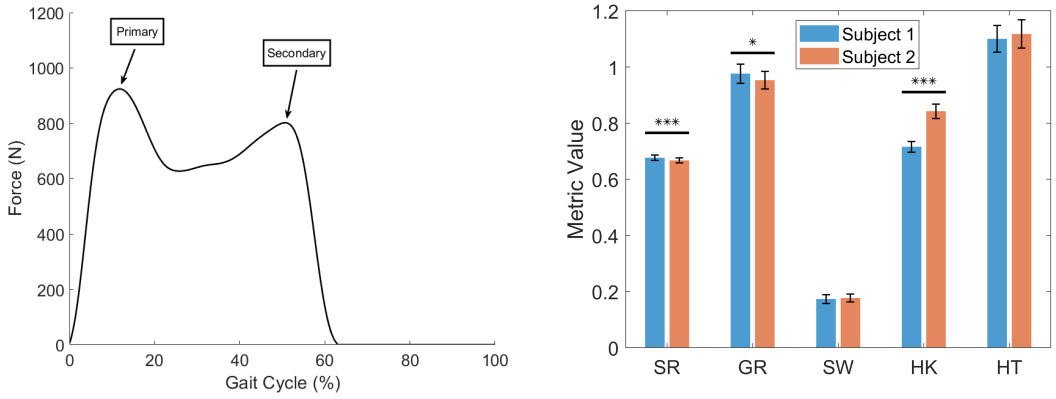

(a) (b)

Figure 6.9: **(a)** An example trajectory of vertical ground reaction force of the leading foot over a gait cycle. The locations of the primary and secondary force peaks used in the calculation of the GRF peak ratio gait metric are shown. **(b)** Comparison of a range of gait metrics between Subject 1 & Subject 2. Metrics include stance ratio (SR), GRF peak ratio (GR), step width (SW), hip range of motion (HK), normalised peak to peak hip torques (HT). Asterisks denote a p-value of 0.001 and 0.05 for 3 asterisks and 1 asterisk, respectively.

human-in-the-loop optimisation. Our method can outperform generic controllers while requiring less time investment than recent state-of-the-art HIL optimisation methods. This is critical if these approaches are to be used for those with injuries or gait pathologies, where long experimental protocols are not an option, and so that increasingly complex control parameterisations can be investigated. Our method could also be useful for labs with motion analysis equipment and experience in musculoskeletal modelling, but without the ability to measure metabolic rate via calorimetry.

The results presented here further highlight the sensitivity of exoskeleton assistance strategies to differences between subjects, be they resulting from physical differences in height or limb length (for example), or variation in internal locomotion strategies. Even off-the-shelf control schemes which have previously exhibited strong performance on the group-level were detrimental to the walking efficiency of some of our subjects. This highlights the need to identify personalised control strategies which work well on an individual level - indeed, this is the primary strength of pure human-in-the-loop approaches. This need is, again, even more pertinent for those with gait pathologies, whose

Formulation Update

In this chapter, and the one preceding it, we have seen the importance of personalising exoskeleton control & design parameters to suit an individuals proportions and gait patterns. Much like gait can be considered a term describing the unique walking style of an individual [97], a relationship is needed which describes how a persons underlying walking style (or gait) is affected by exoskeleton assistance on a neuromuscular level. As a starting point, we posit the following relationship:

$$\boldsymbol{\nu} = \boldsymbol{\nu}_0 + \mathbf{I}(\boldsymbol{\tau}_e), \tag{6.19}$$

In other words, the human muscle excitations $\boldsymbol{\nu}$ are composed of a baseline excitation $\boldsymbol{\nu}_0$, which the subject would command if wearing the exoskeleton transparently but experiencing no assistance, in combination with a reactionary component $\mathbf{I}(\boldsymbol{\tau}_e)$, representing a change in the humans neuromuscular control strategy instigated by the presence of active exoskeleton assistance. This relationship represents an additional constraint which must be considered in the optimisation-based exoskeleton control formulation. A notable exception arises when considering patients with partial or full paralysis, where instead we may require constraints on $\boldsymbol{\nu}$ for the set of affected muscles. Some further remarks are made on this case in the following chapter.

In some sense, the human-in-the-loop protocols presented in Chapters 5 and 6 bypass the need to learn the interaction model $\mathbf{I}$ by sampling from the control (or design) parameter space online. However, as we will discuss in the concluding chapter, the human-in-the-loop framework does not necessarily scale well to changes in walking context which are common in daily life.

walking patterns are likely to be further removed from the normal trajectories on which many generic assistance controllers are based.

Further work remains to be done on the combined approach of musculoskeletal modelling and human-in-the-loop optimisation, particularly to improve the accuracy of modelling human-exoskeleton interaction forces, and to explore alternate search strategies. However, the intersection of these fields has a great potential benefit for the growing community of people who benefit from assistive robotic devices.

Chapter 7

Conclusion

This thesis has been concerned with the effective design and control of exoskeletons, and other assistive robotic devices, for movement assistance. In Chapter 1, we identified three challenging aspects of exoskeleton-assisted locomotion which are required to be solved before the true potential of exoskeletons as assistive tools can be realised.

Firstly, we identified the need for modelling approaches which effectively capture the dynamic interaction between humans and exoskeletons. Then, in Chapter 3, we introduced techniques for modelling human-exoskeleton systems as a combination of musculoskeletal models, exoskeleton inertial properties, and constraint forces. A concrete example of a human-exoskeleton model was detailed in full, namely the human-APO model, which was then used and

referred to extensively in later chapters. In addition, we presented an analysis of methods for modelling the interaction forces acting at human-exoskeleton interfaces. This investigation relied heavily on the collection and processing of data via experimental gait analysis, which was introduced and discussed in detail in Chapter 2.

Next was the open question of which metrics, or objective functions, are suitable to optimise assistance strategies. In Chapter 4 the concept of a gait metric was introduced, and an attempt was made to formalise two key features of gait metrics: resolution and invariance. A study was presented which analysed the invariance properties of a range of gait metrics in order to identify those which are most closely linked to the underlying optimisation of gait stability. From this analysis, we identified two metrics in particular — medial-lateral centre of pressure displacement and medial-lateral margin of stability — which exhibited the most desirable invariance properties, and incorporated those metrics in to our optimisation formulation.

Finally, the third challenge we identified was the problem of shared control, and how to predict or otherwise control for unforeseen changes in human neuromuscular strategies due to the presence of external assistive forces. We saw how human-in-the-loop optimisation techniques, by sampling directly from subjects while learning optimal control (or design) parameters, can implicitly account for this phenomenon. Two applications of this technique were presented. The first application used human-in-the-loop methods to optimise the design parameters of a full body exoskeleton, showing that parameters like cuff placement can have a significant effect on performance. The second application explored how combining musculoskeletal modelling and human-in-the-loop optimisation can reduce the time investment required to complete the optimisation process, and thus enable more complex assistance strategies to be explored.

These three contributions represent a step in the right direction towards enabling exoskeletons and active prosthetics to be more widely used in real-world scenarios, which would lead to invaluable increases in quality of life for many. In the final forthcoming sections, a consolidated view of the optimisation based formulation for exoskeleton control is presented for completeness. Then, we discuss potential sources of further research.

7.1 Optimisation-based Control of Exoskeletons

In Chapter 1, a simple optimisation problem was introduced to model a human following some kinematic trajectory. This oversimplified problem represented the starting point for an optimisation-based exoskeleton control formulation. Throughout this thesis, this optimisation has been amended in a series of formulation updates, first accounting for human-exoskeleton dynamics and musculoskeletal modelling (p51), then identifying suitable metrics for the objective function (p71), and finally discussing the influence of shared control (p111). The resulting formulation is presented below.

For a set of gait metrics[26] $\mathcal{M}$ and a corresponding weight set W, exoskeleton motor torques $\boldsymbol{\mu}$ are selected according to the following optimisation:

$$\min_{\boldsymbol{\mu}} \sum_{1}^{k} w_i m_i \,, \tag{7.1}$$

$$M_c(\mathbf{q})\ddot{\mathbf{q}} + \mathbf{c}_c(\mathbf{q},\dot{\mathbf{q}}) + \mathbf{g}_c(\mathbf{q}) = \boldsymbol{\tau}_h + \boldsymbol{\tau}_g + \boldsymbol{\tau}_e \,, \tag{7.2}$$

$$\boldsymbol{\tau}_e = \mathbf{E}(\boldsymbol{\mu}) \,, \tag{7.3}$$

$$\boldsymbol{\tau}_h = \mathbf{F}\left(\mathbf{f_0}, \mathbf{l}, \dot{\mathbf{l}}\right)^{\mathsf{T}} R(\mathbf{q})\,\mathbf{a} \,, \tag{7.4}$$

$$\dot{\boldsymbol{l}} = \mathbf{C}(\mathbf{a}, \mathbf{l}, \mathbf{q}, \dot{\mathbf{q}}) \,, \tag{7.5}$$

$$\dot{\boldsymbol{a}} = \mathbf{A}(\mathbf{a}, \boldsymbol{\nu}) \,, \tag{7.6}$$

$$\boldsymbol{\nu} = \boldsymbol{\nu}_0 + \mathbf{I}(\boldsymbol{\tau}_e) \,, \tag{7.7}$$

$$\boldsymbol{\mu} \leq \boldsymbol{\mu}_{\max} \,, \tag{7.8}$$

$$\boldsymbol{\nu}_{\min} \leq \boldsymbol{\nu} \leq \boldsymbol{\nu}_{\max} \,. \tag{7.9}$$

For completeness, we summarise here the constituent elements of this system of equations. Equations 7.2 and 7.3 are the equations of human-exoskeleton dynamics, where **E** represents a specific human-exoskeleton force model (see Chapter 3). Equations 7.4 - 7.6 are the equations of musculoskeletal dynamics, modified to include the reactionary component to human muscle activation discussed in the formulation update of Chapter 6 (p111). As noted in the formulation update in Chapter 4 (p51), the elements of the gait metric set which comprise the objective function (Equation (7.1)) will vary depending on

[26] See Definition 4.4.

the task at hand. In this thesis, those metrics which optimise gait stability are preferred. Finally, Equations 7.8 and 7.9 encode the control limitations on the exoskeleton motor torques and human muscle activations, respectively.

A source of immediate further work following on from this thesis is to research methods for modelling or learning the function $\mathbf{I}$, which is necessary to compute the reactionary component of human muscle excitation in Equation (7.6), so that this optimisation formulation can be further tested both in simulation and the lab.

7.2 Future Research Directions

In this thesis we have seen evidence of the complexity of exoskeleton-assisted locomotion. Though the solutions to problems presented within this thesis represent a step in the right direction, the exoskeleton control problem is by no means solved. As is common in science, the answers to some questions often raise others. Here, a number of these questions are discussed in the form of potential extensions to this work.

The Shared Control Problem

In this thesis, we have used human-in-the-loop optimisation strategies to essentially circumvent the shared control problem — learning directly from motion data collected from the subject, rather than having to construct an explicit walking style model (as in Equation (7.6)). The human-in-the-loop approach has had strong metabolic results [99], but is not without drawbacks.

One notable drawback is the specificity of human-in-the-loop optimisation solutions to a particular set of experimental conditions. Recall the equation from Chapter 6 relating exoskeleton control parameters and metabolic rate:

$$V = f_s^C(\mathbf{p}). \tag{7.10}$$

Here, the subscript s denotes specificity to a particular subject, while C denotes specificity to the walking context in which the optimisation was performed. If a human-in-the-loop optimisation is performed for flat walking, there is no guarantee that the learned control policy will translate to other walking

contexts, for example walking on inclined terrain. Given that human-in-the-loop optimisation protocols involve collecting upwards of 60 minutes of motion data per participant per context, it quickly becomes infeasible to account for the natural changes in walking speed and incline which occur throughout daily life.

One source of future work is to investigate alternatives to human-in-the-loop optimisation that scale better to variations in walking context. One suggestion is to make use of bi-level optimisation techniques, similar to those which have been applied in dyadic collaboration tasks [149], and optimise exoskeleton assistance based on an internal optimal control simulations of human walking style changes [150].

Modelling Pathological Gait

Throughout this thesis, we have constructed an optimisation-based formulation of exoskeleton-assisted locomotion. We have thus far allowed for variation of walking style in the form of differing objective functions and human-exoskeleton interaction models which are, to some degree, subject-specific. However, we did not allow for variations in motor control strategies that can result from the presence of gait pathologies.

Human locomotion is a complex process comprising of the recruitment and cooperation of a huge number of musculotendon units. Pathological gait occurs when this process is somehow impeded. Disruptions can broadly be characterised as *musculoskeletal* or *neurological* in nature [151]. In the former, issues occur due to injuries or structural deformities in the body which interfere with the free and painless movement of the affected limbs; while in the latter, the normal action of the central nervous system, peripheral nerves, or muscles is inhibited.

As a starting point for investigating neuromuscular pathologies, two modelling strategies could be investigated:

1. Limiting maximum isometric force.
2. Limiting muscle activation levels.

A limit on maximum isometric force can readily be introduced directly to an OpenSim model by modifying the corresponding muscle parameter. Mean-

while, a limit on muscle activation could be introduced to the optimisation formulation given in Section 7.1 via a modification to the human activation constraint like so:

$$\boldsymbol{\nu}_{\min} \leq \boldsymbol{\nu} \leq \boldsymbol{\nu}_p \,, \tag{7.11}$$

where $\boldsymbol{\nu}_p < \boldsymbol{\nu}_{\max}$. A source of future work is to collect data from patients with gait pathologies so that the modelling approaches outlined above can be evaluated quantitatively.

Bibliography

[1] A. M. Dollar and H. Herr, "Lower extremity exoskeletons and active orthoses: challenges and state-of-the-art," *IEEE Transactions on robotics*, vol. 24, no. 1, pp. 144–158, 2008.

[2] T. Yan, M. Cempini, C. M. Oddo, and N. Vitiello, "Review of assistive strategies in powered lower-limb orthoses and exoskeletons," *Robotics and Autonomous Systems*, vol. 64, pp. 120–136, 2015.

[3] S. Jezernik, G. Colombo, T. Keller, H. Frueh, and M. Morari, "Robotic orthosis lokomat: A rehabilitation and research tool," *Neuromodulation: Technology at the neural interface*, vol. 6, no. 2, pp. 108–115, 2003.

[4] K. Y. Nam, H. J. Kim, B. S. Kwon, J.-W. Park, H. J. Lee, and A. Yoo, "Robot-assisted gait training (lokomat) improves walking function and activity in people with spinal cord injury: a systematic review," *Journal of neuroengineering and rehabilitation*, vol. 14, no. 1, p. 24, 2017.

[5] M. P. De Looze, T. Bosch, F. Krause, K. S. Stadler, and L. W. O'Sullivan, "Exoskeletons for industrial application and their potential effects on physical work load," *Ergonomics*, vol. 59, no. 5, pp. 671–681, 2016.

[6] S. H. Collins, M. B. Wiggin, and G. S. Sawicki, "Reducing the energy cost of human walking using an unpowered exoskeleton," *Nature*, vol. 522, no. 7555, p. 212, 2015.

[7] M. Windrich, M. Grimmer, O. Christ, S. Rinderknecht, and P. Beckerle, "Active lower limb prosthetics: a systematic review of design issues and solutions," *Biomedical engineering online*, vol. 15, no. 3, p. 140, 2016.

[8] F. Heremans, S. Vijayakumar, M. Bouri, B. Dehez, and R. Ronsse, "Bio-inspired design and validation of the efficient lockable spring ankle (elsa) prosthesis," in *2019 IEEE 16th International Conference on Rehabilitation Robotics (ICORR)*. IEEE, 2019, pp. 411–416.

[9] F. A. Panizzolo, I. Galiana, A. T. Asbeck, C. Siviy, K. Schmidt, K. G. Holt, and C. J. Walsh, "A biologically-inspired multi-joint soft exosuit that can reduce the energy cost of loaded walking," *Journal of neuroengineering and rehabilitation*, vol. 13, no. 1, p. 43, 2016.

[10] B. Quinlivan, S. Lee, P. Malcolm, D. Rossi, M. Grimmer, C. Siviy, N. Karavas, D. Wagner, A. Asbeck, I. Galiana *et al.*, "Assistance magnitude versus meta-

bolic cost reductions for a tethered multiarticular soft exosuit," *Science Robotics*, vol. 2, no. 2, p. eaah4416, 2017.

[11] J. Wolff, C. Parker, J. Borisoff, W. B. Mortenson, and J. Mattie, "A survey of stakeholder perspectives on exoskeleton technology," *J Neuroeng Rehabil*, vol. 11, Dec. 2014. [Online]. Available: http://www.ncbi.nlm.nih.gov/pmc/articles/PMC4320449/

[12] D. F. Gordon, G. Henderson, and S. Vijayakumar, "Effectively quantifying the performance of lower-limb exoskeletons over a range of walking conditions," *Frontiers in Robotics and AI*, vol. 5, p. 61, 2018.

[13] A. J. Young, J. Foss, H. Gannon, and D. P. Ferris, "Influence of power delivery timing on the energetics and biomechanics of humans wearing a hip exoskeleton," *Frontiers in bioengineering and biotechnology*, vol. 5, p. 4, 2017.

[14] A. D. Kuo and J. M. Donelan, "Dynamic principles of gait and their clinical implications," *Physical therapy*, vol. 90, no. 2, pp. 157–174, 2010.

[15] D. P. Ferris and C. L. Lewis, "Robotic Lower Limb Exoskeletons Using Proportional Myoelectric Control," *Conf Proc IEEE Eng Med Biol Soc*, vol. 2009, pp. 2119–2124, 2009. [Online]. Available: http://www.ncbi.nlm.nih.gov/pmc/articles/PMC2833282/

[16] J. R. Koller, D. A. Jacobs, D. P. Ferris, and C. D. Remy, "Learning to walk with an adaptive gain proportional myoelectric controller for a robotic ankle exoskeleton," *Journal of neuroengineering and rehabilitation*, vol. 12, no. 1, pp. 1–14, 2015.

[17] J. Zhang, P. Fiers, K. A. Witte, R. W. Jackson, K. L. Poggensee, C. G. Atkeson, and S. H. Collins, "Human-in-the-loop optimization of exoskeleton assistance during walking," *Science*, vol. 356, no. 6344, pp. 1280–1284, 2017.

[18] J. Nocedal and S. Wright, *Numerical optimization*. Springer Science & Business Media, 2006.

[19] R. Featherstone, *Rigid Body Dynamics Algorithms*. Springer, Nov. 2014, google-Books-ID: GJRGBQAAQBAJ.

[20] F. Sylos-Labini, V. La Scaleia, A. d'Avella, I. Pisotta, F. Tamburella, G. Scivoletto, M. Molinari, S. Wang, L. Wang, E. van Asseldonk *et al.*, "Emg patterns during assisted walking in the exoskeleton," *Frontiers in human neuroscience*, vol. 8, p. 423, 2014.

[21] R. J. Farris, H. A. Quintero, S. A. Murray, K. H. Ha, C. Hartigan, and M. Goldfarb, "A preliminary assessment of legged mobility provided by a lower limb exoskeleton for persons with paraplegia," *IEEE Transactions on neural systems*

and rehabilitation engineering, vol. 22, no. 3, pp. 482–490, 2013.

[22] D. Sanz-Merodio, M. Cestari, J. C. Arevalo, and E. Garcia, "A lower-limb exoskeleton for gait assistance in quadriplegia," in *2012 IEEE International Conference on Robotics and Biomimetics (ROBIO)*. IEEE, 2012, pp. 122–127.

[23] F. Doyle, "The historical development of analytical photogrammetry," *Photogrammetric Engineering*, vol. 30, no. 2, pp. 259–265, 1964.

[24] B. Bratt, *Rotoscoping: Techniques and tools for the Aspiring Artist*. Taylor & Francis, 2011.

[25] D. H. Sutherland, "The evolution of clinical gait analysis: Part ii kinematics," *Gait & posture*, vol. 16, no. 2, pp. 159–179, 2002.

[26] D. Fitzgerald, J. Foody, D. Kelly, T. Ward, C. Markham, J. McDonald, and B. Caulfield, "Development of a wearable motion capture suit and virtual reality biofeedback system for the instruction and analysis of sports rehabilitation exercises," in *2007 29th Annual International Conference of the IEEE Engineering in Medicine and Biology Society*. IEEE, 2007, pp. 4870–4874.

[27] A. Menache, *Understanding motion capture for computer animation and video games*. Morgan kaufmann, 2000.

[28] G. Guerra-Filho, "Optical motion capture: Theory and implementation." *RITA*, vol. 12, no. 2, pp. 61–90, 2005.

[29] M. Kitagawa and B. Windsor, *MoCap for artists: workflow and techniques for motion capture*. CRC Press, 2012.

[30] H. Kainz, L. Modenese, D. Lloyd, S. Maine, H. Walsh, and C. Carty, "Joint kinematic calculation based on clinical direct kinematic versus inverse kinematic gait models," *Journal of biomechanics*, vol. 49, no. 9, pp. 1658–1669, 2016.

[31] N. Hasler, B. Rosenhahn, T. Thormahlen, M. Wand, J. Gall, and H.-P. Seidel, "Markerless motion capture with unsynchronized moving cameras," in *2009 IEEE Conference on Computer Vision and Pattern Recognition*. IEEE, 2009, pp. 224–231.

[32] E. van der Kruk and M. M. Reijne, "Accuracy of human motion capture systems for sport applications; state-of-the-art review," *European journal of sport science*, vol. 18, no. 6, pp. 806–819, 2018.

[33] M. A. Perrott, T. Pizzari, J. Cook, and J. A. McClelland, "Comparison of lower limb and trunk kinematics between markerless and marker-based motion capture systems," *Gait & posture*, vol. 52, pp. 57–61, 2017.

[34] A. Pfister, A. M. West, S. Bronner, and J. A. Noah, "Comparative abilities of microsoft kinect and vicon 3d motion capture for gait analysis," *Journal of medical*

engineering & technology, vol. 38, no. 5, pp. 274–280, 2014.

[35] D. Roetenberg, H. Luinge, and P. Slycke, "Xsens mvn: Full 6dof human motion tracking using miniature inertial sensors," *Xsens Motion Technologies BV, Tech. Rep*, vol. 1, 2009.

[36] G. Henderson, D. Gordon, and S. Vijayakumar, "Identifying invariant gait metrics for exoskeleton assistance," in *2017 IEEE International Conference on Robotics and Biomimetics (ROBIO)*. IEEE, 2017, pp. 520–526.

[37] H. Kainz, D. Graham, J. Edwards, H. P. Walsh, S. Maine, R. N. Boyd, D. G. Lloyd, L. Modenese, and C. P. Carty, "Reliability of four models for clinical gait analysis," *Gait & posture*, vol. 54, pp. 325–331, 2017.

[38] S. L. Delp, J. P. Loan, M. G. Hoy, F. E. Zajac, E. L. Topp, and J. M. Rosen, "An interactive graphics-based model of the lower extremity to study orthopaedic surgical procedures," *IEEE Transactions on Biomedical engineering*, vol. 37, no. 8, pp. 757–767, 1990.

[39] Vicon, "What gap filling algorithms are used in nexus 2?" 2020, https://www.vicon.com/support/faqs/?q=what-gap-filling-algorithms-are-used-nexus-2.

[40] S. L. Delp, F. C. Anderson, A. S. Arnold, P. Loan, A. Habib, C. T. John, E. Guendelman, and D. G. Thelen, "Opensim: open-source software to create and analyze dynamic simulations of movement," *IEEE transactions on biomedical engineering*, vol. 54, no. 11, pp. 1940–1950, 2007.

[41] M. B. Popovic, *Biomechatronics*. Academic Press, 2019, pp. 99–100.

[42] B. Corporation, "Bertec force plates," 2012, https://www.bertec.com/downloads.

[43] Kistler, "Force plates and accessories," 2019, https://www.kistler.com/?type=669&fid=350&model=download.

[44] K. Nakazato, P. Scheiber, and E. Müller, "A comparison of ground reaction forces determined by portable force-plate and pressure-insole systems in alpine skiing," *Journal of sports science & medicine*, vol. 10, no. 4, p. 754, 2011.

[45] P. S. Dyer and S. J. M. Bamberg, "Instrumented insole vs. force plate: A comparison of center of plantar pressure," in *2011 Annual International Conference of the IEEE Engineering in Medicine and Biology Society*. IEEE, 2011, pp. 6805–6809.

[46] D. C. Low and S. Dixon, "Footscan pressure insoles: accuracy and reliability of force and pressure measurements in running," *Gait & posture*, vol. 32, no. 4, pp. 664–666, 2010.

[47] G. L. Soderberg and T. M. Cook, "Electromyography in biomechanics," *Physical Therapy*, vol. 64, no. 12, pp. 1813–1820, 1984.

[48] D. Winter and H. Yack, "Emg profiles during normal human walking: stride-to-stride and inter-subject variability," *Electroencephalography and clinical neurophysiology*, vol. 67, no. 5, pp. 402–411, 1987.

[49] M. G. Gazendam and A. L. Hof, "Averaged emg profiles in jogging and running at different speeds," *Gait & posture*, vol. 25, no. 4, pp. 604–614, 2007.

[50] A. Mero and P. V. Komi, "Force-, emg-, and elasticity-velocity relationships at submaximal, maximal and supramaximal running speeds in sprinters," *European journal of applied physiology and occupational physiology*, vol. 55, no. 5, pp. 553–561, 1986.

[51] A. Krasoulis, I. Kyranou, M. S. Erden, K. Nazarpour, and S. Vijayakumar, "Improved prosthetic hand control with concurrent use of myoelectric and inertial measurements," *Journal of neuroengineering and rehabilitation*, vol. 14, no. 1, p. 71, 2017.

[52] L. Peternel, T. Noda, T. Petrič, A. Ude, J. Morimoto, and J. Babič, "Adaptive control of exoskeleton robots for periodic assistive behaviours based on emg feedback minimisation," *PloS one*, vol. 11, no. 2, p. e0148942, 2016.

[53] N. Amrutha and V. Arul, "A review on noises in emg signal and its removal," *Int. J. Sci. Res. Publ*, vol. 7, no. 5, pp. 23–27, 2017.

[54] W. Rose, "Electromyogram analysis," *Online course material. University of Delaware. Retrieved July*, vol. 5, p. 2016, 2011.

[55] R. Merletti and P. Di Torino, "Standards for reporting emg data," *J Electromyogr Kinesiol*, vol. 9, no. 1, pp. 3–4, 1999.

[56] J. Brockway, "Derivation of formulae used to calculate energy expenditure in man." *Human nutrition. Clinical nutrition*, vol. 41, no. 6, pp. 463–471, 1987.

[57] J. McLean, J. A. MacLean, G. Tobin, and J. McLean, *Animal and human calorimetry*. Cambridge University Press, 1987.

[58] D. J. Macfarlane, "Open-circuit respirometry: a historical review of portable gas analysis systems," *European journal of applied physiology*, vol. 117, no. 12, pp. 2369–2386, 2017.

[59] M. Kim, Y. Ding, P. Malcolm, J. Speeckaert, C. J. Siviy, C. J. Walsh, and S. Kuindersma, "Human-in-the-loop bayesian optimization of wearable device parameters," *PloS one*, vol. 12, no. 9, p. e0184054, 2017.

[60] J. C. Selinger and J. M. Donelan, "Estimating instantaneous energetic cost during non-steady-state gait," *Journal of Applied Physiology*, vol. 117, no. 11, pp.

1406–1415, 2014.

[61] L. M. Mooney, E. J. Rouse, and H. M. Herr, "Autonomous exoskeleton reduces metabolic cost of human walking during load carriage," *Journal of neuroengineering and rehabilitation*, vol. 11, no. 1, p. 80, 2014.

[62] O. S. Mian, J. M. Thom, L. P. Ardigò, M. V. Narici, and A. E. Minetti, "Metabolic cost, mechanical work, and efficiency during walking in young and older men," *Acta physiologica*, vol. 186, no. 2, pp. 127–139, 2006.

[63] F. Giovacchini, F. Vannetti, M. Fantozzi, M. Cempini, M. Cortese, A. Parri, T. Yan, D. Lefeber, and N. Vitiello, "A light-weight active orthosis for hip movement assistance," *Robotics and Autonomous Systems*, vol. 73, pp. 123–134, 2015.

[64] E. Martini, C. B. Sanz-Morere, C. Livolsi, A. Pergolini, G. Arnetoli, S. Doronzio, A. Giffone, R. Conti, F. Giovacchini, Þ. Friðriksson *et al.*, "Lower-limb amputees can reduce the energy cost of walking when assisted by an active pelvis orthosis," in *2020 8th IEEE RAS/EMBS International Conference for Biomedical Robotics and Biomechatronics (BioRob)*. IEEE, 2020, pp. 809–815.

[65] E. Martini, S. Crea, A. Parri, L. Bastiani, U. Faraguna, Z. McKinney, R. Molino-Lova, L. Pratali, and N. Vitiello, "Gait training using a robotic hip exoskeleton improves metabolic gait efficiency in the elderly," *Scientific reports*, vol. 9, no. 1, pp. 1–12, 2019.

[66] R. Ronsse, T. Lenzi, N. Vitiello, B. Koopman, E. Van Asseldonk, S. M. M. De Rossi, J. Van Den Kieboom, H. Van Der Kooij, M. C. Carrozza, and A. J. Ijspeert, "Oscillator-based assistance of cyclical movements: model-based and model-free approaches," *Medical & biological engineering & computing*, vol. 49, no. 10, p. 1173, 2011.

[67] S.-H. Hyon, T. Hayashi, A. Yagi, T. Noda, and J. Morimoto, "Design of hybrid drive exoskeleton robot xor2," in *2013 IEEE/RSJ International Conference on Intelligent Robots and Systems*. IEEE, 2013, pp. 4642–4648.

[68] S. L. Delp and J. P. Loan, "A computational framework for simulating and analyzing human and animal movement," *Computing in Science & Engineering*, vol. 2, no. 5, pp. 46–55, 2000.

[69] F. C. Anderson and M. G. Pandy, "A dynamic optimization solution for vertical jumping in three dimensions," *Computer methods in biomechanics and biomedical engineering*, vol. 2, no. 3, pp. 201–231, 1999.

[70] G. T. Yamaguchi and F. E. Zajac, "A planar model of the knee joint to characterize the knee extensor mechanism," *Journal of biomechanics*, vol. 22, no. 1, pp. 1–10, 1989.

[71] M. Millard, T. Uchida, A. Seth, and S. L. Delp, "Flexing computational muscle: modeling and simulation of musculotendon dynamics," *Journal of biomechanical engineering*, vol. 135, no. 2, 2013.

[72] D. G. Thelen, "Adjustment of muscle mechanics model parameters to simulate dynamic contractions in older adults," *Journal of biomechanical engineering*, vol. 125, no. 1, pp. 70–77, 2003.

[73] "Opensim documentation," https://simtk-confluence.stanford.edu /display/OpenSim/OpenSim+Documentation, Accessed: 29-01-21.

[74] O. Skalshøi, C. H. Iversen, D. B. Nielsen, J. Jacobsen, I. Mechlenburg, K. Søballe, and H. Sørensen, "Walking patterns and hip contact forces in patients with hip dysplasia," *Gait & posture*, vol. 42, no. 4, pp. 529–533, 2015.

[75] A. Rajagopal, C. L. Dembia, M. S. DeMers, D. D. Delp, J. L. Hicks, and S. L. Delp, "Full-body musculoskeletal model for muscle-driven simulation of human gait," *IEEE transactions on biomedical engineering*, vol. 63, no. 10, pp. 2068–2079, 2016.

[76] T. K. Uchida, A. Seth, S. Pouya, C. L. Dembia, J. L. Hicks, and S. L. Delp, "Simulating ideal assistive devices to reduce the metabolic cost of running," *PloS one*, vol. 11, no. 9, p. e0163417, 2016.

[77] N. Jarrassé and G. Morel, "Connecting a human limb to an exoskeleton," *IEEE Transactions on Robotics*, vol. 28, no. 3, pp. 697–709, 2012.

[78] M. Malosio, N. Pedrocchi, F. Vicentini, and L. M. Tosatti, "Analysis of elbow-joints misalignment in upper-limb exoskeleton," in *Rehabilitation Robotics (ICORR), 2011 IEEE International Conference on*. IEEE, 2011, pp. 1–6.

[79] D. Zanotto, Y. Akiyama, P. Stegall, and S. K. Agrawal, "Knee joint misalignment in exoskeletons for the lower extremities: Effects on user's gait," *IEEE Transactions on Robotics*, vol. 31, no. 4, pp. 978–987, 2015.

[80] A. Schiele and F. C. Van Der Helm, "Kinematic design to improve ergonomics in human machine interaction," *IEEE Transactions on Neural Systems and Rehabilitation Engineering*, vol. 14, no. 4, pp. 456–469, 2006.

[81] J. M. Hidler and A. E. Wall, "Alterations in muscle activation patterns during robotic-assisted walking," *Clinical Biomechanics*, vol. 20, no. 2, pp. 184–193, 2005.

[82] A. Schiele, "An explicit model to predict and interpret constraint force creation in phri with exoskeletons," in *Robotics and Automation, 2008. ICRA 2008. IEEE International Conference on*. IEEE, 2008, pp. 1324–1330.

[83] M. B. Yandell, B. T. Quinlivan, D. Popov, C. Walsh, and K. E. Zelik, "Physical

interface dynamics alter how robotic exosuits augment human movement: implications for optimizing wearable assistive devices," *Journal of neuroengineering and rehabilitation*, vol. 14, no. 1, p. 40, 2017.

[84] M. Harrington, A. Zavatsky, S. Lawson, Z. Yuan, and T. Theologis, "Prediction of the hip joint centre in adults, children, and patients with cerebral palsy based on magnetic resonance imaging," *Journal of biomechanics*, vol. 40, no. 3, pp. 595–602, 2007.

[85] V. T. Inman, H. D. Eberhart *et al.*, "The major determinants in normal and pathological gait," *JBJS*, vol. 35, no. 3, pp. 543–558, 1953.

[86] C. Kirtley, *Clinical gait analysis: theory and practice*. Elsevier Health Sciences, 2006.

[87] S. A. Gard and D. S. Childress, "What determines the vertical displacement of the body during normal walking?" *JPO: Journal of Prosthetics and Orthotics*, vol. 13, no. 3, pp. 64–67, 2001.

[88] M. H. Schwartz and A. Rozumalski, "The gait deviation index: a new comprehensive index of gait pathology," *Gait & posture*, vol. 28, no. 3, pp. 351–357, 2008.

[89] R. Baker, J. L. McGinley, M. H. Schwartz, S. Beynon, A. Rozumalski, H. K. Graham, and O. Tirosh, "The gait profile score and movement analysis profile," *Gait & posture*, vol. 30, no. 3, pp. 265–269, 2009.

[90] D. D. Espy, F. Yang, T. Bhatt, and Y.-C. Pai, "Independent influence of gait speed and step length on stability and fall risk," *Gait & posture*, vol. 32, no. 3, pp. 378–382, 2010.

[91] J. O. JudgeRoy, B. Davis III, and S. Õunpuu, "Step length reductions in advanced age: the role of ankle and hip kinetics," *The Journals of Gerontology Series A: Biological Sciences and Medical Sciences*, vol. 51, no. 6, pp. M303–M312, 1996.

[92] T. M. Owings and M. D. Grabiner, "Step width variability, but not step length variability or step time variability, discriminates gait of healthy young and older adults during treadmill locomotion," *Journal of biomechanics*, vol. 37, no. 6, pp. 935–938, 2004.

[93] K. Kawamura, A. Tokuhiro, and H. Takechi, "Gait analysis of slope walking: a study on step length, stride width, time factors and deviation in the center of pressure." *Acta Medica Okayama*, vol. 45, no. 3, pp. 179–184, 1991.

[94] A. Leroux, J. Fung, and H. Barbeau, "Postural adaptation to walking on inclined surfaces: I. normal strategies," *Gait & posture*, vol. 15, no. 1, pp. 64–74, 2002.

[95] R. C. Sheehan and J. S. Gottschall, "At similar angles, slope walking has a

greater fall risk than stair walking," *Applied ergonomics*, vol. 43, no. 3, pp. 473–478, 2012.

[96] T. K. Uchida and S. L. Delp, *Biomechanics of Movement: The Science of Sports, Robotics, and Rehabilitation*. MIT Press, 2021.

[97] M. W. Whittle, *Gait analysis: an introduction*. Butterworth-Heinemann, 2014.

[98] S. A. Dugan and K. P. Bhat, "Biomechanics and analysis of running gait," *Physical Medicine and Rehabilitation Clinics*, vol. 16, no. 3, pp. 603–621, 2005.

[99] Y. Ding, M. Kim, S. Kuindersma, and C. J. Walsh, "Human-in-the-loop optimization of hip assistance with a soft exosuit during walking," *Science Robotics*, vol. 3, no. 15, p. eaar5438, 2018.

[100] R. Riener, L. Lünenburger, I. Maier, G. Colombo, and V. Dietz, "Locomotor training in subjects with sensori-motor deficits: an overview of the robotic gait orthosis lokomat," *Journal of Healthcare Engineering*, vol. 1, no. 2, pp. 197–216, 2010. [Online]. Available: http://multi-science.atypon.com/doi/abs/10.1260/2040-2295.1.2.197

[101] J. A. Blaya and H. Herr, "Adaptive control of a variable-impedance ankle-foot orthosis to assist drop-foot gait," *IEEE Trans Neural Syst Rehabil Eng*, vol. 12, no. 1, pp. 24–31, Mar. 2004.

[102] D. A. Winter, "Kinematic and kinetic patterns in human gait: Variability and compensating effects," *Human Movement Science*, vol. 3, no. 1–2, pp. 51–76, Mar. 1984. [Online]. Available: http://www.sciencedirect.com/science/article/pii/0167945784900058

[103] B. W. Stansfield, S. J. Hillman, M. E. Hazlewood, A. A. Lawson, A. M. Mann, I. R. Loudon, and J. E. Robb, "Sagittal joint kinematics, moments, and powers are predominantly characterized by speed of progression, not age, in normal children," *J Pediatr Orthop*, vol. 21, no. 3, pp. 403–411, Jun. 2001.

[104] M. S. Orendurff, A. D. Segal, G. K. Klute, J. S. Berge, E. S. Rohr, and N. J. Kadel, "The effect of walking speed on center of mass displacement," *J Rehabil Res Dev*, vol. 41, no. 6A, pp. 829–834, Dec. 2004.

[105] A. N. Lay, C. J. Hass, and R. J. Gregor, "The effects of sloped surfaces on locomotion: A kinematic and kinetic analysis," *Journal of Biomechanics*, vol. 39, no. 9, pp. 1621–1628, 2006. [Online]. Available: http://www.sciencedirect.com/science/article/pii/S0021929005002150

[106] J. R. Franz and R. Kram, "The Effects of Grade and Speed on Leg Muscle Activations during Walking," *Gait Posture*, vol. 35, no. 1, pp. 143–147, Jan. 2012. [Online]. Available: http://www.ncbi.nlm.nih.gov/pmc/articles/

PMC3262943/

[107] T. Lenzi, D. Zanotto, P. Stegall, M. C. Carrozza, and S. K. Agrawal, "Reducing muscle effort in walking through powered exoskeletons," *Conf Proc IEEE Eng Med Biol Soc*, vol. 2012, pp. 3926–3929, 2012.

[108] D. Martelli, F. Vannetti, M. Cortese, P. Tropea, F. Giovacchini, S. Micera, V. Monaco, and N. Vitiello, "The effects on biomechanics of walking and balance recovery in a novel pelvis exoskeleton during zero-torque control," *Robotica*, vol. 32, no. 08, pp. 1317–1330, 2014.

[109] C. L. Lewis and D. P. Ferris, "Invariant hip moment pattern while walking with a robotic hip exoskeleton," *J Biomech*, vol. 44, no. 5, pp. 789–793, Mar. 2011. [Online]. Available: http://www.ncbi.nlm.nih.gov/pmc/articles/PMC3075111/

[110] A. L. Hof, M. G. J. Gazendam, and W. E. Sinke, "The condition for dynamic stability," *Journal of Biomechanics*, vol. 38, no. 1, pp. 1–8, Jan. 2005.

[111] C. L. Vaughan and M. J. O'Malley, "Froude and the contribution of naval architecture to our understanding of bipedal locomotion," *Gait & posture*, vol. 21, no. 3, pp. 350–362, 2005.

[112] J. Cohen, "Statistical power analysis for the behavioural sciences," *Hillsdale, NJ, Lawrence Erlbaum Associates*, vol. 2nd ed., 1988.

[113] S. S. Sawilowsky, "New effect size rules of thumb," *Journal of Modern Applied Statistical Methods*, vol. 8, no. 2, pp. 597–599, 2009.

[114] N. d'Elia, F. Vanetti, M. Cempini, G. Pasquini, A. Parri, M. Rabuffetti, M. Ferrarin, R. Molino Lova, and N. Vitiello, "Physical human-robot interaction of an active pelvis orthosis: toward ergonomic assessment of wearable robots," *Journal of NeuroEngineering and Rehabilitation*, vol. 14, p. 29, 2017. [Online]. Available: http://dx.doi.org/10.1186/s12984-017-0237-y

[115] Z. Svoboda, L. Bizovska, M. Janura, E. Kubonova, and N. Vuillerme, "Variability of centre of pressure displacements during gait in fallers and nonfallers: A 6-month prospective study," *Gait & Posture*, vol. 49, p. 160, Sep. 2016. [Online]. Available: http://www.sciencedirect.com/science/article/pii/S0966636216303563

[116] F. Horst, S. Lapuschkin, W. Samek, K.-R. Müller, and W. I. Schöllhorn, "Explaining the unique nature of individual gait patterns with deep learning," *Scientific reports*, vol. 9, no. 1, pp. 1–13, 2019.

[117] T. W. Dorn, J. M. Wang, J. L. Hicks, and S. L. Delp, "Predictive simulation generates human adaptations during loaded and inclined walking," *PloS one*, vol. 10,

no. 4, p. e0121407, 2015.

[118] J. R. Koller, D. H. Gates, D. P. Ferris, and C. D. Remy, "'Body-in-the-Loop' optimization of assistive robotic devices: A validation study." in *Robotics: Science and Systems*, vol. 2016, 2016, pp. 1–10.

[119] W. Felt, J. C. Selinger, J. M. Donelan, and C. D. Remy, "'Body-In-The-Loop': Optimizing device parameters using measures of instantaneous energetic cost," *PloS one*, vol. 10, no. 8, p. e0135342, 2015.

[120] D. F. N. Gordon, T. Matsubara, T. Noda, T. Teramae, J. Morimoto, and S. Vijayakumar, "Bayesian optimisation of exoskeleton design parameters," in *2018 7th IEEE International Conference on Biomedical Robotics and Biomechatronics (Biorob)*. IEEE, 2018, pp. 653–658.

[121] M. Hamaya, T. Matsubara, T. Noda, T. Teramae, and J. Morimoto, "Learning assistive strategies for exoskeleton robots from user-robot physical interaction," *Pattern Recognition Letters*, vol. 99, pp. 67–76, 2017.

[122] M. Hamaya, T. Matsubara, J.-i. Furukawa, Y. Sun, S. Yagi, T. Teramae, T. Noda, and J. Morimoto, "Exploiting human and robot muscle synergies for human-in-the-loop optimization of emg-based assistive strategies," in *2019 International Conference on Robotics and Automation (ICRA)*. IEEE, 2019, pp. 549–555.

[123] J. Snoek, H. Larochelle, and R. P. Adams, "Practical bayesian optimization of machine learning algorithms," in *Advances in neural information processing systems*, 2012, pp. 2951–2959.

[124] C. Pechak, M. Thompson, G. H. E. Consortium *et al.*, "Disability and rehabilitation in developing countries," *Global Health Education Consortium*, 2007.

[125] R. Cardoso and M. T. Silva, "Design, analysis and simulation of a novel device for locomotion support," in *Converging Clinical and Engineering Research on Neurorehabilitation II*. Springer, 2017, pp. 833–837.

[126] L. Cui, A. Phan, and G. Allison, "Design and fabrication of a three dimensional printable non-assembly articulated hand exoskeleton for rehabilitation," in *2015 37th Annual International Conference of the IEEE Engineering in Medicine and Biology Society (EMBC)*. IEEE, 2015, pp. 4627–4630.

[127] T. Lenzi, M. C. Carrozza, and S. K. Agrawal, "Powered hip exoskeletons can reduce the user's hip and ankle muscle activations during walking," *IEEE Transactions on Neural Systems and Rehabilitation Engineering*, vol. 21, no. 6, pp. 938–948, 2013.

[128] P. Malcolm, W. Derave, S. Galle, and D. De Clercq, "A simple exoskeleton that assists plantarflexion can reduce the metabolic cost of human walking," *PloS*

one, vol. 8, no. 2, p. e56137, 2013.

[129] K. Seo, J. Lee, Y. Lee, T. Ha, and Y. Shim, "Fully autonomous hip exoskeleton saves metabolic cost of walking," in *2016 IEEE International Conference on Robotics and Automation (ICRA)*. IEEE, 2016, pp. 4628–4635.

[130] A. B. Zoss, H. Kazerooni, and A. Chu, "Biomechanical design of the berkeley lower extremity exoskeleton (bleex)," *IEEE/ASME Transactions on mechatronics*, vol. 11, no. 2, pp. 128–138, 2006.

[131] R. Suzman and J. Beard, "Global health and aging," *NIH Publ*, vol. 1, no. 4, pp. 273–277, 2011.

[132] R. Suzman, J. R. Beard, T. Boerma, and S. Chatterji, "Health in an ageing world—what do we know?" *The Lancet*, vol. 385, no. 9967, pp. 484–486, 2015.

[133] S. F. M. Chastin, E. Ferriolli, N. A. Stephens, K. C. Fearon, and C. Greig, "Relationship between sedentary behaviour, physical activity, muscle quality and body composition in healthy older adults," *Age and ageing*, vol. 41, no. 1, pp. 111–114, 2011.

[134] S. Galle, P. Malcolm, S. H. Collins, and D. De Clercq, "Reducing the metabolic cost of walking with an ankle exoskeleton: interaction between actuation timing and power," *Journal of neuroengineering and rehabilitation*, vol. 14, no. 1, p. 35, 2017.

[135] B. Quinlivan, S. Lee, P. Malcolm, D. Rossi, M. Grimmer, C. Siviy, N. Karavas, D. Wagner, A. Asbeck, I. Galiana *et al.*, "Assistance magnitude versus metabolic cost reductions for a tethered multiarticular soft exosuit," *Sci Robot*, vol. 2, no. 2, p. 4416, 2017.

[136] Y. Ding, F. A. Panizzolo, C. Siviy, P. Malcolm, I. Galiana, K. G. Holt, and C. J. Walsh, "Effect of timing of hip extension assistance during loaded walking with a soft exosuit," *Journal of neuroengineering and rehabilitation*, vol. 13, no. 1, p. 87, 2016.

[137] I. Kang, H. Hsu, and A. Young, "The effect of hip assistance levels on human energetic cost using robotic hip exoskeletons," *IEEE Robotics and Automation Letters*, vol. 4, no. 2, pp. 430–437, 2019.

[138] M. P. Murray, "Gait as a total pattern of movement: Including a bibliography on gait," *American Journal of Physical Medicine & Rehabilitation*, vol. 46, no. 1, pp. 290–333, 1967.

[139] M. P. Murray, A. B. Drought, and R. C. Kory, "Walking patterns of normal men," *JBJS*, vol. 46, no. 2, pp. 335–360, 1964.

[140] H. Westerblad, J. D. Bruton, and A. Katz, "Skeletal muscle: energy metabolism,

fiber types, fatigue and adaptability," *Experimental cell research*, vol. 316, no. 18, pp. 3093–3099, 2010.

[141] M. Kim, C. Liu, J. Kim, S. Lee, A. Meguid, C. J. Walsh, and S. Kuindersma, "Bayesian optimization of soft exosuits using a metabolic estimator stopping process," in *2019 International Conference on Robotics and Automation (ICRA)*. IEEE, 2019, pp. 9173–9179.

[142] P. Slade, R. Troutman, M. J. Kochenderfer, S. H. Collins, and S. L. Delp, "Rapid energy expenditure estimation for ankle assisted and inclined loaded walking," *Journal of neuroengineering and rehabilitation*, vol. 16, no. 1, p. 67, 2019.

[143] C. L. Dembia, A. Silder, T. K. Uchida, J. L. Hicks, and S. L. Delp, "Simulating ideal assistive devices to reduce the metabolic cost of walking with heavy loads," *PloS one*, vol. 12, no. 7, p. e0180320, 2017.

[144] F. C. Anderson and M. G. Pandy, "Dynamic optimization of human walking," *Journal of biomechanical engineering*, vol. 123, no. 5, pp. 381–390, 2001.

[145] B. R. Umberger, K. G. Gerritsen, and P. E. Martin, "A model of human muscle energy expenditure," *Computer methods in biomechanics and biomedical engineering*, vol. 6, no. 2, pp. 99–111, 2003.

[146] T. K. Uchida, J. L. Hicks, C. L. Dembia, and S. L. Delp, "Stretching your energetic budget: how tendon compliance affects the metabolic cost of running," *PloS one*, vol. 11, no. 3, p. e0150378, 2016.

[147] A. D. Koelewijn, D. Heinrich, and A. J. Van Den Bogert, "Metabolic cost calculations of gait using musculoskeletal energy models, a comparison study," *PloS one*, vol. 14, no. 9, 2019.

[148] D. A. Winter, "Biomechanical motor patterns in normal walking," *Journal of motor behavior*, vol. 15, no. 4, pp. 302–330, 1983.

[149] T. Stouraitis, I. Chatzinikolaidis, M. Gienger, and S. Vijayakumar, "Online hybrid motion planning for dyadic collaborative manipulation via bilevel optimization," *IEEE Transactions on Robotics*, vol. 36, no. 5, pp. 1452–1471, 2020.

[150] C. L. Dembia, N. A. Bianco, A. Falisse, J. L. Hicks, and S. L. Delp, "Opensim moco: musculoskeletal optimal control," *PLOS Computational Biology*, vol. 16, no. 12, p. e1008493, 2020.

[151] W. Pirker and R. Katzenschlager, "Gait disorders in adults and the elderly," *Wiener Klinische Wochenschrift*, vol. 129, no. 3-4, pp. 81–95, 2017.

[152] M. A. Sherman, A. Seth, and S. L. Delp, "Simbody: multibody dynamics for biomedical research," *Procedia Iutam*, vol. 2, pp. 241–261, 2011.

[153] D. G. Thelen and F. C. Anderson, "Using computed muscle control to gener-

ate forward dynamic simulations of human walking from experimental data," *Journal of biomechanics*, vol. 39, no. 6, pp. 1107–1115, 2006.

[154] T. Chand, "An algorithm for generating muscle-actuated simulations of long-duration movements," *bcats 2006*, p. 31, 2006.

[155] M. A. Sherman, A. Seth, and S. L. Delp, "What is a moment arm? calculating muscle effectiveness in biomechanical models using generalized coordinates," in *Proceedings of the... ASME Design Engineering Technical Conferences. ASME Design Engineering Technical Conferences*, vol. 2013. NIH Public Access, 2013.

[156] F. C. Anderson and M. G. Pandy, "Static and dynamic optimization solutions for gait are practically equivalent," *Journal of biomechanics*, vol. 34, no. 2, pp. 153–161, 2001.

[157] Y.-C. Lin, T. W. Dorn, A. G. Schache, and M. G. Pandy, "Comparison of different methods for estimating muscle forces in human movement," *Proceedings of the Institution of Mechanical Engineers, Part H: Journal of Engineering in Medicine*, vol. 226, no. 2, pp. 103–112, 2012.

Appendix A

Musculoskeletal Modelling

OpenSim is modelling software which allows users to create musculoskeletal models & analyse dynamic simulations of movement [40]. It is built on the multibody dynamics engine Simbody, which is aimed primarily at researchers in the field of biomechanics [152].

OpenSim includes a set of generic musculoskeletal models intended for a range of educational and scientific purposes. In this thesis, we focus on two widely used models which were specifically designed for the analysis of human gait, with a focus on lower-body physiology. These models, shown in Figure A.1, are known as the *gait2392* and *gait2354* models, being so named as they possess 23 degrees of freedom driven by 92 and 54 musculotendon actuators, respectively. The human-exoskeleton models described in Chapter 3

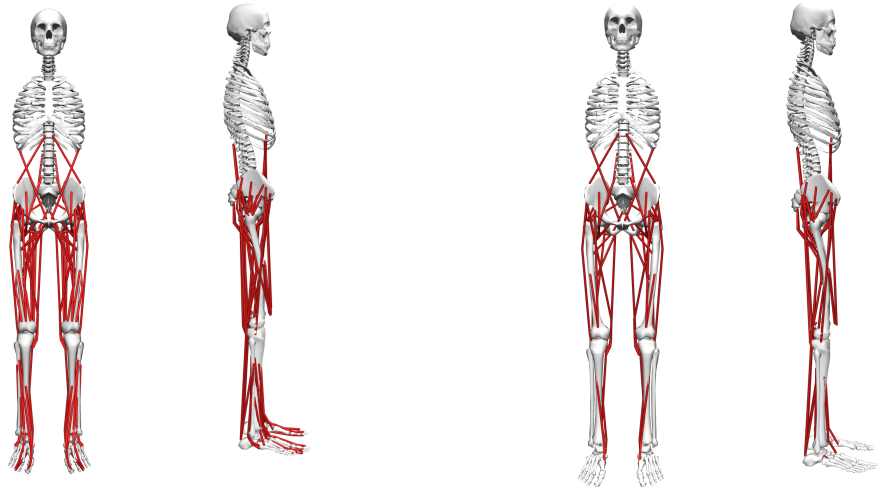

(a) (b)

Figure A.1: The (a) gait2392 and (b) gait2354 musculoskeletal models. The models are identical except that the gait2354 model features fewer muscles.

use these human models as a base.

The following sections will introduce and explain the computational tools OpenSim offers for running simulations of human motions. Note that these algorithms are included within OpenSim, and were not developed for this thesis, but are included as background information to aid understanding of the simulation steps outlined in Chapters 3, 4 and 6. The primary reference for the subsequent sections is the OpenSim User's guide [73]; for this Appendix only repeated citations to this source are avoided. Information taken from other sources is cited appropriately.

A.1 Scaling Musculoskeletal Models

The OpenSim scaling tool allows users match the mass and proportions of generic musculoskeletal models to specific subjects. The tool performs two steps as part of the scaling process, both of which involve comparisons between a set of experimental markers measured using motion capture data (for an example of an experimental marker set, see Section 2.1.1) and a set of virtual markers affixed to the generic model.

Firstly, a subset markers located at easy-to-locate anatomical landmarks such as the ankle bone is used to compute scaling factors between the virtual model and the model of the subject. These scaling factors are then used to scale the body segments of the model so that the distances between anatomical landmarks are the same on the virtual model and on the subject. In other words, this step ensures that the bodies comprising the virtual model are scaled to that of the subject. The mass of each body is also scaled accordingly by assuming that the mass distribution between bodies remains constant.

Secondly, the locations of the virtual markers are shifted to match the experimental marker locations. This step is less important for markers located at anatomical landmarks, which should already be fairly accurate, but is important for clusters of markers used to represent (for example) the thigh and shank which can have high variance in where they are located (between individual trials as well as between subjects).

A.2 Inverse Kinematics

Joint kinematics trajectories, $\mathbf{q}(t)$, are obtained from experimental data via least squares minimisation. The problem solved at each timestep is of the following form:

$$\min_{q} \sum_{i=1}^{m} w_i \|\mathbf{p}_i - \mathbf{x}_i(\mathbf{q})\|^2, \tag{A.1}$$

where $\mathbf{p}_i$ is the 3D position in space of the i^{th} experimental marker and $\mathbf{x}_i$ is the 3D position of the corresponding model marker, which is dependent on $\mathbf{q}$.

A.3 The Residual Reduction Algorithm

Due to a combination of model inaccuracies[27] and noisy data, OpenSim models are never perfectly dynamically consistent with the experimental data they aim to track. Essentially, this means the actuators of the model are incapable of tracking the desired motion and force data without the assistance of additional 6D forces applied to the root body. These additional forces are termed

[27] Model inaccuracies can result due to simplifications such as assuming a single torso segment or approximating the mass distribution for a subject.

residual forces.

The purpose of the Residual Reduction Algorithm (RRA) is to iteratively minimise this dynamic inconsistency by making adjustments to the model & the simulated kinematics. The lower the residual forces, the more any modelled motions are a result of internal joint torques rather than the residual forces. In other words, the lower the residual forces, the more accurately the OpenSim model is able to represent the experimental data.

The RRA algorithm is an improvement of the Residual Elimination Algorithm (REA) employed previously by Thelen & Anderson [153]. The REA algorithm aims to eliminate the residual forces completely by making changes to the joint accelerations. However, this has the negative effect of drift on the pelvis translations and lower back angles for simulations approaching and exceeding $0.5s$. By changing both the forces and accelerations in a controlled fashion, RRA is able to achieve much more stable and longer lasting results than REA [154].

A.4 The Calibration Pipeline

OpenSim models are sensitive to modelling errors, particularly during the scaling step. Incorrect weighting of markers, or marker data which has become unusable during the course of an experiment[28], can significantly alter the resultant joint torques and muscle activations observed in simulation.

In practice, the model calibration process in OpenSim typically involves modifying the weights of the scaling step to optimise for tracking error and RRA residuals, both of which should be minimised. In the OpenSim documentation, the developers provide reasonable cut-offs for these parameters. These cut-offs are summarised for reference in Table A.1.

In Figure A.2, a schematic is provided outlining the model calibration process. Starting from a generic model (e.g. the gait2392 or gait2354 models), a scaled model is generated via the scaling step, and further adjusted via the RRA algorithm to better match the experimental data. Between each model transition, analyses of tracking errors and RRA residuals are undertaken to

[28] For example, due to a marker which significantly shifted in location over time due to loose clothing or other factors.

Quantity	OpenSim Cut-off
RMS Position Error (m)	0.05
Max Position Error (m)	0.04
RMS Rotation Error (deg)	5
Max Rotation Error (deg)	5
RMS Residual force (N)	10
Peak Residual force (N)	25
RMS Residual moment (Nm)	50
Peak Residual moment (Nm)	75

Table A.1: Maximum allowed values for tracking errors and RRA residuals as specified by the OpenSim developers. Results exceeding these values indicate that the scaled model poorly fits the measured experimental data.

ensure that the generated models are sufficiently accurate.

A.5 Inverse Dynamics

OpenSim uses the Simbody dynamics engine [152] to perform inverse dynamics by solving the multibody equation of motion over time, i.e

$$\tau = M(\mathbf{q})\ddot{\mathbf{q}} + \mathbf{C}(\mathbf{q}, \dot{\mathbf{q}}) + \mathbf{g}(\mathbf{q}) + J(\mathbf{q})^T f_{\text{ext}}, \tag{A.2}$$

where τ and $\mathbf{q}$ are the vectors of joint torques and joint angles; M and J are the system mass matrix and Jacobian; $\mathbf{C}$ and $\mathbf{g}$ give the non-linear and gravity terms; and finally f_{ext} is the net external force acting on the system, which typically in this case is due to a combination of ground reaction forces and exoskeleton assistance components.

A.6 Static Optimisation

The 23 degrees of freedom of the human-APO musculoskeletal model are driven by 54 musculo-tendon units (MTUs). Each MTU produces force ϕ_m according to its normalised length λ_m, velocity v_m, and the level of muscle activation α_m, i.e.

$$\phi_m = H(\alpha_m, \lambda_m, v_m, \pi_m). \tag{A.3}$$

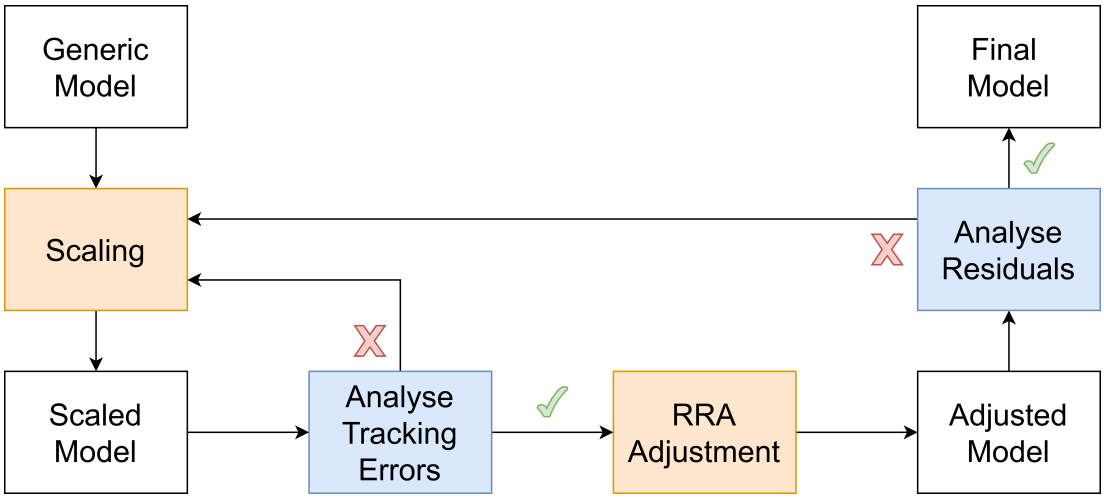

Figure A.2: A diagram outlining the key steps of model calibration. First, a generic model is scaled to match static data. This scaled model is made to track kinematic data, and the scaling process is repeated with modified weights until sufficient tracking accuracy is obtained. Then, the RRA algorithm is used to adjust the scaled model and identify the residual force required to track a specified motion. This entire process repeats until the RRA residuals are within the guidelines specified in Table A.1.

Here, H is a black-box function which encodes the relationship between muscle parameters π_m, such as optimal fibre length and maximum force, and the relationship between muscle force and current state. In practice the behaviour of H depends on the muscle model used. In this thesis the model used is a modified version of a Hill-type muscle model [72], referred to within OpenSim as the Thelen 2003 muscle model.

Consider a time history of torques at each joint of the model, as computed by Equation (A.2). These joint torques are composed of force contributions from the muscles of the model, which are mapped in to joint space by a coupling matrix C_m determined by the placement of the muscle relative to the joint [155]. For a given joint j with c muscles crossing that joint, we have

$$\tau_j = \sum_{m=1}^{c} \phi_m^\top C_m. \tag{A.4}$$

For a known set of joint torques there are infinitely many solutions for the corresponding muscle activations. To identify a unique solution we can optimise

over some objective function; in this work, we choose to minimise the sum of squared muscle activations i.e.

$$\min \sum_{m=1}^{n} (\alpha_m)^2, \tag{A.5}$$

where for our model we have $n = 54$. The process of solving Equations A.3 and A.4 while minimising Equation (A.5) is known as static optimisation. Static optimisation is significantly faster computationally than dynamic tracking algorithms such as CMC, which we discuss next, and previous work has indicated that for relatively low-impact movements (e.g. walking) the differences in the obtained muscle activations are minimal [156, 157].

A.7 Muscle Energetics

Once the muscle activations are determined, either from static optimisation or via a more complex dynamic tracking algorithm known as computed muscle control [153], we can employ a muscle energetics model to compute the energy expenditure for each muscle. The model used in this thesis is based on the well known model by Umberger [145] with modifications to the recruitment of muscle fibres and the treatment of mechanical work [146]. For simplicity we use a black-box function, U, to express this model:

$$\dot{\epsilon}_m = U(\alpha_m, \lambda_m, v_m, \pi_m), \tag{A.6}$$

where $\dot{\epsilon}_m$ is the rate of energy usage of muscle m. Through summation over the full set of muscles we can compute the rate of energy usage of the entire model as

$$\dot{\epsilon} = \sum_{m=1}^{n} \dot{\epsilon}_m, \tag{A.7}$$

where $\dot{\epsilon}$ can be interpreted as the overall energetic cost associated with the movement.

Appendix B

Supplementary Materials

B.1 Gait Metric Invariance Data Table

	Step Width (cm)					Step frequency (steps/min)				
	BW	UW	DW	FW	SW	BW	UW	DW	FW	SW
NE	17.3 ± 4.1	16.8 ± 3.5	18.5 ± 5.1	16.8 ± 4.5	15.9 ± 4.4	103.4 ± 8.7	103.5 ± 9.8	109.4 ± 9.0	108.8 ± 8.5	88.3 ± 6.7
ET	16.2 ± 3.5	15.9 ± 2.2	16.2 ± 3.2	15.9 ± 3.6	15.9 ± 2.5	98.7 ± 14.8	101.3 ± 6.9	105.7 ± 6.5	104.9 ± 12.3	83.9 ± 8.8
EA	15.8 ± 3.1	15.8 ± 3.2	16.3 ± 3.2	15.8 ± 3.8	16.5 ± 3.6	104.3 ± 5.3	105.4 ± 6.7	110.1 ± 6.9	109.2 ± 12.9	93.7 ± 7.5
	$\theta_{\text{hip-RoM}}$(Sagittal hip angles RoM (°))					$\tau_{\text{hip-pp}}$(Sagittal peak to peak hip torques (Nm/kg))				
	BW	UW	DW	FW	SW	BW	UW	DW	FW	SW
NE	36.0 ± 3.0	47.2 ± 3.8	30.4 ± 3.6	40.0 ± 3.2	34.7 ± 3.7	0.98 ± 0.2	1.24 ± 0.2	0.91 ± 0.2	1.23 ± 0.2	0.76 ± 0.2
ET	38.4 ± 2.7	50.3 ± 2.7	33.3 ± 3.8	42.7 ± 2.8	37.6 ± 3.5	1.02 ± 0.2	1.23 ± 0.2	0.97 ± 0.1	1.27 ± 0.1	0.80 ± 0.2
EA	39.6 ± 3.6	49.0 ± 3.0	32.0 ± 3.2	42.2 ± 3.1	36.0 ± 5.2	1.12 ± 0.1	1.33 ± 0.1	1.08 ± 0.2	1.44 ± 0.3	0.91 ± 0.2
	CoP-AP_{disp}(CoP anterior posterior displacement (mm))					CoP-ML_{disp}(CoP medial lateral displacement (mm))				
	BW	UW	DW	FW	SW	BW	UW	DW	FW	SW
NE	419.1 ± 52.2	420.2 ± 56.8	413.4 ± 57.7	484.9 ± 83.7	403.3 ± 50.3	32.2 ± 14.6	31.3 ± 9.6	28.1 ± 13.6	36.8 ± 16.8	37.5 ± 20.3
ET	434.7 ± 45.8	431.3 ± 46.7	439.6 ± 81.8	508.0 ± 51.6	427.5 ± 49.2	37.0 ± 16.5	37.2 ± 13.8	31.5 ± 14.9	41.2 ± 16.9	40.7 ± 28.5
EA	444.9 ± 65.4	419.2 ± 55.1	418.1 ± 79.9	519.9 ± 101.5	390.5 ± 51.4	40.1 ± 18.2	40.2 ± 14.8	42.1 ± 18.2	48.4 ± 24.2	41.5 ± 18.4
	CoM-V_{disp}(CoM vertical displacement (mm))					CoM-ML_{disp}(CoM medial lateral displacement (mm))				
	BW	UW	DW	FW	SW	BW	UW	DW	FW	SW
NE	30.0 ± 4.9	36.0 ± 6.0	35.0 ± 6.0	34.4 ± 4.0	26.6 ± 4.1	58.5 ± 19.7	55.0 ± 13.6	53.2 ± 19.3	49.8 ± 17.6	68.0 ± 23.2
ET	30.7 ± 4.8	37.6 ± 4.7	34.5 ± 5.9	38.4 ± 5.8	28.9 ± 5.1	55.0 ± 18.8	54.0 ± 12.2	51.6 ± 16.7	51.6 ± 16.0	72.1 ± 18.5
EA	31.7 ± 4.1	37.8 ± 5.0	33.4 ± 4.6	38.6 ± 5.7	28.9 ± 4.0	52.0 ± 13.7	51.1 ± 12.2	45.4 ± 14.3	45.4 ± 12.6	64.2 ± 18.7
	MoS-AP (Margins of stability - anterior posterior (mm))					MOS-ML (Margins of stability - medial lateral (mm))				
	BW	UW	DW	FW	SW	BW	UW	DW	FW	SW
NE	104.0 ± 36.1	101.8 ± 46.9	157.8 ± 45.4	120.8 ± 46.1	59.3 ± 36.3	68.8 ± 16.9	70.2 ± 18.6	72.05 ± 17.4	69.5 ± 20.6	63.3 ± 21.7
ET	90.2 ± 34.8	102.3 ± 39.6	135.6 ± 32.6	112.3 ± 25.6	39.8 ± 30.8	71.8 ± 17.3	70.1 ± 17.2	66.16 ± 15.3	71.75 ± 18.6	62.2 ± 18.6
EA	97.5 ± 25.7	112.5 ± 40.8	144.5 ± 41.9	125.5 ± 36.5	64.4 ± 30.1	68.7 ± 18.7	69.4 ± 15.8	70.0 ± 21.4	70.3 ± 18.5	66.8 ± 16.2

Table B.1: Mean ± standard deviation of metrics categorised by walking context and assistance scenario.

B.2 Metabolic Power Consumption Data Table

	Adductor brevis (mW/kg)					Adductor longus (mW/kg)				
	BW	UW	DW	FW	SW	BW	UW	DW	FW	SW
NE	17.2 ± 2.7	16.9 ± 2.1	16.4 ± 2.2	17.3 ± 2.8	16.2 ± 1.9	47.4 ± 13.7	51.8 ± 13.8	40.9 ± 11.7	52.2 ± 13.5	37.1 ± 8.8
ET	16.3 ± 2	16.4 ± 2.3	16.6 ± 2.2	17.4 ± 2.8	15.7 ± 1.8	44 ± 10.5	47.1 ± 12.1	40.8 ± 10.3	53.4 ± 15.6	35.4 ± 7.9
EA	17.3 ± 2.6	17 ± 2.7	17.5 ± 3.1	18 ± 3.1	16.6 ± 2.2	44.8 ± 13.6	48.2 ± 13.4	45.5 ± 13.3	51.1 ± 17.6	37.4 ± 8.3
	Adductor magnus (mW/kg)					Psoas (mW/kg)				
	BW	UW	DW	FW	SW	BW	UW	DW	FW	SW
NE	14.2 ± 6.1	16.1 ± 9.3	13.4 ± 5.3	15.4 ± 7.5	13 ± 4.8	194.4 ± 40.8	228 ± 38.8	178.6 ± 35	218.6 ± 37.5	161.6 ± 27
ET	13.9 ± 6.1	14.7 ± 7.9	14.2 ± 7.3	15 ± 7.6	13 ± 5.3	204.3 ± 32.5	232 ± 30.8	203.1 ± 38.5	233.5 ± 34.9	169.3 ± 27
EA	14 ± 6	14.9 ± 7.9	14.7 ± 8	15.1 ± 7.7	13.3 ± 5.2	198.1 ± 35.2	213.4 ± 32.7	202.2 ± 37	229.9 ± 53.7	166.2 ± 33.8
	Gluteus maximus (mW/kg)					Biceps femoris long head (mW/kg)				
	BW	UW	DW	FW	SW	BW	UW	DW	FW	SW
NE	72.9 ± 45.8	157.8 ± 101.3	41.8 ± 21.9	89 ± 54.3	63.4 ± 38.2	71.5 ± 33	116.1 ± 39.4	51.5 ± 20.6	91.8 ± 39.6	60.3 ± 20.4
ET	68.8 ± 43.7	159.5 ± 101.6	36.7 ± 20.7	82.6 ± 52.7	59.5 ± 36	76 ± 31.4	112 ± 34	61.8 ± 29.6	96.3 ± 38.4	61.3 ± 22
EA	73.7 ± 47.3	162.3 ± 106.2	40.7 ± 23.9	89.9 ± 55.9	62.9 ± 37.5	72 ± 30.8	110.2 ± 35.5	58.7 ± 29	101.2 ± 50.9	66.7 ± 27.3
	Rectus femoris (mW/kg)					Vastus medialis (mW/kg)				
	BW	UW	DW	FW	SW	BW	UW	DW	FW	SW
NE	198 ± 63.3	225.2 ± 69.7	230.1 ± 66.2	233.1 ± 72.1	188 ± 52.2	52.6 ± 21	84 ± 20.2	63.2 ± 27.2	66.6 ± 22.7	41.6 ± 11.2
ET	229.3 ± 70.9	244.7 ± 89.5	235.9 ± 78.9	238.9 ± 64.1	211.9 ± 75.1	60.8 ± 20.3	114.1 ± 22.1	72.1 ± 23	75.3 ± 28.8	49 ± 13.5
EA	205.5 ± 69.3	233.3 ± 91.5	236.5 ± 84.2	234.2 ± 87.1	207.3 ± 72.2	59 ± 13.7	108.7 ± 21.9	75.8 ± 22.9	78.7 ± 28.6	53.6 ± 22.1
	Medial gastrocnemius (mW/kg)					Soleus (mW/kg)				
	BW	UW	DW	FW	SW	BW	UW	DW	FW	SW
NE	197.1 ± 34.2	205.5 ± 36.1	155.3 ± 26.8	204.4 ± 39.9	160.9 ± 26.9	290.8 ± 67.4	355.4 ± 100.9	238.1 ± 63	334.8 ± 85.6	219.5 ± 73.8
ET	201.1 ± 44.9	198.2 ± 25	175.6 ± 37.3	221.2 ± 47.6	172 ± 30.3	318.3 ± 90	368.4 ± 108.9	250.5 ± 56.7	369 ± 89	243.3 ± 55.5
EA	198.2 ± 36.5	208.3 ± 32.2	163.4 ± 33	221.2 ± 69.2	176 ± 31.6	291.8 ± 83.8	385.1 ± 101.4	240.9 ± 88.3	354.3 ± 143.9	246.7 ± 65.2

Table B.2: Mean ± standard deviation of power consumption categorised by walking context and assistance scenario.

B.3 Participant Questionnaire Sheet

Subject ID:

You have just experienced Assistance Mode A followed by Assistance Mode B.

Which of the two modes, if either, did you find most comfortable?

1. Mode A
2. Mode B
3. Both the same
4. Not sure

Which of the two modes, if either, do you think best assisted your walking?

1. Mode A
2. Mode B
3. Both the same
4. Not sure

You have just experienced Assistance Mode C followed by Assistance Mode D.

Which of the two modes, if either, did you find most comfortable?

1. Mode C
2. Mode D
3. Both the same
4. Not sure

Which of the two modes, if either, do you think best assisted your walking?

1. Mode C
2. Mode D
3. Both the same
4. Not sure

You have now finished the verification phase of the experiment. You experienced four assistance modes in the order A, B, C, D.

Which of the four assistance modes, if any, did you find most comfortable?

1. Mode .....
2. No one mode was best
3. Not sure

Which of the four assistance modes, if any, do you think best assisted your walking?

1. Mode .....
2. No one mode was best
3. Not sure